Doctoral School of Geosciences

MICROSTRUCTURE, GEOMETRY AND HYDROGEOLOGY OF THE FRACTURE NETWORK OF THE BODA CLAYSTONE FORMATION

A BODAI AGYAGKŐ FORMÁCIÓ TÖRÉSHÁLÓZATÁNAK MIKROSZERKEZETE, GEOMETRIÁJA ÉS HIDROGEOLÓGIÁJA

PhD Dissertation

Author

Emese Tóth

Supervisors

Tivadar M. Tóth, DSc

Professor, Head of the department, University of Szeged, Department of Mineralogy, Geochemistry and Petrology

Félix Schubert, PhD

Assistant professor, University of Szeged, Department of Mineralogy, Geochemistry and Petrology

University of Szeged

Faculty of Science and Informatics

Department of Mineralogy, Petrology and Geochemistry

Szeged

2023

TABLE OF CONTENTS

LIST OF FIGURES

LIST OF TABLES

CHAPTER I.

Introduction

I.1. The actuality of this research

The ever-growing population of the Earth is putting increasing pressure on the planet's resources and having a negative impact on the environment. Today, the concentration of CO_2 in the atmosphere is reaching critical levels (Lee and Ojovan, 2013; Guimarães and Bobos, 2021). With the growth and development of humanity, the electricity demand is rapidly increasing, while the energy sector is responsible for 40% of global CO_2 emissions (Guimarães and Bobos, 2021). Nuclear energy production has good efficiency and produces almost no CO_2 emissions, at least at the point of energy generation (IAE, 2012; Sonnberger et al., 2021). In this regard, nuclear energy has attracted particular interest because it is the only energy source that can simultaneously curb the world's growing energy demand and carbon emissions (Guimarães and Bobos, 2021). Nuclear fission has been providing humanity with a significant portion of our energy for more than 50 years, in a far more harmless, lower-carbon, and environmentally friendly manner, and with significantly less loss of life in its production than other energy sources such as coal, oil, and gas (Lee and Ojovan, 2013). Despite its many positive features, there are significant problems associated with nuclear energy in society: the safety of nuclear plants and the generation of radioactive waste, which must be disposed of in special landfill sites and requires special management. (Christoforidis et al., 2021; Guimarães and Bobos, 2021).

Radioactive waste is material that contains or is contaminated with radionuclides in concentrations or activities greater than clearance levels established by regulatory authorities and for which no use is intended. The hazard associated with radioactive wastes depends on the concentration and type of radionuclides, with those that emit high-energy radiation or are more toxic to life being the most dangerous (Lee and Ojovan, 2013).

In all countries operating nuclear power plants, the management of spent nuclear fuel and long-lived radioactive waste is a major environmental issue. The directive of the European Union is that every country should be able to dispose of its radioactive waste in its territory (Ádám et al., 2016). Since Hungary derives 50% of its energy needs from nuclear energy and the Hungarian Government is basing its long-term energy supply on nuclear energy, solving the problem of the safe storage of radioactive waste is of paramount importance (Christoforidis et al., 2021). Deep geological disposal has been the recommended approach for the permanent disposal of radioactive wastes. Certain geological formations can be called high-isolation sites because either no water is present as a medium for radionuclide transport (e.g. bedded salt, salt

domes) or the permeability of the rock matrix is extremely low, and no fractures are present (e.g. bedded clay, mudstone). These properties assure slow, diffusive transport over relatively large distances (> 50 metres; Apted and Ahn, 2010).

After a preliminary screening in the 90s, the Boda Claystone Formation in the Mecsek Mountains could be a potential medium for the deep geological disposal of high-level radioactive wastes in Hungary. Therefore, the formation has been an important research target of Hungarian geological research in the last 30 years (Lázár and Máthé, 2012). Despite the low porosity and permeability of the formation, which provides the retentive properties, evaluating the tectonic setting of the rock is essential to understand the sequence of occurrence of faults or folds and their amplitude. This analysis leads to an assessment of the tectonic evolution of the host rock, the hydrogeological role of the tectonic structures, and the consequences for the future release of radionuclides into the geosphere (Delay, 2010).

I.2. Outlook

I.2.1. Argillaceous host rocks

Until the late 1990s, there were no direct industrial applications for deep geologic clay formations and little research was done to analyse clay rocks. The advent of the final disposal of radioactive waste in argillaceous formations led to a boom in research in this area (Tournassat et al., 2015). The terminology of the fine-grained sediments is very complex; a brief description of the argillaceous rock types is as follows. The argillaceous rocks (lutites) include shales, claystones, siltstones, and mudstones. Claystone is a clastic rock consisting of more than 50 % of grains finer than 1/256 mm. Siltstone consists of more than 50 % material between 1/256 mm and 1/16 mm. Mudstone is composed of a mixture of clay, silt, and sand-sized particles, none of which make up 50 % of the rock. Laminated lutites that are fissile are called shale (Picard, 1971).

Clays and clay-rock formations are chosen as waste repository host rocks worldwide because of their excellent retentive properties due to their low permeability, but the argillaceous sedimentary formation must meet certain other requirements to host a repository (Norris, 2017).

The formation must protect the waste packages from surface phenomena, mainly climatic effects such as erosion, glaciation, and human activities. This is possible if the deep geological repositories are constructed at an appropriate depth of between 500 and 1500 metres. The formation must have vertical and lateral continuity to ensure radionuclide confinement and intrinsic properties that limit water migration and promote radionuclide retardation. These properties must be provided over long periods, from thousands to several hundred thousand

years. These favourable properties must be maintained despite the disturbance of the rock caused by the construction of the facility. Excavation will create a damaged zone (EDZ), where fractures could form due to the redistribution of stresses around the underground structures after excavation. The favourable properties of argillaceous rocks, creep and swelling, could result in the self-sealing of fissures or fractures; this directly affects the long-term functionality of the host rock as a migration barrier (NEA, 2010; Zhang, 2013; Wang et al., 2015). Self-sealing may result in near complete sealing of the EDZ of the subsurface structures after the closure of the repository (Delay, 2010). If self-sealing occurs within a reasonable time, fractures will not persist as preferential pathways for radionuclide migration, leaving the system dominated by diffusion (NEA, 2010).

The barrier properties of the rock must remain intact despite the effects of the heat-generating waste packages and the degradation of the packages and engineered barriers. Fortunately, these rocks generally have low mechanical resistance and thermal conduction capability (Delay, 2010). The mechanical behaviour of argillaceous rocks is determined not only by void ratio and stress path history but also by the complicated processes of lithification, weathering, and the associated physical and chemical processes (Heitz and Hicher, 2002).

In Europe, in addition to the Boda Claystone in Hungary, three argillaceous sedimentary formations are the subject of intensive research for radioactive waste storage. The Boom Clay near Mol in Belgium, the Callovo-Oxfordian near Bure in France and the Opalinus Clay at Benken and Mont Terri in Switzerland. Siliceous shale and diatomaceous shale are studied for nuclear waste disposal in Japan at the Horonobe site (Delay, 2010). Some basic properties and characteristic minerals of these potential clay host rocks in Europe are summarised and compared in Table I.1.

Table I.1. Specific characteristic data of clay and claystone types considered as perspective hosts in Europe (modified after Lázár and Máthé, 2012)

Formation	Age [Ma]	Depth [m]	Max. temp. [°C]	Pore water [%]	Organic matter [%]	Clay fraction [%]	Albite [%]	Calcite [%]
Boom Clay	30–36	200	16	~25	2–3	35–65	1-2	~1
Callovo-Oxfordian Claystone	155	500	40	~7	~1	~40	~1	~35
Opalinus Clay	180	500	85	~7	~1.5	45–60	~1	4–8
Boda Claystone	250	1000	220	~2	-	35–50	4–8	3–5

In principle, all rock types contain clay minerals in large proportions. Concerning other properties, however, the clayey rocks show considerable differences. Their ages, maximum temperatures during formation, water content, and characteristic minerals differ significantly, demonstrating the unique formation history of each clay rock. Therefore, each of them should be specifically characterised (Lázár and Máthé, 2012).

Deep drillings over the last ten years (BAF–1, BAF–1A, BAF–2, BAF–3, BAF–3A, BAF–4) in the Boda Claystone Formation revealed a more fractured and tectonised rock body than expected. These wells intersected the formation for thousands of metres with nearly 100% core recovery, providing a unique opportunity to study the formation in detail. In addition to studying the sorption, diffusion and mechanical properties of the host rock, analysis of the fracture network is essential. Since fracture networks are usually the main pathways for fluid transport in subsurface rocks, especially when the matrix is nearly impermeable compared to the fractures, as in the case of the Boda Claystone (Berkowitz, 2002).

I.2.2. Fractured rock bodies

Fractures are the most common visible structural features in the Earth's upper crust. They are found in most rock bodies, and most reservoirs likely contain some natural fractures. Naturally fractured reservoirs are complex systems that are difficult to characterise, engineer and predict (National Research Council, 1996). The study of fractured reservoirs and the modelling of their fracture network is usually associated with the petroleum industry or water supply, where they want to extract fluids from the rock body. Conversely, by modelling fracture networks in the case of waste repository rocks, we can answer the question of whether the fluid will remain in the rock or not. In the case of a waste repository, the favourable hydrodynamic conditions have the opposite meaning as in the case of a potential oil, gas or water reservoir.

Fractures are naturally occurring discontinuities that often form complex networks and dominate the geomechanical and hydrological behaviour of subsurface rocks (Zimmermann and Main, 2004). In the fracture networks, individual fractures may occur over a wide range of sizes, from submicroscopic to hundreds of meters, but some of their features are comparable across different size ranges (Turcotte, 1992; Long, 1996). Thus, the structural geological data of fractures and microfractures that can be documented in excavations and boreholes can provide important information about large-scale structures, faults and fault zones.

Estimating in situ fracture properties is a challenge in characterising fractured reservoirs. This is because fracture properties, such as aperture, porosity, or permeability, cannot be measured directly in the case of subsurface rock. We must rely on observation from outcrops and underground tunnels (two-dimensional, 2D) and use one-dimensional (1D)

geological and geophysical tools in boreholes (Einstein and Baecher, 1983). Seismological surveys can locate large-scale 3D structures, but current technology can hardly detect widespread medium and small fractures due to the resolution limit of the method. The description of natural fracture geometries must rely mainly on extrapolations, from 1D-2D to 3D and from small samples to the entire study area (Lei et al., 2017). Recently, borehole video logging technology (borehole camera, optical and acoustic televiewer-BHTV) has been widely used in geological and hydrogeological research and nuclear waste research to measure fracture characteristics in boreholes. The fracture orientation (dip direction and dip), spatial parameters, and *P10* linear fracture intensity could be easily determined using these methods (Pavičić et al., 2021). Acoustic borehole televiewers give a picture of the interior of a borehole by measuring the acoustic amplitude and return time of an ultrasonic signal emitted by a borehole logging tool. Analysis of these logs provides a continuous picture of where fractures intersect the borehole, which is particularly useful in boreholes without oriented drill cores (Zamenak, 1970; Massiot et al., 2017).

Due to the unknown nature of in situ fractures outside of boreholes, from geometric properties to spatial distributions, simplifications often must be made by omitting details that are less important to the question at hand (Lei et al., 2017). Several simple or simplified conceptual models and scenarios have been proposed, developed, and used to approximate or characterise the complicated flow behaviour in fractured porous media systems. Such modelling approaches include discrete fracture, double porosity, double permeability, multicontinuum, etc. (Wu, 2016). Herein only the discrete fracture network approach is discussed.

A "discrete fracture network" (DFN) refers to a computational model that explicitly represents the geometric properties of each fracture (e.g., orientation, size, position, shape, and aperture) as well as the topological relationships between individual fractures and fracture sets (Long et al., 1982; Lei et al., 2017). The discrete fracture modelling approach requires detailed knowledge of the fracture and matrix geometric properties and their spatial distributions (Wu, 2016). The qualitative characteristics of fractures and the values of their measurable, geometrical parameters depend essentially on the petrographic properties of the deformed rock type, mineral composition, grain size distribution and structure. In addition, the physical conditions under which the deformation takes place are crucial. The primary importance of the stress field is also significantly modified by the confining stress, temperature and fluid content of the rock. The resulting fracture system as a geometric object consisting of individual fractures is created as a result of all these effects (M. Tóth, 2008).

Modelling the geometry of fracture networks defines the geometrically connected fracture groups, which is a fundamental step in understanding and predicting the hydromechanical behaviour of the fracture system (National Research Council, 1996).

Flow and transport behaviour of the fracture systems are obtained with numerical models. The first step in developing a numerical model is to create an appropriate conceptual model of the fracture system. The conceptual model is a physical model of the system that describes the key features of the geology and hydrology that control the flow and transport behaviour of the studied rock body. A conceptual model includes an interpretation or schematisation of reality that forms the basis for mathematical calculations of behaviour (National Research Council, 1996). Building the numerical models for flow and transport is beyond the main topic of this thesis, but the determination of the critical features that formed the fracture system in the investigated boreholes could serve as a future basis for flow and transport modelling of the Boda Claystone Formation.

I.3. The aims and structure of the dissertation

This dissertation investigates the brittle structural elements of a potential repository rock for high-level radioactive waste on a wide scale. The study was carried out using core samples and borehole data, therefore all depth values is in total measured depth through the entire work. The principle of the research is that each successive phase of research examines the problem at an increasing scale, from microstructural measurements to the investigation of the fracture network based on multiple boreholes. Microscale studies of small segments of the fracture network contribute to the understanding of the behaviour of the entire fracture network. The main objective of this study was to reveal the geometry and hydrodynamic character of the fracture network of the Boda Claystone Formation as well as the investigation of the spatial extensibility of the properties of the fracture network.

The following sections represent a selection of published and accepted papers about the research of the structural interpretation of the Boda Claystone Formation. After this brief introduction (Chapter I.), each chapter represents a different stage of the research.

Chapter II. presents a microstructural analysis of the sigmoidal-shaped veins that are characteristic structures of the Boda Claystone Formation. In this study, sigmoidal veins were investigated in an uncommon host rock. These structures typically occur in sandstones and carbonate rocks where pressure solution and stylolites are common accompanying processes. These processes are confined within a claystone body, suggesting a unique formation for the sigmoidal veins. Furthermore, we have used geometric and chemical analysis of the sigmoidal

veins to investigate the shear strain and volume changes occurring in the accompanying shear zones in the BAF−2 well.

In Chapter III. The potential waste reservoir was studied on a larger scale to understand the geometry of the fracture network and the processes that controlled the formation of the connected fracture clusters in the BAF−2 well. By modelling the fracture network using the DFN modelling approach and evaluating the hydrodynamic behaviour of the rock body, different flow units were determined along the well, and their formation processes were discussed.

Chapter IV. represents an attempt to establish the relationship between the fracture density and the conventional geophysical logs of the BCF in the BAF−4 and BAF−2 wells with multiple regression analysis. With this method, the fracture density of the well could be predicted in older wells where BHTV data is unavailable. In this way, we could involve more wells in the fracture network modelling in the future, which could provide more information about the extensibility of communicating fracture clusters and large-scale structures, such as faults.

Finally, Chapter V. presents the summary of the main findings of the work and a conclusion of the entire thesis. A summarised reference list is provided at the end of the thesis.

CHAPTER II.

ESTIMATING SHEAR STRAIN AND VOLUME CHANGE USING SIGMOIDAL VEINS: CASE STUDY OF THE BODA CLAYSTONE

Emese Tóth

Department of Mineralogy, Geochemistry and Petrology, University of Szeged, Hungary

tothemese@geo.u-szeged.hu

Ervin Hrabovszki

Department of Mineralogy, Geochemistry and Petrology, University of Szeged, Hungary

hrabovszkiervin@geo.u-szeged.hu

Tivadar M. Tóth

Department of Mineralogy, Geochemistry and Petrology, University of Szeged, Hungary

mtoth@geo.u-szeged.hu

Félix Schubert

Department of Mineralogy, Geochemistry and Petrology, University of Szeged, Hungary

schubert@geo.u-szeged.hu

Journal of Structural Geology

Volume 138, 2020, 104105

DOI 10.1016/j.jsg.2020.104105

Estimating shear strain and volume change using sigmoidal veins: Case study of the Boda Claystone

Emese Tóth, Ervin Hrabovszki, Tivadar M. Tóth, Félix Schubert

Abstract

The Boda Claystone Formation, a potential host rock for high-level nuclear waste in Hungary, contains numerous sigmoidal vein arrays with angular vein terminations. These veins are excellent strain markers and can be used in the interpretation of palaeo-environments. Sigmoidal vein arrays were investigated in the BAF–2 well, which penetrates the formation to depths above 900 m with nearly 100% core recovery. The veins have antitaxial growth morphologies and are filled by calcite, anhydrite and barite–celestine phases. To estimate the volume change in shear zones, we used geometric, mass-balance and density-change calculations. These methods exhibit different volume loss rates. The geometric approach indicates a large amount of volume loss, whereas the isocon method and density-change approach suggest that volume loss in the shear zones was less than 10%. We propose that the volume loss in the shear zone occurred because of tectonic compaction. Vein shapes indicate formation under compressional stress fields. Based on their intersections with other vein generations, the sigmoidal *en échelon* vein generation is determined to be one of the youngest structures in the well.

II.1. Introduction

Fracturing and vein formation in rock bodies provides essential information for interpreting their paleo-environments and conditions of formation. Among others, sigmoidal veins are excellent strain markers with a characteristic geometry that can be used for understanding stress field and vein cementation processes (Ramsay, 1980; Ramsay and Huber, 1987; Olson and Pollard, 1991; Lisle, 2013). Sigmoidal tension gashes are S- or Z-shaped veins, occurring as arrays in which they usually exhibit an *en échelon* (step-like) arrangement (Fig. II.1).

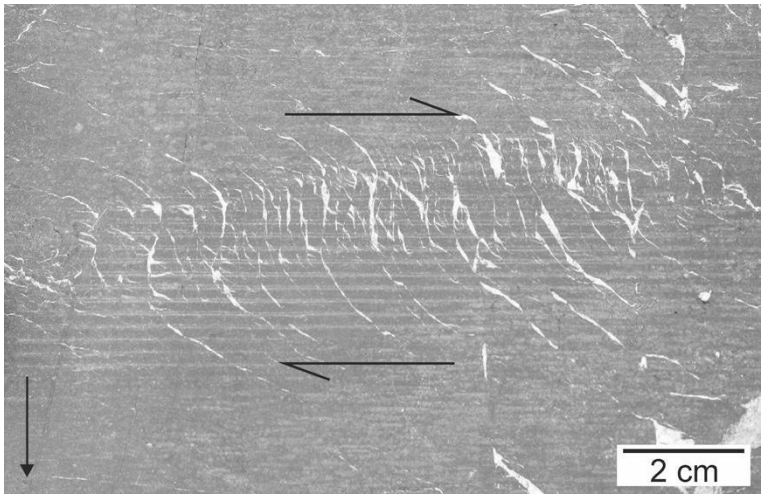

Fig. II.1 Sigmoidal en échelon vein array in the studied claystone; sample BAF–2_657. The horizontal arrows indicate the shear sense of the shear zone. The arrow in the lower left corner indicates the core axis and downward direction of the specimen.

The longitudinal axis of the veins is parallel to the largest principal stress (σ_1), and veins are the thickest perpendicular to σ_1 in the central parts before tapering towards their ends (Ramsay and Huber, 1987; Lisle, 2013). Sigmoidal *en échelon* veins are common in deformed sedimentary rocks, especially carbonates and sandstones. Their development is usually accompanied by pressure solution (Beach, 1975; Seyum and Pollard, 2016), such that pressure solution seams accumulate the relatively insoluble phases of rock material, e.g. clay minerals, graphite, iron oxides and hydroxides. Tectonic stylolites form almost synchronously with vein propagation in calcareous rocks, where precipitating vein-filling minerals are derived directly from the stylolite (Ramsay and Huber, 1983). Sigmoidal vein arrays frequently occur in conjugate pairs in outcrops, where the strain rate of the two shear zones is approximately equal intensity, and the orientation of the principal axes of the stress field can be determined using these conjugate pairs. The bisector angles between conjugate pairs indicate the directions of the maximum and minimum principal stresses (Ramsay and Huber, 1987).

Several authors (Ramsay and Graham, 1970; Beach, 1975; Nicholson and Pollard, 1985; Nicholson and Ejiofor, 1987; Olson and Pollard, 1991; Nicholson, 2000; Lisle, 2013; Thiele et al., 2015) have discussed the formation mechanism of sigmoidal veins. Although many specific details remain subject to discussion, it is widely accepted that their formation is related to shear zones. According to Ramsay and Huber (1987), such veins usually occur in brittle-ductile shear zones, where continuous and discontinuous deformational features are combined.

The studied sigmoidal vein arrays are from the Late Permian Boda Claystone Formation, which is a potential host rock for high-level radioactive waste in Hungary (Konrád and Hámos, 2006). Samples were obtained from the BAF–2 well, which penetrated the formation to depths

of more than 900 m with close to 100% core recovery; more than 200 sigmoidal vein arrays can be identified along the well.

This study aimed to present a detailed description of sigmoidal vein arrays in an uncommon host rock and estimate the amount of shear strain and volume change in shear zones along the BAF–2 well through the application of three approaches: geometric, mass-balance and density-change calculations.

II.2. Geological setting

The Late Permian Boda Claystone Formation (BCF) is located in SW Hungary in the Mecsek Mountains. Its distribution covers approximately 150–200 km^2, and its average thickness is 1000 m (Fig. II.2; Konrád and Hámos, 2006).

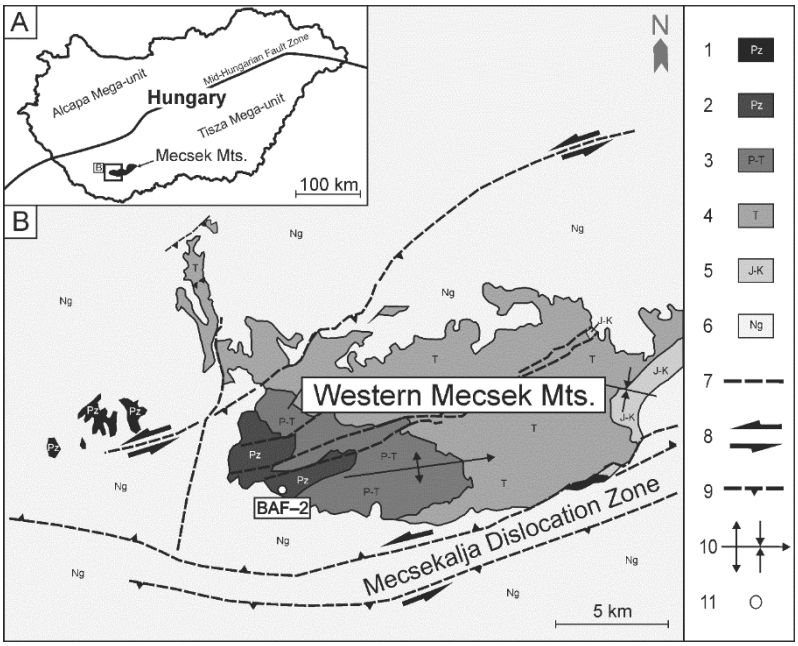

Fig. II.2 (A) Map showing the location of the Mecsek Mountains in Hungary. (B) Distribution of the Boda Claystone Formation (modified after Konrád and Sebe, 2010). Legend: 1 Palaeozoic; 2 Upper Permian Boda Claystone Fm; 3 Upper Permian–Triassic Kővágószőlős Sandstone Fm; 4 Triassic sediments (sandstones, carbonates and evaporites); 5 Jurassic and Cretaceous sediments and Cretaceous volcanite; 6 Neogene sediments; 7 fault; 8 strike-slip fault; 9 thrust fault; 10 syncline and anticline; 11 well site.

The BCF consists mainly of well-compacted homogeneous reddish-brown claystones and siltstones with sandstone and dolomite interbeds. It contains predominantly albite, illite–muscovite, quartz, hematite, calcite, dolomite and chlorite mineral phases (Árkai et al., 2000; Máthé, 2015). Based on its mineralogical, petrographical, geochemical and sedimentological characteristics, the depositional environment of the formation was a shallow alkaline lake and

playa mudflat that formed under arid–semiarid climate (Árkai et al., 2000; Varga et al., 2005; Konrád et al., 2010; Máthé, 2015). Derived from illite and chlorite crystallinity, deep diagenetic to lower anchizone conditions (200 °C–250 °C) prevailed in the BCF (Árkai et al., 2000).

Various brittle structures can be identified along the well, indicating multiple tectonic deformations. Árkai et al. (2000) conducted detailed investigations of veins in the formation and defined examples dominated by calcite, barite–quartz–calcite, anhydrite, calcite–barite and calcite–anhydrite precipitated from meteoric (~70 °C) and/or hydrothermal (~150 °C) parent fluids. Based on the mineralogy and microstructure of veins in the BAF–2 well, four groups of veins (branched veins, straight veins, breccia-like veins and sigmoidal veins) were defined by Hrabovszki et al. (2017). The most characteristic feature of branched veins is the presence of wall-rock inclusions within the veins with a typical cone-in-cone geometry ($Vein_{CIC}$; e.g. Cobbold and Rodrigues, 2007). The average width of the veins varies between 2–15 mm; they mainly consist of calcite with a significant amount of albite around the solid inclusions. Straight veins ($Vein_{STR}$) are 1–5-mm wide; the vein-filling minerals are dominantly calcite and anhydrite with elongate blocky morphology, although a small amount of barite–celestine and quartz is also present. Straight veins have syntaxial vein morphologies with several inclusion bands, indicating multiple subsequent opening events. The average width of breccia-like veins is 5–12 mm ($Vein_{BR}$), and these morphologies are filled with blocky calcite, fibrous quartz and minor amounts of pyrite. Calcite crystals grow on the walls, leaving open pores inside the vein. The last vein type described in the studied core material is the sigmoidal *en échelon* vein ($Vein_{ECH}$; Hrabovszki et al., 2017). Based on the intersection of veins, a relative age relationship of each vein generation can be determined (Fig. II.3).

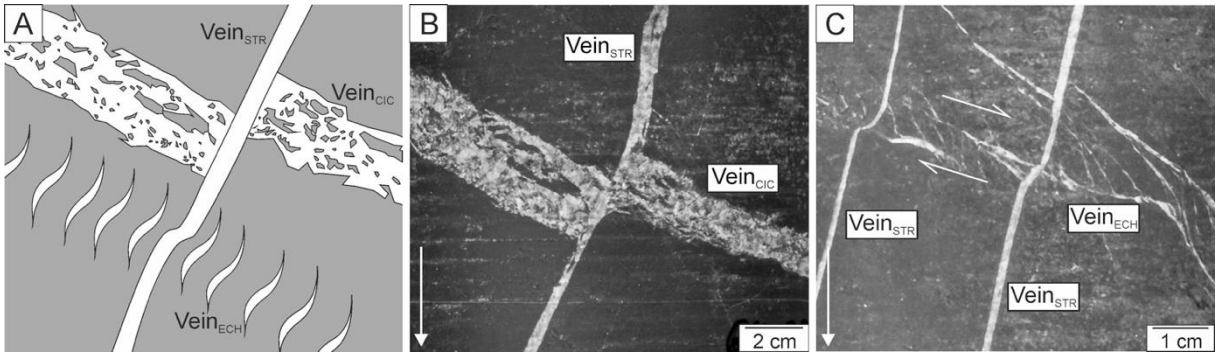

Fig. II.3 (A) Intersection geometry of the VeinCIC, VeinSTR and VeinECH generations. (B) The oldest vein generation is VeinCIC, which is penetrated by the VeinSTR generation in sample BAF–2_662. (C) VeinSTR is sheared by VeinECH in sample BAF–2_667. There is no evidence for the intersection between the Vein$_{CIC}$ and Vein$_{ECH}$ generations in the studied core samples. The arrow in the lower left corner indicates the core axis and the downward direction.

It is well documented in numerous cases that branched veins are cross-cut by straight veins and are thus older. According to Hrabovszki et al. (2017), sigmoidal veins are younger than the straight vein generation because the sigmoidal arrays offset the straight vein generation. Nevertheless, they did not observe intersections among the branched, breccia-like and sigmoidal veins.

II.3. Samples and methods

Measurements were performed on core samples from the BAF–2 well between 500 and 667 m. The studied samples represent a ~200-m-long section within the 900-m-deep well. The numbers in the sample names denote the specimen depth. Based on macroscopic and microscopic features in the studied samples, the conditions of the vein formation in this portion of the well were similar. Consequently, each sigmoidal vein is considered to have the same formation history. For petrographic analysis of the veins, a standard polarising Olympus BX41 microscope with Olympus DP73 digital microscope camera was used. Cathodoluminescence (CL) images were obtained using a Reliotron VII CL instrument operated at 7 kV and 0.7 mA, mounted on an Olympus BX43 microscope. Raman spectroscopy was conducted using a Thermo Scientific DXR Raman microscope equipped with a 532-nm wavelength Nd:YAG laser. A laser power of 10 mW and a pinhole confocal aperture of 25 □m were used for these measurements.

To estimate the volume change effect of a geological process, the representative elementary area (REA) of the analysed system should first be identified. By definition, the REA

is the smallest area above which the given petrographic parameter can be considered representative of the whole (Bear, 1972; Kanit et al., 2003).

Based on its microstructure, the studied system can be subdivided into two major domains, the wall rock and shear zone. The wall rock is undeformed, whereas the shear zone contains two further subdomains, sigmoidal veins and the rock bridges between them (Fig. II.4).

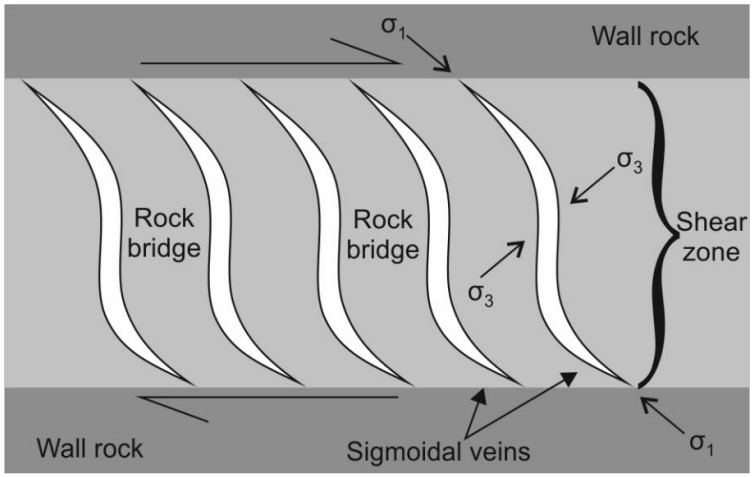

Fig. II.4 Domains of the studied system; the two major domains are the wall rock and the shear zone. The shear zone contains two subdomains, the veins and their intervening rock bridges.

The veins and rock bridges were treated independently, such that REA was estimated for each of the three microdomains using density and volume change calculations.

The REA of the two major domains was determined using image analysis of micro-CT data. Micro-CT analysis was conducted on a single core sample of the BAF–2 well at 657-m depth, containing a 2-cm-wide shear zone with sigmoidal veins. Two micro-CT measurements were performed: one on a sample from the wall rock lacking veins or macroscopic inhomogeneity (BAF–2_657$_{WR}$) and another on a sample from the shear zone (BAF–2_657$_{SZ}$), containing both sigmoidal veins and rock bridges. The CT slices were perpendicular to the vein orientation, facilitating the simultaneous visualisation of both bridges and veins in one slice. Micro-CT scans used a Bruker Skyscan 2211 cone-beam scanner with X-ray source settings as follows: 168-kV source voltage, 50-µA source current and 50-ms exposure time for each measurement. The voxel size of the dataset was 11 × 11 × 11 µm^3. CT was used to determine Hounsfield Units (HU), numerical data presenting a linear correlation with material density over limited density intervals (Kawamura, 1990; Guntoro et al., 2019).

The REA was determined *via* image analysis using the ImageJ software on 16-bit greyscale CT images. To achieve this, squares of gradually increasing size were chosen by a random sampler macro (Appendix A), and the average colour value of each square was computed. The sizes of the squares were between 2 and 250 pixels, and the pixel size was 11

μm. Variation coefficients (the ratio of mean and standard deviation) of the colour values of the squares were determined, and the REA was defined as the pixel size where this value reaches a threshold (in the present case, 0.05). All further investigations were conducted on REA-sized portions of the samples.

The strain analysis of the shear zone was conducted using three different methods. Based on Lisle (2013), both the shear strain and volume change of a shear zone can be determined by the geometry of sigmoidal veins. The sigmoidal shape of veins can develop in two ways according to the passive rotation and folded bridge models (Lisle, 2013). These models provide different approaches to calculating shear strain and volume change.

According to the passive rotation model, the curvature of the vein is produced by heterogeneous strain within the shear zone; therefore, different segments of the tension gash rotate differently. The final orientation of the tension gash depends on both the initial orientation of the vein and the strain accumulated since the propagation of the tension gash (Beach, 1975; Lisle, 2013). In the case of isochoric (constant volume) simple shear, the expected initial orientation of the veins is 45° with respect to the shear zone boundary (Ramsay and Huber, 1987). If volume change accompanies shear strain, this angle could be lower or higher, resulting in a positive or a negative volume change (Ramsay and Graham, 1970; Lisle, 2013).

The application of this model requires the use of two differently oriented passive line markers deformed by the shear zone (Fig. II.5) to calculate shear strain and volume change following the method described by Ramsay (1980). Shear strain (Eq. II.1) and the volume change (Eq. II.2) can be estimated as follows (Ramsay, 1980):

$$\gamma = \frac{cot\alpha' cot\beta - cot\beta' cot\alpha}{cot\alpha' - cot\beta'} \quad \text{(II.1)}$$

$$1 + \Delta = \frac{cot\alpha - cot\beta}{cot\alpha' - cot\beta'} \quad \text{(II.2)}$$

where α is the original orientation of the tension gash, and α' is the deformed orientation (Fig. II.5). The original fracture orientation, α, can be estimated from the orientation of the gash tip at the edge of the shear zone. β and β' are the initial and the deformed orientations of the passive line marker, respectively (Fig. II.5; Ramsay, 1980; Lisle, 2013).

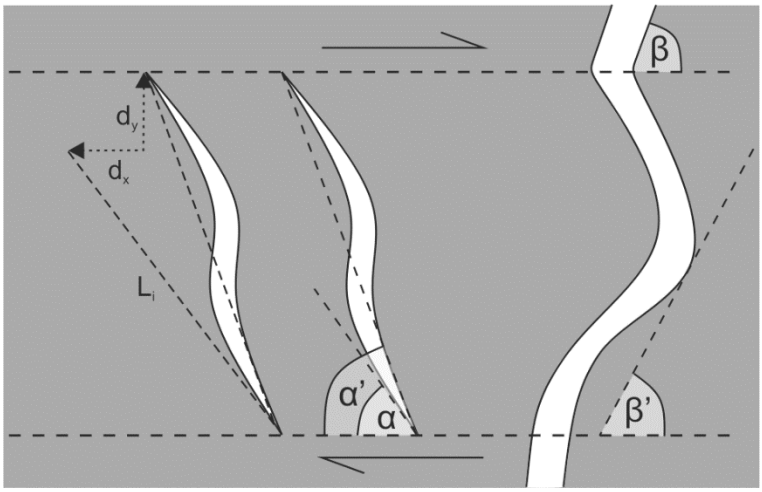

Fig. II.5 Position of α, α' and β, β' in the shear zone. α and α'are the initial and deformed tension gash orientations, β and β' are the initial and deformed vein orientations (ß' is the acute angle between the tangent of the inflexion point of the sheared vein and shear zone boundary), and d_y and d_x are the dilatational and lateral components of shear zone displacement. L_i indicates the initial length of the vein. Modified from Lisle (2013).

The folded bridge model considers the mechanical strength of the rock bridges between veins. The curved shape of the vein forms during dilatation of the gash and is influenced by the mechanical competence of the rock bridges. The strain rate of the shear zone can be determined by measuring the displacement of points along the shear zone boundary. In this approximation, d_x is the component parallel to the shear zone boundary, giving simple shear, whereas d_y is the boundary-normal component, indicating the volume change of the shear zone (Fig. II.5). Dividing d_x and d_y by the original width of the zone gives D_x and D_y, respectively (Lisle, 2013). Finally, according to the folded bridge model, shear zone displacement can be obtained using an eight-step algorithm (for details, see Lisle, 2013). This method requires the orientation data α and α' for sigmoidal veins (denoted as above).

The geometric analysis of the shear zones was conducted on core scanner images of samples BAF–2_662 and BAF–2_667, and the width of the investigated shear zones was approximately 5 mm in both cases.

Mass-balance calculations were applied using the bulk rock chemical composition of two portions of a single sample (BAF–2_500). One part represents the wall rock without any visible inhomogeneity, and another represents the shear zone, which contains sigmoidal veins and intervening rock bridges. Each sample has a weight of 60 g. The bulk rock chemical analysis was conducted by the Bureau Veritas Mineral Laboratories, Canada, using the LF100 and XF702 analysis packages, and the whole-rock chemical data are presented in Table II.1.

Table II.1. Bulk chemical composition of the wall rock (WR180205) and the shear zone (HH180205)

	WR180205	**HH180205**
	wt%	
SiO_2	51.10	49.20
TiO_2	0.74	0.68
Al_2O_3	17.60	16.90
Fe_2O_3	7.68	7.47
MnO	0.08	0.10
MgO	4.00	3.78
CaO	3.98	5.80
Na_2O	3.14	3.08
K_2O	4.76	4.48
P_2O	0.35	0.33
SO_3	0.032	0.055
Cr_2O_3	0.02	0.01
	ppm	
Ba	345.00	611.00
Be	8.00	4.00
Co	21.30	20.60
Cs	18.80	17.80
Ga	25.50	25.10
Hf	3.90	3.70
Nb	15.60	15.60
Rb	235.20	227.90
Sn	5.00	5.00
Sr	252.40	267.60
Ta	1.30	1.10
Th	17.30	16.10
U	3.80	3.60
V	105.00	101.00
W	105.30	3.00
Zr	143.50	134.10
Y	32.60	33.70
La	45.30	44.10
Ce	89.40	84.30
Pr	10.33	10.09
Nd	39.90	37.90
Sm	7.99	7.68
Eu	1.29	1.39
Gd	6.81	6.69
Tb	1.03	1.06
Dy	6.01	5.86
Ho	1.17	1.22
Er	3.68	3.39
Tm	0.49	0.48
Yb	3.22	3.32
Lu	0.51	0.49

The density of the investigated sample (BAF–2_500) was determined to be the average of two independent measurements using the water displacement method. Prior to measuring their weight and volume, samples were coated with impermeable masking fluid to prevent water infiltration during measurement.

The composition and volume relationship of the metasomatic alteration process was considered by Gresens (1967), who defined equations for calculating gains and losses from chemical analyses. Using Gresens' (1967) method, the interrelationships of volume change, composition and density can be traced between altered and unaltered varieties of the same rock type using the following equation:

$$\Delta m_i = f_v(\rho_a/\rho_0)C_a^i - C_0^i \quad \text{(II.3)}$$

where Δm_i is the mass change in component i, f_v is the volume factor, the ratio of the final volume to the initial volume, $\rho 0$ and ρa represent the original and altered rock densities and C_a^i and C_0^i are the initial and final concentrations of component i. Moreover, $f_v = 1$ indicates constant volume during the alteration process, $f_v < 1$ indicates volume loss and $f_v > 1$ indicates volume gain (Gresens, 1967).

During the alteration, some elements are likely to become immobile in the system, whereas others become mobile. If immobile elements can be identified, they may be used to estimate the volume change involved in the process (Gresens, 1967; Grant 1986). Grant (1986) provided a graphical solution to Gresens' equations, termed the isocon method, by rearranging the equations into a linear relationship between the concentration of a component in the original and altered rocks. Therein, elements that remain immobile must lie on a straight line through the origin, called the isochemical line or isocon (Grant, 1986; Mukherjee and Gupta, 2007; López-Moro, 2012). The immobility of one or more elements is assumed as a reference frame from which the mass transfer calculations are estimated. The slope of the isocon line indicates the mass change of the alteration. Elements that are lost and gained are located below or above the isocon line, respectively (Grant, 1986). Mass-balance modelling was performed using the Microsoft Excel spreadsheet programme EASYGRESGRANT (López-Moro, 2012), which provides correct selection of immobile elements, volume factors, and an improved isocon diagram based on the method of Gresens (1967) and Grant (1986). The mass-balance calculation provides lists of mobile elements, as well as the quantity of volume, and mass change during vein formation and development processes.

The density changes of the shear zone and wall rock were also analysed by evaluating the micro-CT images. The exact separation of small rock bridges is difficult because of their size, but it is necessary for the application of the ordinary density measurement methods.

Nevertheless, CT is a non-destructive procedure allowing the determination of HU values on even micrometre-sized rock volumes, i.e. on a single rock bridge between veins. Since average HU values correlate with density (Kawamura, 1990), manually measured density and HU data of the wall rock and the shear zone can be used for calibrating the density of the rock bridges. To do so, image analysis using the ImageJ (Schneider et al., 2012) image processing software was conducted on the CT images. Consequently, the density of the bridges could be obtained as follows: manually measured densities of the wall rock and shear zone, as well as the average greyscale values were calculated on the CT images of all three domains; assuming a linear correlation between greyscale value and density, the density of the rock bridge can be computed.

The microstructure of the wall rock and rock bridges were analysed by scanning electron microscopy (SEM) using a Hitachi S-4700 field emission instrument, where differences in 2D porosity, grain orientation and grain size could be identified for the two major rock domains. The element distribution maps were acquired using a BRUKER (former RÖNTEC) energy-dispersive device (EDS) attached to the Hitachi S-4700 SEM. The 2D porosity of the wall rock and the rock bridges was determined by image analysis using the ImageJ software on REAs, calculated as explained above.

II.4. Results

II.4.1. Petrography of the veins

Sigmoidal veins occur within 0.5–5-cm-wide shear zones between depths of 280–730 m in the BAF–2 well (Fig. II.6A). The average thickness of veins in the cross-section varies between 0.5 and 1.5 mm, and their aperture can significantly change within one vein (Fig. II.6B). CT images revealed that their 3D geometry is varied, their length spatially exceeded the diameter of the core sample, and thicker veins often joined together with thinner ones.

The shape of the investigated veins often exhibited angular features, triangular vein terminations were common (Fig. II.6A, Fig. II.6B). Several thin planar veins branch away from veins around their tips (Fig. II.6B). This vein shape was different from the typical sigmoidal geometry, which was characterised by the smooth ‘S’ shape. However, in addition to the mentioned angular vein parts, curved segments can also be observed.

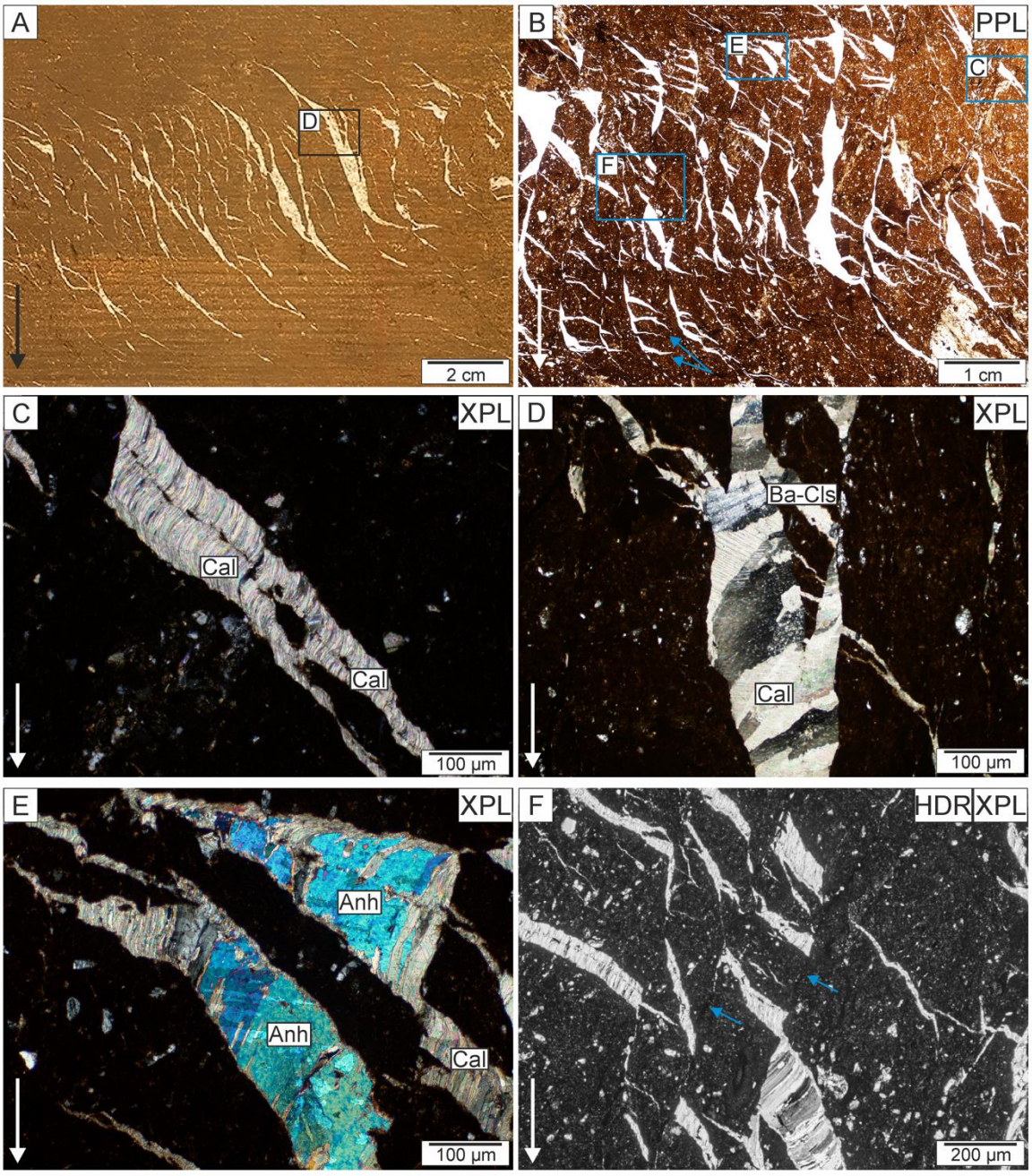

Fig. II.6 Microstructure of the sigmoidal veins. (A) Shear zone with sigmoidal veins in sample BAF–2_500. (B) Vertical veins branching away from the sigmoidal vein in sample BAF–2_657; blue arrows indicate angular vein terminations. (C) Antitaxial vein with fibrous calcite vein filling in sample BAF–2_657. (D) Textural appearance of barite–celestine in the vein in sample BAF–2_500. (E) Anhydrite vein-filling fabric with small calcite crystal remnants enclosed as inclusions in sample BAF–2_657. (F) Shear planes (blue arrows) with rhombus-shaped vein segments in sample BAF–2_657. The arrows in the lower left corners of the images indicate the downward direction of the core. PPL – plane-polarised light. XPL – crossed polarised light. HDR – extreme high-dynamic range image.

The average dip of the zones, which was adjusted according to the inclination of the well, was 22° with low deviations (Hrabovszki et al., 2017). Based on the downward direction of the cores, the orientation of the vein tips, which point in the opposite direction to the shear sense, and the direction of the dip relative to the shear sense, the sigmoidal veins indicate reverse structures.

The major vein-forming minerals are calcite and anhydrite, although barite–celestine occurs in smaller quantities. In most parts, calcite has a characteristic fibrous texture with slightly curved fibres (Fig. II.6C), which show only minor growth competition. As a result of minor growth competition, small widening of the fibrous crystals can be observed in the central part of the veins (Fig. II.6D). The calcite phase exhibits a bright orange CL colour in all samples. Triangular terminations of the veins contain thin curved calcite fibres. In general, calcite crystals fill the veins entirely, whereas barite–celestine is observed only in the centre of the veins. Occasionally, vein-filling fibres consist of barite–celestine across the entire vein (Fig. II.6D). Anhydrite occurs as relatively large monocrystals, which also have fibrous textures, but that is less defined than in calcite (Fig. II.6E). Anhydrite crystals are located in various textural positions. In certain cases, they fill the majority of the veins, but elsewhere, they appear only in small quantities between fibrous calcite crystals. Nevertheless, they regularly enclose small calcite crystal remnants (Fig. II.6E). Median zones consisting of wall-rock fragments can be observed within the mineral filling of the veins (Fig. II.6C). These median zones are not always located in the middle of the veins, indicating asymmetrical vein opening.

Dark fine-grained seams are discernible in the rock bridges in the thin sections (Fig. II.6F). The triangular vein terminations arise from these seams, pointing opposite the shear sense. In some cases, mineral precipitation occurs in rhombus-shaped cavities between the seams (Fig. II.6F). These dark lines are detectable across the shear zone joining together different vein segments and could be interpreted as shear planes. Sometimes, rock bridges in the core of the shear zone contain thin, undulated dark seams, whose orientation is different from the above-mentioned shear planes, they are perpendicular to the vein orientation. Some seam, mainly in the outer part of the shear zone enriched in Ti and Fe according to the EDS images (Fig. II.7), the width range of the seams are between 20 and 40 μm. Most of the dark seams appeared in the microscopic analysis enrichment of elements and marks of pressure solution cannot be found on the SEM images.

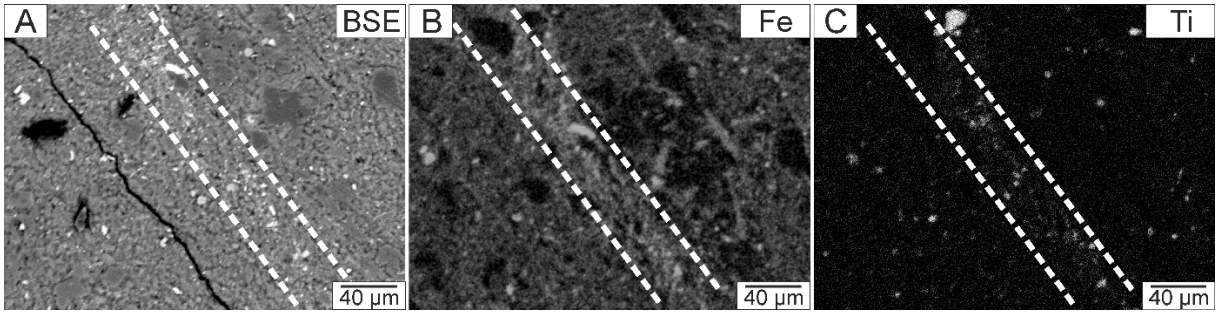

Fig. II.7 Back scattered electron image and element distribution maps measured on the representative elementary area along a fine-grained seam in a rock bridge. (A) Backscattered electron image of the seam. (B) Distribution of Fe. (C) Distribution of Ti. Dashed lines indicate the border of the seam.

II.4.2. Volume change estimations

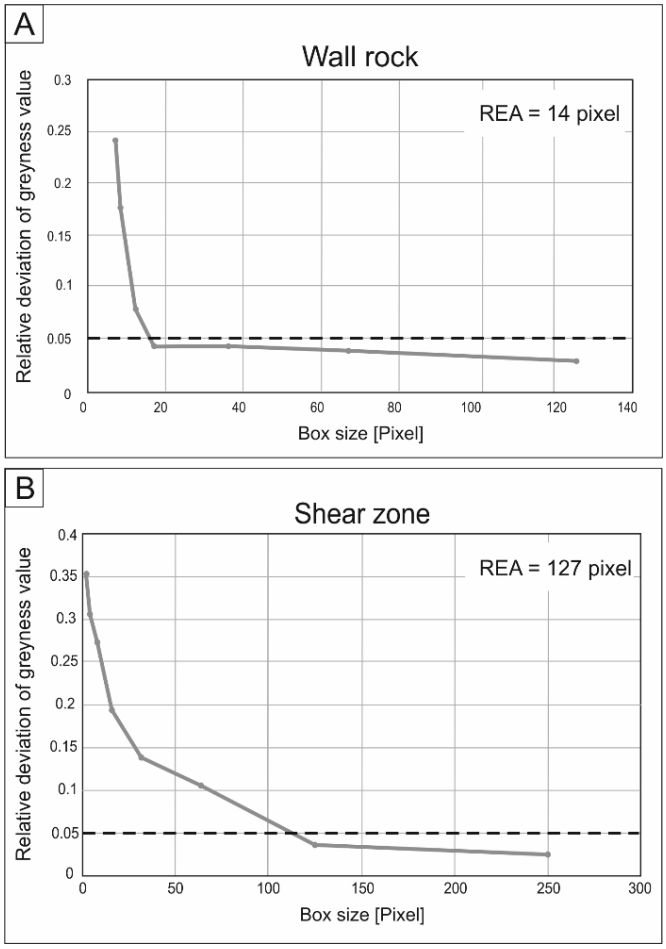

The density and volume change of the shear zones was estimated on REA-sized segments, which significantly differ for the wall rock and shear zone. The wall rock is fine-grained, homogenous claystone; hence, the REA is relatively small for this domain. Moreover, the length of the side of the representative sampling square is ~150 µm. The REA of the shear zone is larger, around 1400 µm, due to the heterogeneity of the veins and rock bridges determined based on the CT images (Fig. II.8).

Fig. II.8 Representative elementary areas (REA) of the wall rock (A) and the shear zone (B) determined by image analysis based on micro-CT images of different domains.

II.4.2.1. Geometric approach

Shear zones of the BAF–2_662 and BAF–2_667 samples were analysed using Lisle's (2013) method for calculating shear strain and the volume change of the shear zone based on

the geometry of sigmoidal veins. Since the passive rotation model demands two differently oriented line markers for shear strain and volume change calculations, two samples were chosen in which sigmoidal vein arrays intersect with straight veins. The results of shear strain and volume change calculations derived from the original and deformed orientations of the straight and sigmoidal veins according to the passive rotation and the folded bridge models shown by Tóth et al. (2018) are presented in Table II.2.

Table II.2 Strain rate and volume change estimates for the shear zones in BAF–2_662 and BAF–2_667 samples based on the geometric approach (Lisle, 2013)

	BAF–2_662	BAF–2_667
Passive rotation model	$\gamma = 0.74$ $\Delta V = -49\%$	$\gamma = 0.73$ $\Delta V = -57\%$
Folded bridge model	$D_x = 0.71$ $\Delta V = -46\%$	$D_x = 0.63$ $\Delta V = -41\%$

Applying the passive rotation and folded bridge models to our samples, the average shear strain is found to be approximately $\gamma = 0.7$, corresponding to intermediate shear strain. Volumetric estimations suggest a ca. 50% volume loss for both samples. These results appear unaffected by the choice of the kinematic model.

4.2.2. Mass-balance analysis

Another approach to determine the volume change of the shear zone is mass-balance analysis of the system (Gresens, 1967; Grant, 1986). Mass-balance analysis was conducted on sample BAF–2_500, for which the average density of the wall rock is 2.53 g/cm^3 and the density of the shear zone is 2.89 g/cm^3; values were determined using the water displacement method. All chemical, mass and density changes of the wall rock and the shear zone were compared using the isocon method (Grant, 1986). Ti was chosen as an immobile element during the mass transfer computations. The results reveal that the shear zone became enriched in Ca, Ba, S, Sr and Mn (Fig. II.9). Other major and trace elements, as well as the REEs, were located near to the isocon line, suggesting that the deformation process caused no changes in the concentration of these elements (Fig. II.9). According to these calculations, mass transfer resulted in a +9% mass change in the shear zone. Despite the positive mass change, the shear zone bore a 5% loss in volume.

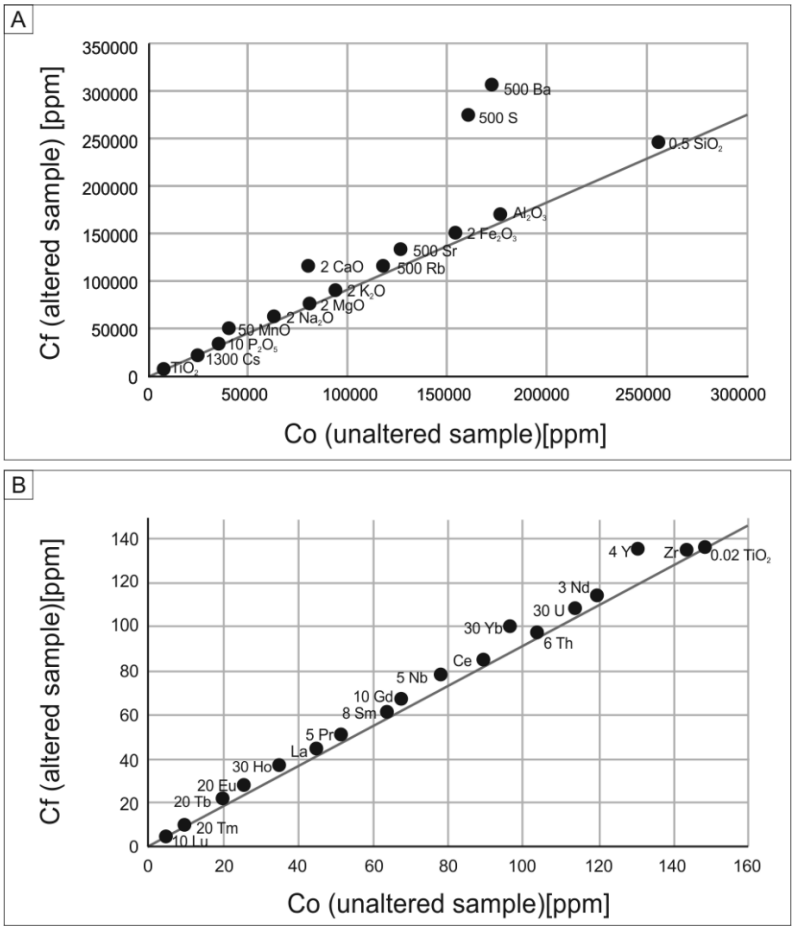

Fig. II.9 Isocon analysis of the shear zone: Co, concentration for unaltered samples; Cf, concentration for altered samples. The concentration of elements located on the isocon line is unchanged, elements above the line are enriched in the altered sample, and elements under the isocon line are depleted in the altered sample. Concentrations of the major elements and elements of the rock-forming minerals are presented in the first diagram (A); concentrations of the rare-earth elements are presented in the second diagram (B). Numbers before element names are scaling factors, e.g. 2CaO.

4.2.3. Density-change evaluation

To study the density change, the three rock domains were analysed using micro-CT. The average grey colours of the wall rock, shear zone and rock bridges were determined and correlated with densities derived from traditional density measurements. Since micro-CT is a non-destructive method with high spatial resolution, it allows the analysis of the rock bridges alone. The density of the rock bridges is estimated at 2.76 g/cm^3 based on micro-CT values (Fig. II.10). Using this value, the bridges suggest a density increase of ~8% compared with the wall rock.

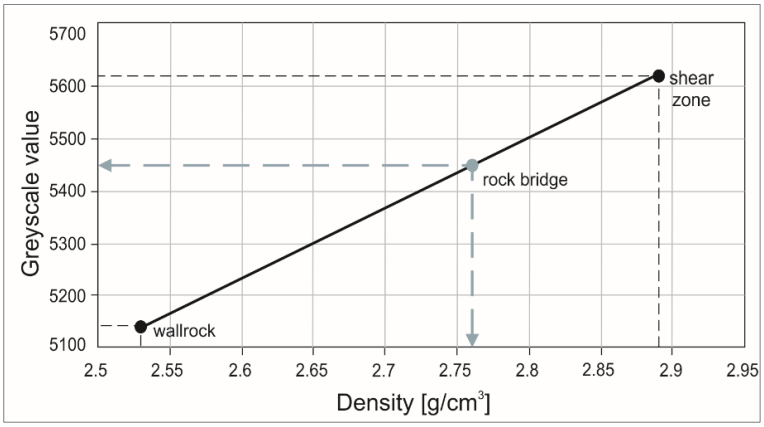

Fig. II.10 Density calculation of the rock bridges based on greyscale values of the two main domains in micro-CT images.

Analysis of SEM images, based on the selected REA (~4400 µm), gives 1.6% 2D porosity (φ) for the wall rock and 0.8% for the bridges, i.e. a 50% loss of porosity in the bridges due to deformation (Fig. II.11).

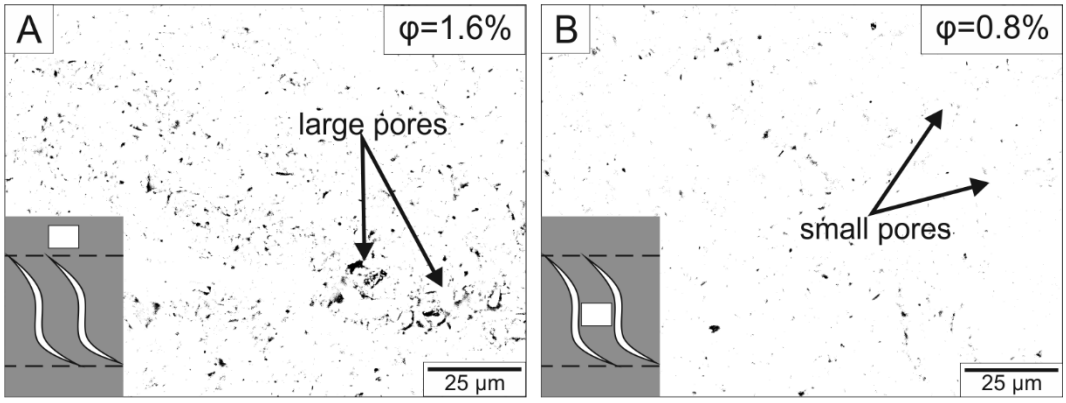

Fig. II.11 Average 2D porosity (φ) of the representative elementary area (REA) segments of (A) the wall rock and (B) the rock bridge on binarised SEM-BSE images. Drawings in the left corners indicate the positions of the analysed areas in the shear zone. The wall rock contains larger, connected pores, whereas the rock bridges enclose small, separate pores.

II.5. Discussion

II.5.1. Microstructure and evolution of sigmoidal veins

En échelon veins were previously examined mostly in carbonates (Beach, 1975; Rothery, 1988; Seyum and Pollard, 2016) and sandstones (Hancock, 1972; Rickard and Rixon, 1983; Nicholson, 1991; Smith, 1995; Lisle, 2013; Thiele et al., 2015). These authors investigated the formation process of these veins and found that it was influenced by the composition of the host rock itself through pressure solution of the rock-forming minerals. The

samples analysed herein derive from the BCF; more than 200 sigmoidal vein arrays were detected in the BAF–2 well alone. They all occur in claystone, which has different rheological features from the lithologies mentioned in the above papers.

Described triangular vein terminations can be derived from different kinematics (Swanson, 1992; Willemse and Pollard, 1998; Coelho et al., 2006). We propose that the formation of the investigated vein arrays can be related to that of pennant veins (Coelho et al. 2006). Coelho et al. (2006) described pennant veins, which have distinct triangular pennant-shaped vein terminations, and their kinematics are controlled by Riedel conjugate sets of fractures (Fig. II.12). The triangular space, which is filled with minerals, is obtained by rotation and slip of the operating shear fractures.

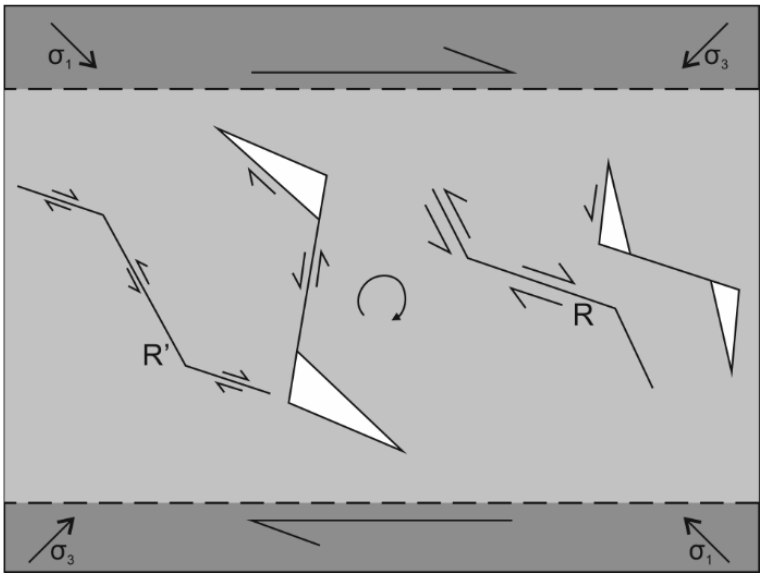

Fig. II.12 Development of pennant-shaped veins controlled by R and R' Riedel fractures. These fractures rotate and slip during progressive deformation, opening pennant-shaped gaps (modified after Coelho et al., 2006).

In our case, the vein-filling calcite fibres of the triangles are curved, indicating shearing during the crystal growth (Fig. II.13A inset 'a'). The triangular terminations (Fig. II.13B inset 'b') arise from the dark seams, which can be attributed to the localised shear planes possibly formed from initial flaws (Willemse and Pollard, 1998; Fig. II.13B inset 'c'). Between these shear planes, rhombus-shaped vein segments can open (Fig. II.13A inset 'd'), during the evolution of the shear zone these vein segments and vein tips could rotate and bend (Fig. II.13A inset 'e'). Mineral precipitation can also occur in the middle parts of the shear planes when the orientation becomes favourable for vein opening by rotation induced by the shear zone (Fig. II.13B inset 'f'). The sigmoidal shape could have been formed by the connection of these vein segments via rotation and continuous mineral precipitation.

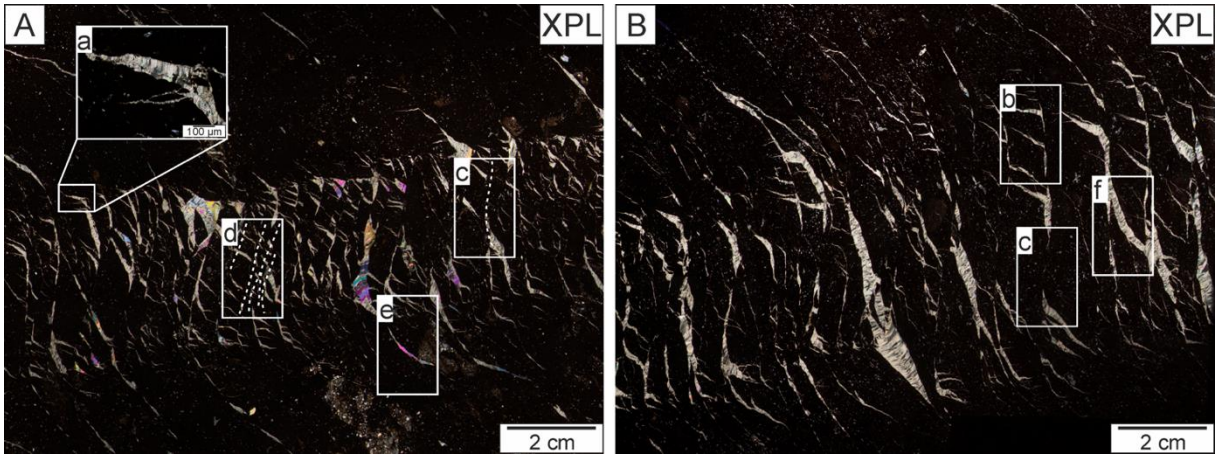

Fig. II.13 Formation mechanism of the sigmoidal veins. Shear zone in cross-polarised light (A) in sample BAF–2_657 and (B) sample BAF–2_500. (a) Curved calcite fibres in the vein tips. (b) Triangular vein terminations of the veins. (c) Initial flaws, which develop to shear planes, in many cases without mineral-fillings. (d) Rhombus-shaped segments, which opened as a result of the adjacent shear planes. (e) Tips of the veins bend as the shear zone develop. (f) Significant mineral precipitation occurs in the central part of the shear zone when their orientation became favourable for vein opening. Dashed lines indicate the shear planes. XPL – crossed polarised light.

In our samples, the dominant vein filling of the sigmoidal veins is fibrous calcite with anhydrite and barite–celestine in minor quantities. The fibrous morphology of the calcite and the systematic presence of the middle line in the veins indicate antitaxial vein growth morphology. No common growth competition texture is presented; therefore, crystal precipitation and fracture opening probably occurred simultaneously (Means and Li, 2001; Wiltschko, 2001; Barker et al., 2006). Crystal fibres in antitaxial veins usually follow the opening trajectory of the fracture (Bons et al., 2012). Calcite crystal habits, together with the relative positions of barite–celestine crystals, indicate that they grew simultaneously with vein opening. Based on the habit of the anhydrite and calcite inclusions, the anhydrite phase resulted from post-kinematic replacement of the calcite phase (Fig. II.6E).

The size of the shear zones, vein shape, and their shear sense relative to their dip are unified. The vein-filling sequence in each studied sigmoidal vein arrays is similar. The crosscutting relationship within the studied depth interval is uniform, and the sigmoidal vein arrays ($Vein_{ECH}$) are the youngest of the three vein generations in each situation.

Such structural inhomogeneities and fracture planes could behave as fluid migration pathways in the rock body; therefore, detailed analyses of each vein generation and recent hydrodynamic behaviour of the fracture system are essential (Gentier et al., 2000). Based on the 3D geometry of the shear zones, more evolved hydrological interconnectivity can be

achieved through these veins, which is more significant than that predicted from the cross-sectional geometry. However, the lateral extension of the shear zones outside the well is not known.

Because sigmoidal veins with similar attributes occur throughout the depth of the well, the formation of these veins could be related to the same deformation event, which had a significant effect on the whole BCF. The shear sense of the shear zones, the direction of dip relative to the shear sense and the known upward direction of the cores suggest development during a compressional stress field. The position of the arrays relative to the bedding is unknown; nevertheless, the dip of the arrays is almost constant throughout the BAF–2 well. Thus, the formation of the veins is not older than the tilting and folding of the formation caused by the prevailing compressional stress field in the Late Cretaceous (Benkovics et al., 1997; Haas and Péró 2004). This event generated folds with a NE–SW axis orientation, which are characteristic in the Mecsek Mountains and accompanied by thrust faulting in the BCF (Wein, 1967; Maros et al., 2000).

II.5.2. Evaluation of volume change estimations

The three tested methods of volume change estimation used (the geometric approach, isocon method and density approach) exhibit significantly different rates of volume loss (Table II.3).

Table II.3 The observed features of the shear zones based on three different

	Volume change of the shear zone	Average density of the domains	Other observations
Geometric approach	−50%	-	-
Mass-balance calculation	−5%	Wall rock: 2.53 g/cm^3 Shear zone: 2.89 g/cm^3	Shear zone enriched in Ca, Mn, Ba, Sr, S Mass change +9%
Density-change approach	−8%	Rock bridge: 2.76 g/cm^3	Porosity in the rock bridges is decreased by 50%

The results of the mass-balance and the density-change calculations are similar (5% and 8%, respectively); however, the geometric method suggests a significantly larger volume reduction (~ 50%). The reason for this difference could be related to the different principles of the three approaches. The geometric method (Lisle 2013) was introduced on sandstones and uses exclusively vein shape parameters. Thiele et al. (2015) suggested that the effects of

pressure solution within the shear zones are crucial in vein development. Along the pressure solution seams, slight rotation and slip could occur, which influence the geometry of the veins. Consequently, the veins become highly sigmoidal without substantial rotation or bending; therefore, if pressure solution was active then the volume change and strain calculations based on the geometry of the veins will overestimate (Thiele et al., 2015).

While pressure solution is an important process in sandstones (Toussaint et al., 2018), its role is less critical in claystones because of their poor solubility under low-temperature physicochemical conditions (Rutter, 1983). In the BAF samples seams frequently appear as thin dark-coloured lines under a polarising microscope in the rock bridges in two orientations. One of them, which the triangular and rhombus-shaped vein segments arise from, possibly represent shear planes (DS_{SP}) according to the evolution of pennant-shaped veins (Coelho et al., 2006). Element enrichment and marks of pressure solution cannot be traced in the SEM images. The other group of dark seams (DS_{PS}), which are perpendicular to the vein orientation, show enrichment of certain elements (Fe, Ti) based on EDS images. As pressure solution can be observed along certain dark seams only, we suppose that the effect of pressure solution along the shear zone was subordinate. Additionally, the reduced effect of pressure solution is confirmed by the fact that the mass-balance calculations did not show any element depletion in the shear zone.

Our calculations suggest that the application of the geometric approach in rock types for which rheological and petrophysical properties are different from those typical in sandstones (siltstones and claystones in the present case) leads to an unrealistic result (~50%). Moreover, the proposed vein formation process namely, the pennant-shaped vein forming mechanism significantly differs from those, which are responsible for the development of regular tension gashes. Thus, the volume change and strain calculations based only on the geometric approach may provide misguided results.

According to the coinciding results of two other volume change estimations–the isocon method and the density approach–the shear zones underwent a low-rate volume loss. Based on the isocon method, despite the volume loss of the shear zone, its mass increased. Assuming Ti as immobile for the isocon calculation (Maclean and Kranidiotis, 1987; Gong et al., 2016), the shear zone became enriched in Ca, Mn, Ba, Sr and S relative to the undeformed host rock (Table II.3.). All other studied elements behaved in an immobile manner. Considering the mineralogical composition of the veins, the increase in Ca probably derived from the calcite and anhydrite, whereas the minor amount of barite–celestine vein-fillings was responsible for the increases in Ba and Sr concentration. Most probably S gain derived from sulphate phases, anhydrite, barite and celestine. The cathodoluminescent activity of the calcite phase confirms

the Mn content of the calcite (Götze, 2012). All precipitating mineral phases may have been responsible for the mass increase observed in the shear zone, although the shear zone carries 5% volume loss. Therefore, the rate of volume loss in the shear zone must have been higher than the overall volume gain caused by the vein formation.

Based on the above calculations, the evolution of the shear zone can be divided into three main stages. Two of these stages, namely, fracture opening and mineral precipitation inside the veins, are responsible for the increases in volume and mass, respectively. Nevertheless, since the total volume decreased along the shear zone proven by the mass-balance calculations, there must be additional processes causing volume loss.

The results of the micro-CT analyses and density calculations detailed above indicate that the density of the rock bridges is significantly higher than that of the wall rock (2.76 and 2.53 g/cm^3, respectively), suggesting different mineralogies and/or porosities and/or chemical compositions in the two domains.

The rock bridges show ~50% lower 2D porosity than the wall rock, based on SEM-BSE images (0.8% and 1.6%, respectively), which indicates that the volume loss of the shear zone took place in the rock bridges and occurred by porosity reduction. Considering all of these results together, we believe that tectonic compaction inside the rock bridges is an essential process for significant volume loss in the deformed portion of the studied claystone. Further processes could cause volume loss in the bridges, such as grain size reduction and reorientation of grains. Tectonic compaction caused a more significant effect on volume change than fracture opening, whereas compaction and subordinate pressure solution was responsible for the volume decrease and fracture opening caused volume increase in the shear zone.

II.5.3. Conceptual model of the development of a shear zone in the BCF

The formation of the sigmoidal vein arrays is associated with the development of shear zones. We propose that vein arrays formed from initial flaws (Fig. II.14A), where pennant-shaped vein termination could form with conjugate Riedel shear fractures (Fig. II.14B). The rotation and bending of these flaws resulted in the sigmoidal veins with triangular vein terminations (Fig. II.14C). The evolution of the veins was accompanied by porosity reduction in the rock bridges. The primary, syn-kinematic vein-filling phase, mainly calcite and barite–celestine is present in minor quantities (Fig. II.14B). The fibrous morphology of the calcite and middle zone of the vein indicate antitaxial vein growth. Vein-filling calcite was post-kinematically replaced by anhydrite (Fig. II.14C).

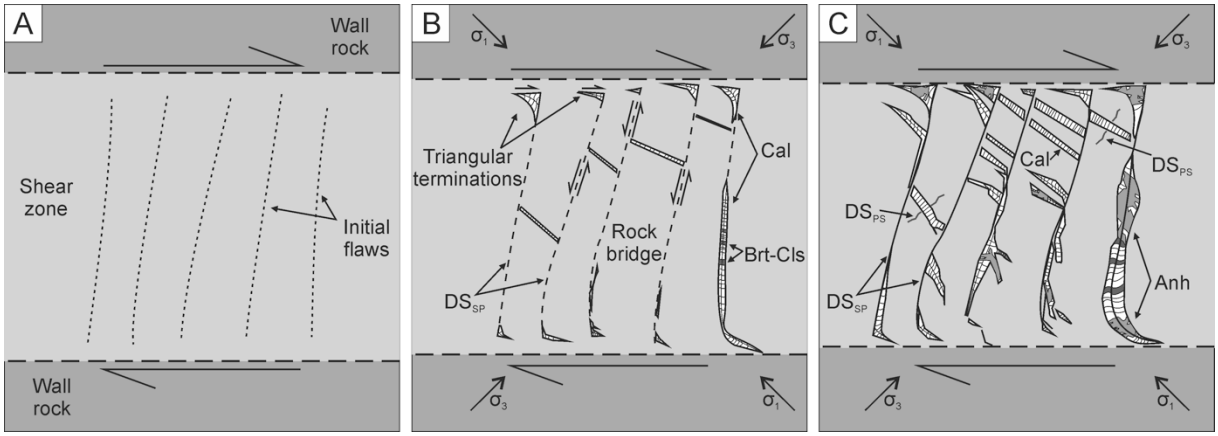

Fig. II.14 Conceptual model of the evolution of the studied shear zones. (A) Presumably, initial flaws of unknown origin are located in the shear zone. (B) During the evolution of the shear zone, triangular terminations form with Riedel conjugate fractures and the initial flaws are working as shear planes. Fibrous calcite and barite-celestine are precipitated in the veins. Parallel to the evolution of the shear zone, the porosity of the rock bridges decreases, which cause volume loss in the shear zone. (C) As a result of shear strain, the fractures rotate and buckle and that resulted in the formation of 'S' shape of the veins. Significant mineral precipitation occurs also in the middle part of the zone when the orientation becomes favourable for vein opening. Subsequently the vein filling sequence was partially replaced by anhydrite. DS_{PS}- dark seams with element enrichment. DS_{SP} – shear planes.

II.6. Conclusions

Sigmoidal *en échelon* arrays were examined in the Late Permian BCF, Hungary, in which more than 200 sigmoidal vein arrays were detected along the BAF–2 well, which penetrated most of the utmost thickness of the formation. The formation of these vein arrays is associated with the development of shear zones. Based on the detailed microstructural analysis, the veins are interpreted as pennant-veins, their kinematics are controlled by Riedel conjugate fractures.

Volume change of the shear zone was conducted using three different approaches, the geometric approach, mass-balance analysis and density-change approach, each of which estimated different rates of volume change. Nevertheless, the studied shear zone undoubtedly went through volume loss. The result of the geometric approach indicates a large volume loss; however, the isocon method and density approaches yield a volume loss in the shear zones of <10%. It appears that the application of the geometric approach, which considers only the shape of the veins without considering the role of other processes can lead to an unrealistic result. Therefore, we propose low rates of volume loss in the shear zones based on the results of the

other two methods. Considering these observations, the sigmoidal veins studied are among the youngest structures of the BCF. The genesis of sigmoidal veins could be related to a Cretaceous compression event accompanied by thrust faulting.

CHAPTER III.

DISCRETE FRACTURE NETWORK (DFN) MODELLING OF A HIGH-LEVEL RADIOACTIVE WASTE REPOSITORY HOST ROCK AND THE EFFECTS ON ITS HYDROGEOLOGICAL BEHAVIOUR

Emese Tóth

Department of Mineralogy, Geochemistry and Petrology, University of Szeged, Hungary

tothemese@geo.u-szeged.hu

Ervin Hrabovszki

Department of Mineralogy, Geochemistry and Petrology, University of Szeged, Hungary

hrabovszkiervin@geo.u-szeged.hu

Félix Schubert

Department of Mineralogy, Geochemistry and Petrology, University of Szeged, Hungary

schubert@geo.u-szeged.hu

Tivadar M. Tóth

Department of Mineralogy, Geochemistry and Petrology, University of Szeged, Hungary

mtoth@geo.u-szeged.hu

Journal of Structural Geology

Volume 156, 2022, 104556

DOI 10.1016/j.jsg.2022.104556

Discrete fracture network (DFN) modelling of a high-level radioactive waste repository host rock and the effects on its hydrogeological behaviour

Emese Tóth, Ervin Hrabovszki, Félix Schubert, Tivadar M. Tóth

Abstract

Fracture network modelling and a hydrological evaluation were performed in a well more than 900 m deep that penetrated the Boda Claystone Formation, a potential host rock for high-level nuclear waste disposal facilities in Hungary. The fracture network geometry was generated with a discrete fracture network algorithm, in which the permeability and porosity of the system can be calculated if the aperture of the fractures is known. The hydrological aperture of the fractures was estimated via an aperture calibration based on a comparison of the measured and modelled permeability values. Flow zone indices were calculated for numerous sections along the well, designating hydraulic units, in which the fluid flow-controlling properties are internally even. Based on the fracture network geometry and the hydraulic flow units, most parts of the well behave uniformly, while three narrow zones differ significantly. The first zone is located in the upper 100 m of the well probably formed due to weathering. The second zone is located at approximately 400 m, where a large-scale structural boundary is presumed. In the third zone at 700 m, a lithological change greatly affects the hydrological properties, but the influence of tectonic processes cannot be ruled out.

III.1. Introduction

The potential host rock for the high-level radioactive waste repository of Hungary is the late Permian Boda Claystone Formation (BCF), which is located in the Mecsek Mountains, SW Hungary (Konrád and Hámos, 2006). The characteristics of this claystone provide good retentive properties, and its low porosity and permeability can prevent the leakage of radionuclides (Krauskopf, 1988; Árkai et al., 2000). In this lithology, significant fluid pathways can exclusively form along planes of structural inhomogeneities and fractures (Anders et al., 2014). Therefore, the investigation of the fracture network geometry and its hydrodynamic behaviour is crucial in understanding the hydrodynamic behaviour of otherwise impermeable rock bodies. Vital areas of study include the connectivity of the fracture system, whether or not single fractures form communicating networks, and the size and location of all potential fracture clusters.

The size of hydrologically active fractures is usually within the resolution of seismic data but transcends the resolution of well log and microstructural studies (Paillet et al., 1993; Childs et al., 1997). Therefore, little information is available about the behaviour of fracture systems at the reservoir scale. Since fracture networks can be approximated as scale-invariant geometrical objects, structural data measured at microscales can be upscaled to larger dimensions (Turcotte, 1992; National Research Council, 1996). Such a discrete fracture network (DFN) modelling approach requires quantitative geometric data of the fracture network, such as the fracture size distribution, spatial density of fracture midpoints, and orientation (dip and dip direction). The essential features of the fractured rock body, such as the connectivity tendency of single fractures as well as the hydrodynamic behaviour of the system (fractured porosity and permeability), can be investigated using simulated models (M. Tóth and Vass, 2011).

This paper aims to characterise the fracture network geometry and the hydrodynamic behaviour of the surroundings of the deepest well (BAF–2) in the BCF using fracture network modelling and evaluating hydraulic measurements in the well.

III. 2. Geological setting

The late Permian BCF is located in SW Hungary (Fig. III.1) and is a member of the 4000–5000 m thick Paleozoic–Triassic sedimentary sequence of the Western Mecsek Mountains. The formation consists of well-compacted reddish-brown claystone, siltstone, and albitolite (authigenic albite >50%) with dolomite and sandstone intercalations. The main rock-forming minerals are quartz, albite, illite-muscovite, chlorite, calcite, dolomite, and haematite (Árkai et al., 2000; Máthé, 2015). The maximal thickness of the formation is more than 1000 m and the distribution area is approximately 150 km^2 (Konrád and Hámos, 2006). The BCF was deposited in an alkaline lake environment on a periodically drying playa mudflat in an arid to semiarid climate (Árkai et al., 2000; Varga et al., 2005; Varga et al., 2006; Varga, 2009; Konrád et al., 2010).

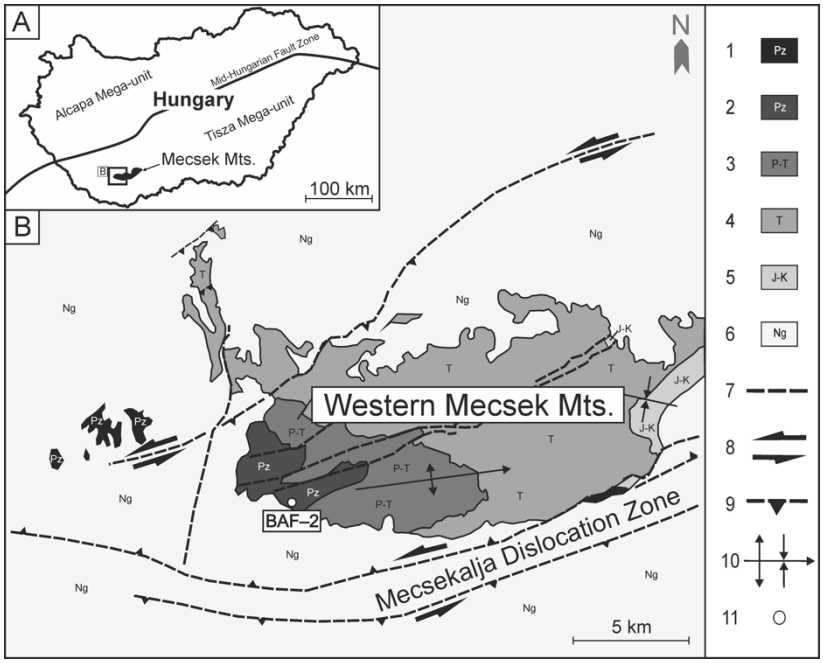

Fig. III.1 (A) Map of Hungary with the location of the Mecsek Mountains. (B) Geological map of the Mecsek Mountains with the distribution of the Boda Claystone Formation (modified after Konrád and Sebe, 2010) Legend: 1, Palaeozoic; 2, Upper Permian Boda Claystone Fm; 3, Upper Permian–Triassic Kővágószőlős Sandstone Fm; 4, Triassic sediments (sandstones, carbonates and evaporites); 5, Jurassic and Cretaceous sediments and Cretaceous volcanic rocks; 6, Neogene sediments; 7, fault; 8, strike-slip fault; 9, thrust fault; 10, syncline and anticline; 11, well site.

The study area is located around the subvertical profile of the BAF–2 well, which penetrated the formation in largest thickness of more than 900 m, with close to 100% core recovery. The well intersected characteristic reddish-brown, intensely tectonised claystone. The average dip direction of the bedding in the well is SE-SSE, and the dip is 40° based on acoustic borehole televiewer (BHTV) observations (Bernáth et al., 2014; Konrád et al., 2015).

The grain size gradually increases with depth (claystone - siltstone - fine sandstone). Above the Permian sequences, the BAF–2 well penetrated Quaternary (Holocene, Pleistocene) sediments between 0 and 9.10 m (reported depths are in the total measured depth in metres throughout the paper; Fig. III.2A). Between 9.10 and 130 m, reddish-brown claystone with interbedded siltstone is the dominant rock type. This section is intensively weathered; presumably, the rock body was uncovered for an extended period of time in a warm and humid climate before and during the Miocene (Konrád et al., 2015). As a significant alteration product, limonite is present in the uppermost 100 m of the well. The section between 130 and 757 m consists of reddish-brown claystone with siltstone beddings. Between 148.59–153.90 and 233.36–238.40 m, the well crosscuts two thick reductive layers; in these intervals, the sequence

contains greenish-grey claystone (Fig. III.2A). Presumably, these layers represent two independent reductive events. Based on the interpretation of the BHTV data, the tectonic repetition of the same horizon cannot be ruled out either (Bernáth, 2015; Konrád et al., 2015). The first fine sandstone layer of significant thickness appears at 757.96 m. Below this horizon, the transition zone of the BCF to its coarser-grained bedrock is identified. In this interval, claystone with numerous siltstone and fine sandstone intercalations is the dominant rock type (Fig. III.2A; Konrád et al., 2015).

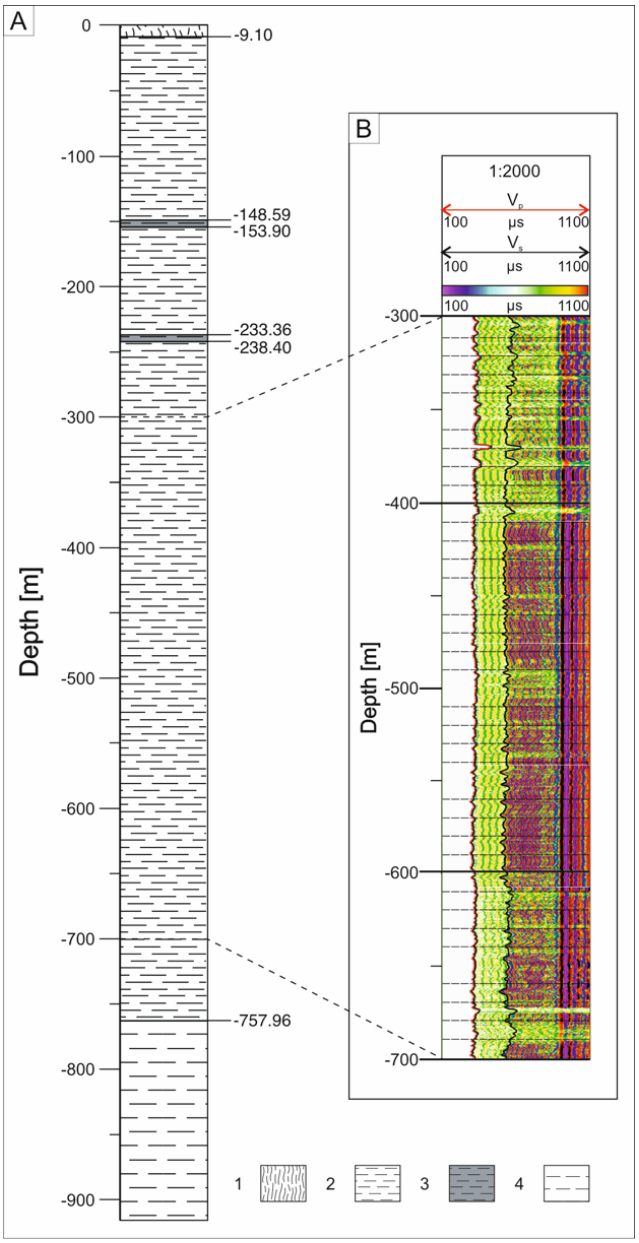

Fig. III.2 (A) Lithology log of the BAF–2 well; 1, soil, loess; 2, claystone with siltstone beddings; 3, greenish-black reductive claystone; 4, claystone with siltstone and sandstone beddings (modified after Hrabovszki et al., 2017). (B) Sonic log for the BAF–2 well between 300 and 700 metres. Red line indicates the velocity of the primary waves, black line indicates the velocity of the secondary waves (modified after Bernáth et al., 2014).

Numerous subsequent tectonic phases could characterise the evolution of the area. Significant NE–SW shortening during the Late Cretaceous (Benkovics et al., 1997) was followed by events related to the formation of the Pannonian Basin in the Neogene. Deformation due to tensional stresses in the early Miocene (Bergerat and Csontos, 1988; Csontos and Bergerat, 1992; Fodor et al., 1999) was followed by late Miocene (Sarmatian)

compression (Sebe, 2017) and by thermal subsidence of the basin afterwards (Pannonian; Csontos et al., 2002; Maros et al., 2004). The most recent essential event is the ongoing tectonic inversion of the basin (Konrád and Sebe, 2010).

Konrád et al. (2015) suggest a structural boundary at approximately 400 m in the BAF–2 well. Below this depth, the graded bedding style changes from normal to inverse, and thinning of the graded sequences is observed. In this segment, the sequence contains numerous smaller strata interpreted as overturned.

Many geophysical well logs show a characteristic difference between the upper (0–400 m) and lower (400–915 m) parts of the well. The most significant deviation is shown in the sonic log (Fig. III.2B), where the acoustic wave velocity drastically decreases below 400 m (Bernáth et al., 2014). This log indicates the mechanical properties of the rock body by measuring how fast the acoustic waves can travel through the rock body. Based on all this information, the current structural interpretation of Konrád et al. (2015) suggests that the BAF–2 well intersected a tilted fold sheared by fault zones.

Previous studies distinguished four vein generations along the BAF–2 well that indicate multiple tectonic and/or diagenetic processes (Hrabovszki et al., 2017, 2020, 2022; Tóth et al., 2020). The veins are classified into the following categories: branched veins, straight veins, *en échelon* vein arrays, and breccia-like veins. In the BAF–2 well, the average dip values of the vein types are 42° (branched veins), 70° (straight veins), and 22° (*en échelon* vein arrays) (Hrabovszki et al., 2017). All four vein generations occur all along the rock body. The fractures are filled predominantly with calcite, anhydrite, and barite-celestine (Árkai et al., 2000; Hrabovszki et al., 2020, 2022; Tóth et al., 2020).

Accurate knowledge of hydrogeological conditions is an essential requirement for assessing the suitability of a geological formation for the storage of radioactive waste. The general hydrogeological conditions of the Western Mecsek Mountains are determined by the morphology of the mountains and their surroundings. The Paleozoic–Mesozoic formations of the mountains rise 400–500 m from their surroundings, defining a regional recharge zone whose discharge areas are the Neogene basins located in its wider periphery (Csicsák, 1999).

Due to its petrophysical properties and thickness, the BCF is an aquiclude. Due to its high clay content, fracture self-sealing is also a frequent phenomenon (Csicsák, 1999). In its surface outcrops, the rock body is relatively well fragmented and significantly weathered; therefore, groundwater amounts can be significant in the uppermost 40–50 m. Based on hydraulic testing of the well, transmissivity decreases with depth; however, high-transmissivity zones also occur, even in the deeper parts (down to approximately 500 m). The well can be divided into two parts based on the transmissivity log. High-transmissivity zones occur mainly

in the upper 500 m, while below 500 m, the transmissivity is close to constant at a significantly reduced value throughout the well. The highest value is 1.9×10-5 m2/s, while the lowest value is 2.7×10-12 m2/s (Fig. III.3; Andrássy et al., 2018).

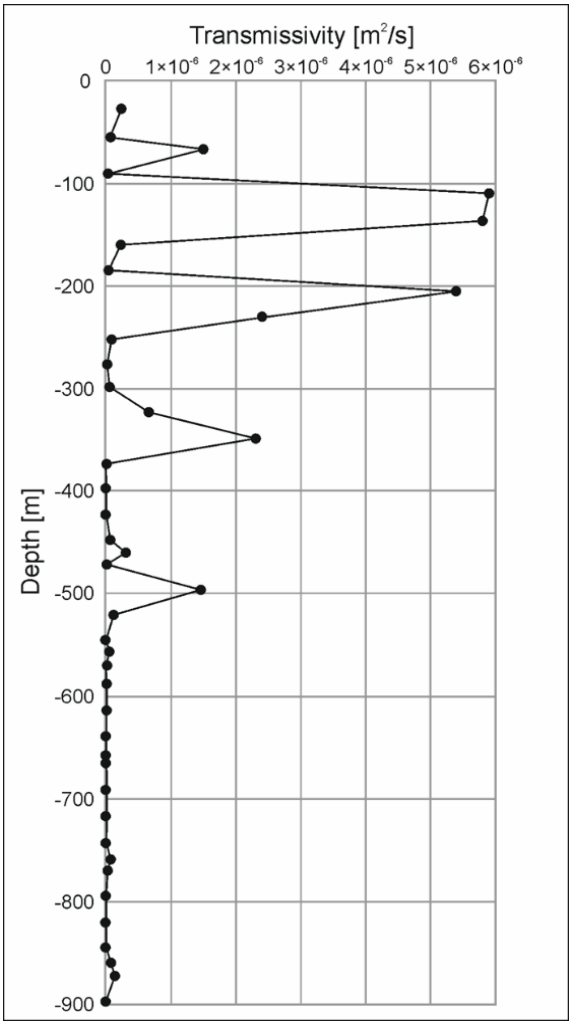

Fig. III.3 Transmissivity log of the BAF–2 well based on well-hydraulic testing (Andrássy et al., 2018).

III.3. Methods

Fracture networks usually follow a fractal-like pattern independent of the lithology and structural evolution (Barton and Larsen, 1985; La Pointe, 1988). Such an appearance allows fracture networks to be modelled at any scale using measured geometric data. In this study, a discrete fracture network (DFN) modelling approach was used to predict the hydrodynamic behaviour of the rock body based on the geometric data of the individual fractures (Witherspoon et al., 1980; Neuzil and Tracy, 1981; Zimmerman and Bodvarsson, 1996).

DFN modelling has two consecutive steps. First, the geometric parameters of the individual fractures must be determined. These parameters serve as the foundation for the simulation. The most important geometric parameters and those used in the modelling are the

fracture length distribution, the spatial density of fracture midpoints, the orientations of the fractures, and their aperture. Second, the network is generated using a fracture modelling software program. In this study, the discrete fracture network modelling system called Infress (previously RepSim) was applied (M. Tóth et al., 2004; M. Tóth, 2010, 2018).

III.3.1. Determination of the geometric parameters of fractures

Fracture size is one of the essential geometric parameters of DFN modelling. Numerous studies have shown that the distribution of fracture lengths follows a power-law function so that

$$\mathrm{N}(L) = F * L^{-E} \qquad \text{(III.1)}$$

where *N(L)* is the number of fractures with a length of *L* and *E* and *F* are the parameters of the distribution function (Yielding et al., 1992; Min et al., 2004). This asymmetric distribution denotes that the number of small fractures is significantly larger than the number of large fractures.

Measurement of fracture length cannot be easily performed on cores because most individual fractures do not terminate within the core. To solve this problem, M. Tóth (2010) introduced a novel algorithm. Here, two images with different sensitivities are required to determine the length exponent (*E* in Eq. III.1). The number of fractures identified by the less sensitive method is necessarily less than the number of fractures seen by the more sensitive method, with a constant difference (*ΔN(L)*). Using this difference and the detection limits of the applied methods, the parameters of Eq. III.1 can be calculated. For further details, see M. Tóth (2010). In our study, the length exponent was determined using BHTV data (lower resolution) and core images (higher resolution). The vertical resolution of the BHTV is 4 mm, while the resolution of the core images is 1 mm.

The spatial density of the fracture network can be defined by the fractal dimension of the fracture pattern. In a borehole, the real fracture network is crosscut by a line (defined by the well itself), resulting in a point series. In this case, the spatial density of the fractures can be characterised by computing the fractal dimension of this series. As the borehole image logs (e.g., BHTV) define the exact spatial position of fractures, the intersection points between the fracture network and the borehole can be interpreted as the point process in question. The fractal dimension of this pattern was calculated using rescaled range (R/S) analysis, which aims to estimate the Hurst exponent. The degree of self-similarity is defined by the Hurst exponent (*H*) parameter, which is directly related to the fractal dimension so that:

$$D = 2 - H \qquad \text{(III.2)}$$

The parameter *H* was determined for each 100 m interval with an overlap of 50 m (0–100 m, 50–150 m, 100–200 m, etc.) along the well using Benoit 1.0 software following the approach introduced by M. Tóth (2010). In addition to the fractal dimension, another commonly used parameter that may also characterise the fracture density is the P10 parameter (number of intersections per metre), which was also calculated and plotted with depth. The orientations of the fractures were described by the dip direction and dip angle obtained from the BHTV data.

III.3.2. Fracture network modelling and aperture calibration

The fracture network of the investigated well was generated in 3D by Infress fracture network modelling software (M. Tóth, 2010; Tóth and Vass, 2011; Bauer and M. Tóth, 2016). This DFN software package simulates single penny-shaped fractures in a stochastic manner with the given geometric parameters of the fracture network. Infress generates the desired number of equally probable realisations of the fracture network geometry. A subroutine of the software code enables the investigation of the size and spatial position of the communicating subsystems of the simulated fracture networks (M. Tóth and Vass, 2011). Based on the fracture network geometry and an aperture value for all fractures, the fractured porosity and the intrinsic permeability tensor elements can be computed for any cubic volume element of the modelled rock body. The algorithms and the mathematical background of the software code are described in detail by M. Tóth (2018).

Determining and even defining the fracture aperture are somewhat problematic (Vermilye and Scholz, 1995; Keller, 1998; Liu, 2005; Bisdom et al., 2016). The physical aperture is usually defined as the average distance between the opposite walls of the fracture that can be measured using an image analysis approach at any scale. In hydrodynamic processes, the hydraulic aperture should be used instead, which is defined as a theoretical conduit that produces the same flow rate as the real fracture (Olsson and Barton, 2001; Cheng et al., 2020).

Furthermore, the fracture aperture should not be defined as an independent geometric parameter. It usually follows a power-law distribution function, similar to the fracture length, and a tight linear correlation can be assumed between the two parameters based on numerous studies (Barton and Larsen, 1985; Pollard and Segall, 1987; Gudmundsson et al., 2001):

$$a = A * L \qquad \text{(III.3)}$$

where *a* is the aperture, the aperture coefficient *A* is characteristic of the rock body, and L is the length of the fracture, which is the diameter of a theoretical penny-shaped fracture in the model. In many different rock types, the ratio of the maximal aperture to the length varies within

approximately 2×10^{-3}–8×10^{-3} for joints and 3×10^{-3}–3×10^{-2} for shear fractures (Opheim and Gudmundsson, 1989; Vermilye and Scholz, 1995). Using this simple correlation, the initial aperture for every fracture with the modelled length can be computed. Finally, the modelled fractured porosity and permeability values estimated for any cubic cell depend exclusively on the fracture network geometry and the aperture coefficient (*A*).

The initial aperture of a fracture can be modified by numerous water-rock interaction processes, which can have different effects on the initial aperture from part to part along the fracture plane (Vermilye and Scholz, 1995). In addition, the aperture is affected by the prevailing stress field, fracture orientation, depth and roughness of the fracture wall (Kumar et al., 1991; Liu, 2005). Therefore, the current hydraulic fracture aperture is the result of numerous independent processes that make it difficult to estimate. Choosing reliable aperture values, nevertheless, is essential in the evaluation of the hydraulic conductivity behaviour of a fractured rock body.

Given the simulated fracture network geometry and the measured transmissivity data, the hydraulic aperture can be estimated by comparing the observed and modelled permeabilities following the algorithm outlined in Fig. III.4.

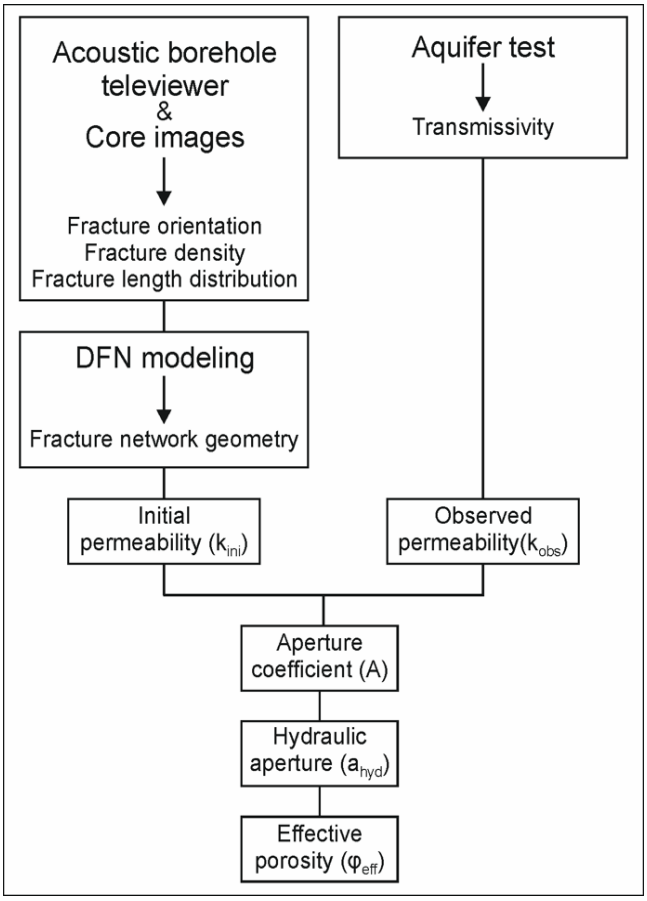

Fig. III.4 Flow chart of the algorithm for determining the hydraulic properties of the BAF–2 well. Aperture coefficient, hydraulic aperture and effective porosity of the well are extracted from the modelled fracture network geometry and the well-hydraulic transmissivity measurement, respectively.

Infress software, as mentioned above, allows the calculation of the porosity (φ_{ini}) and the 3x3 intrinsic permeability tensor for any cubic cell based on the generated fracture network geometry using an aperture coefficient value. As hydraulic measurements of a well do not account for the anisotropy of permeabilities, hereafter, the mean of the diagonal elements of the permeability tensor (k_{ini}) is used during calibration.

Based on the measured transmissivity data, the observed permeability (k_{obs}; Fig. III.4) can be calculated. The transmissivity for the horizontal flow of a rock layer with a specified thickness of d is:

$$T = K * d \tag{III.4}$$

where T is the transmissivity and K is the hydraulic conductivity. The d value in Eq. III.4 is the packer interval used for the transmissivity measurement. From the hydraulic conductivity, permeability is defined as:

$$K = \frac{k\varrho g}{\eta} \tag{III.5}$$

where ϱ and η are the density and the dynamic viscosity of the fluid, respectively, g is the gravitational acceleration, and k is the permeability of the rock body (Grant, 2005). The density and dynamic viscosity of the water were taken as unity in the equation. In this way, the observed permeability (k_{obs}) can be determined for any interval where transmissivity was measured.

In our study, the hydraulic aperture (a_{hyd}) of the fractures was obtained using the above aperture calibration approach (Fig. III.4). The objective of aperture calibration is to change the aperture coefficient value (A) so that the two permeability values (k_{ini} and k_{obs}) for the same volume become equal. To estimate permeability tensor elements with Infress, a rock volume of d^3 was considered. In this way, an average aperture coefficient could be computed for each interval independently, allowing the effective porosity to be calculated for all sections.

The hydrodynamic characteristics of any rock body can be described using the flow zone indicator (FZI). This parameter is based on the covariation of porosity and permeability and is usually used to evaluate reservoir quality. This index can also be applied to define flow units, volumes of reservoirs in which the geological and petrophysical properties that control the fluid flow are internally consistent (Amaefule et al., 1993). According to Al-dhafeeri and Nasr-El-Din (2007), FZI can be calculated as:

$$FZI = \frac{RQI}{NPI} = \frac{0.0314\sqrt{\frac{K}{\Phi}}}{\frac{\Phi}{(1-\Phi)}} \tag{III.6}$$

where *FZI* is the flow zone indicator in μm, *NPI* is the normalised porosity index, *RQI* is the reservoir quality index, *K* is the permeability in mD, and Φ is the porosity in a volume fraction. FZI values are related to the porosity, permeability, capillary pressure, lithology distribution, mineralogy, and sedimentary structures and are also affected by diagenetic processes (Dezfoolian, 2013). Various combinations of these factors may result in distinct rock hydraulic flow units (HFUs). A HFU, by definition, is a volume of a rock body where the geological and petrophysical properties that control the fluid flow are internally consistent (Amaefule et al., 1993). It is worth noting that elevated FZI values do not necessarily mean better hydraulic conductivity; high values indicate only the changing relationship between porosity and permeability. For example, FZI can increase with increasing permeability due to fracturing; if the porosity does not grow to the same extent or if porosity drops without a significant decrease in permeability, FZI may also increase.

III.4. Results

III.4.1. Fracture network parameters

Fracture density can be defined in many different ways. The number of fractures per metre index (P10) was calculated for every 100 m with 50 m overlap based on the BHTV data (Fig. III.5A). This calculation includes all planes detected by BHTV, including faults, veins, joints and bedding planes. The upper part of the well, between 100 and 420 m, is highly fractured; the average fracture density is 9–10 m^{-1}. Below 420 m, three fractured zones can be distinguished at ~500, ~650, and ~850 m (5–6 m^{-1}). The fracture density between these zones is low; 3–4 fractures per metre can be found in the least fractured sections (Fig. III.5A).

The fractal dimension (*D*) was calculated for 100 m long sections of the well with 50 m overlap. The average *D* is 1.37±0.05, while high *D* values characterise three well-defined zones, 140–250, 580–680 and 790–870 m, with elevated fracture densities (Fig. III.5B). A single length exponent (E) and an F parameter were calculated for the entire well using the approach detailed by M. Tóth (2010): E = –0.90 and F = 10.00.

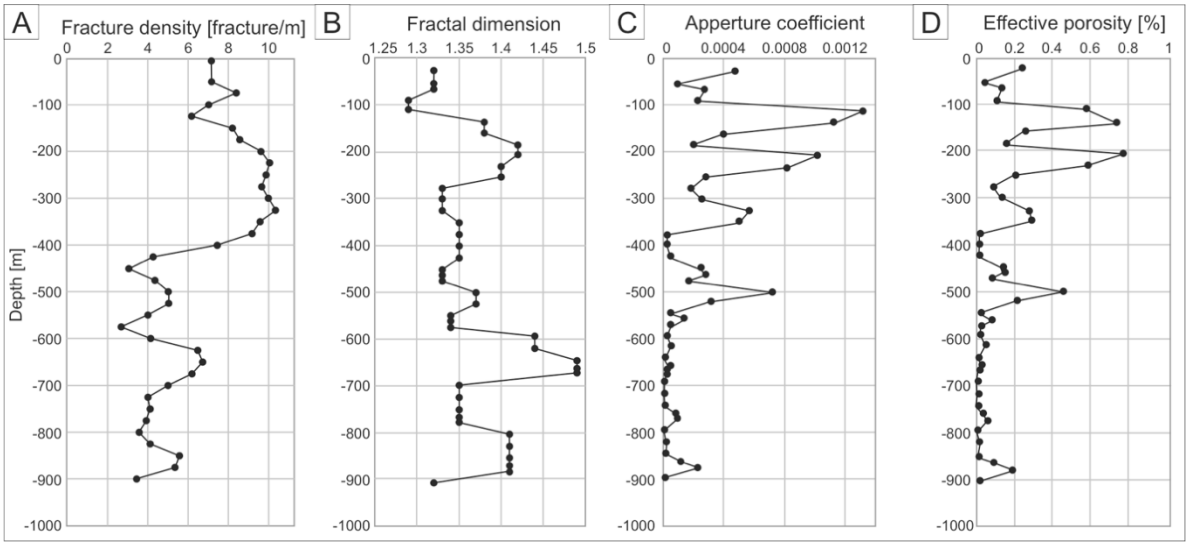

Fig. III.5 (A) Fracture density log of the well expressed with the number of fractures per meter (P10 parameter); (B) Fractal dimension log of the well, determined in every 100 m, with 50 m overlap; (C) Variation in aperture coefficient along with the well; (D) Effective porosity log of the well.

Based on the BHTV evaluations, most planes detected in the borehole have an SSE dip direction (Fig. III.6) with an average orientation of ~ N162° E60°. The planes in this group primarily indicate sedimentary bedding and probably fracture planes parallel to layering (Fig. III.6).

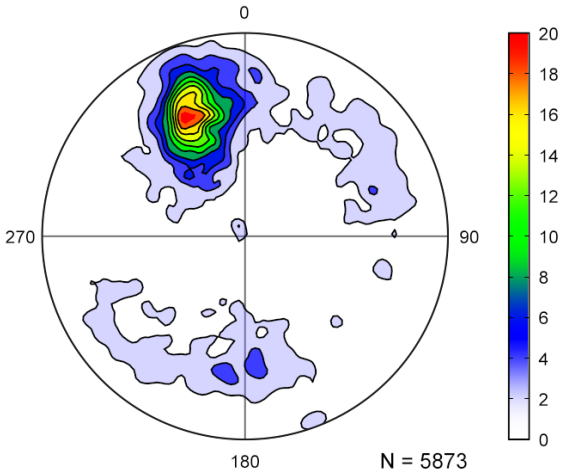

Fig. III.6 Lower hemisphere stereographic projection of the poles of the bedding and fracture planes based on BHTV data on Schmidt net. The isolines denote 2% increase in frequency. The largest group of planes has a SSE dip direction, which coincides with the dip direction of the bedding planes.

III.4.2. Fracture network modelling

Modelling was carried out in a 150 x 150 x 925 m cuboid surrounding the well. The presence of connected subsystems can characterise the simulated fracture networks in each run. Based on 20 independent runs, five typical geometries were distinguished regarding the communication of the fracture network (Fig. III.7).

In the first case, the whole fracture system defines one communicating group (Fig. III.7A). In many cases, two connected subsystems are present that do not interconnect with each other. The boundaries between the subgroups vary from one run to another and appear at ~300, ~400 or ~700 m (Fig. III.7B, C, D). In some cases, the fracture system of the well splits into four connected fracture subgroups along the boundaries at ~100, ~400, and ~700 m (Fig. III.7E).

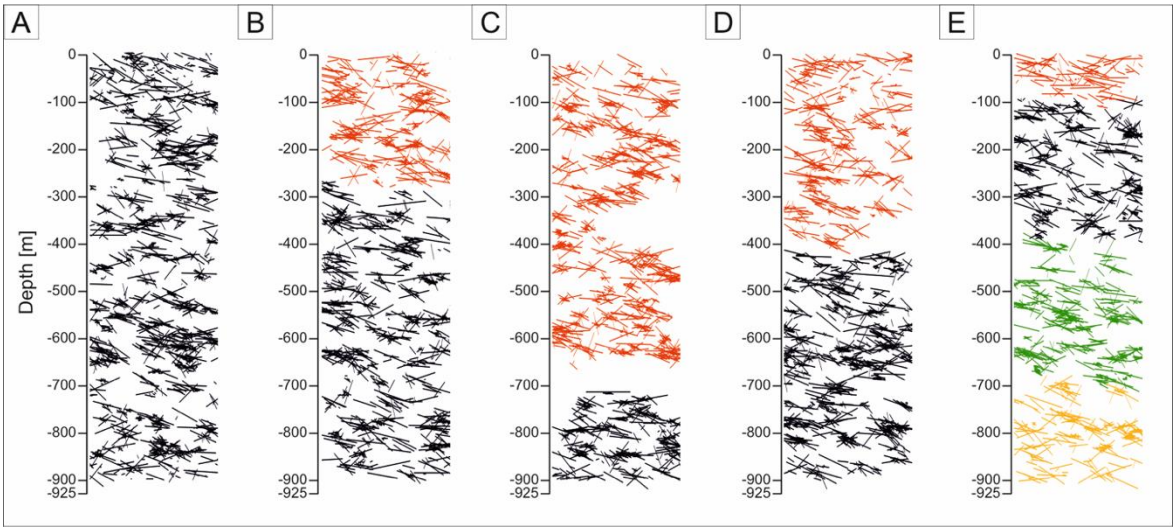

Fig. III.7 Vertical east-west sections of typical simulated fracture network geometry patterns (A–E) of the BAF–2 well based on 20 independent runs. Different colours indicate the communicating fracture groups within the well. The width of the sections is 150 m.

III.4.3. Estimation of the aperture coefficient and effective fractured porosity

The values of the calibrated aperture coefficient (A in Eq. III.3) of the 20 m long intervals, from which the transmissivity data were obtained, decrease with depth and vary between 4×10^{-6} and 8×10^{-4} (Fig. III.5C). The hydraulic aperture of a fracture with a diameter of 1 m may change between 4 μm and 0.8 mm, depending on the influence of the post-tectonic fluid-rock interaction processes, the degree of closure with depth and the current stress field. The aperture coefficient of the fracture system in the lower half of the well is significantly reduced in two sections (380–420 m and 580–850 m), while the upper section (120–160, 200–240 and 320–340 m) is characterised by elevated values.

The effective porosity log (Fig. III.5D) follows the anomalies seen on the aperture coefficient log (Fig. III.5C). Sections with a high effective porosity are characteristic in the upper part of the well (above 400 m). There are two sections with significantly higher porosity values in the lower part at ~500 m and ~850 m, while a small increase can be detected at ~780 m (Fig. III.5D).

III.4.4. Poro-perm diagram and the flow zone indicator

The examination of the porosity and permeability data together allows the characterisation of the reservoir bodies from a hydrodynamic point of view. Therefore, the conventional poro-perm diagram was constructed, and FZI values were calculated for all 44 data points along the well. The permeability data were derived from hydraulic measurements of the well, while the porosity data were estimated based on the DFN model and the calibrated aperture coefficients. The largest section of the well follows the same trend on the poro-perm diagram with an excellent fit (R^2 = 0.986; Fig. III.8A, black curve). In this section the typical value of the FZI is between 200–350 (Fig. III.8C/b, d, f).

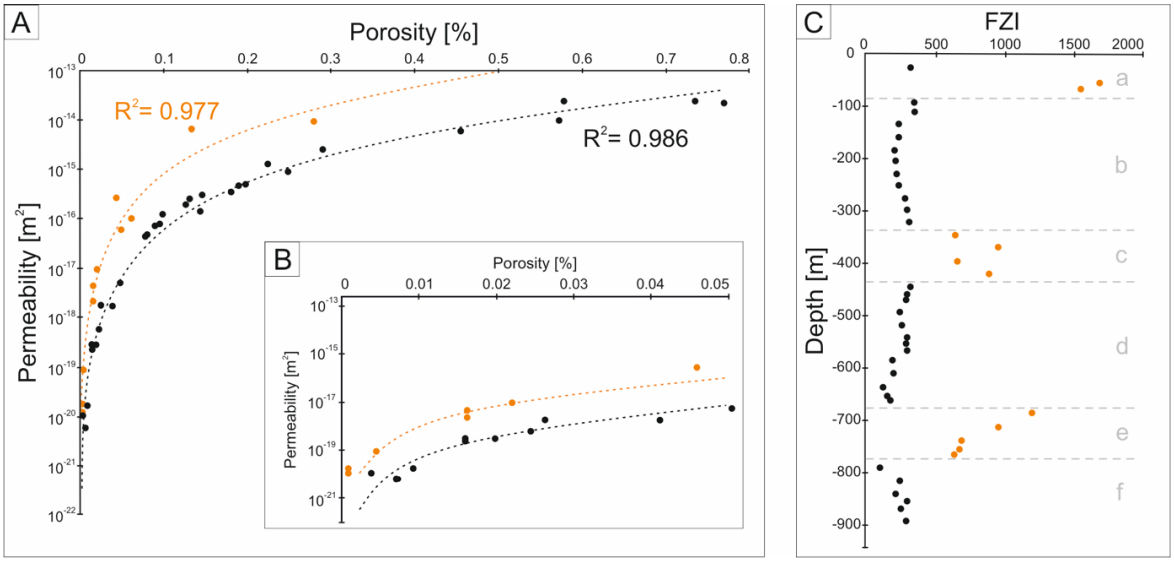

Fig. III.8 (A) Poro-perm trends of the BAF–2 well based on the measured permeability and computed effective porosity data. (B) Inset of the poro-perm trend diagram of small values. (C) The hydraulic flow units of the BAF–2 well are indicated by the flow zone indicator (FZI), dashed lines designate the borders of the HFU-s, grey letters (a-f) indicate the HFU-s. Different colours indicate different FZI trends.

There are three narrow, distinct zones with elevated FZI values (60–110 m, 350–420 m, and 690–770 m; Fig. III.8C/a, c, e). The data points for all of these sections lie on the same trend on the poro-perm diagram (R^2 = 0.977; Fig. III.8A, orange curve). Using the poro-perm

trends and the FZI values, the studied well can be subdivided into six hydraulic flow units (Fig. III.8B, C).

III.5. Discussion

III.5.1. Evaluation of the structural elements of the well

This study examines the fracture network of a potential high-level radioactive waste repository site in Hungary using fracture network modelling. The modelling parameters were determined primarily using BHTV data and core images of the BAF–2 well. A BHTV records fracture planes and bedding similarly along the borehole; both appear as sinusoidal curves in the images. Although several steep fractures crosscut the studied formation, many others lie parallel to the bedding surfaces (Konrád et al., 2015). This geometry suggests that due to competence contrast these planes were most effectively deformed during tectonic or atectonic events. Consequently, fractures and stratifications are difficult to distinguish using BHTV images in the lithologically homogeneous sections of the rock body. On the other hand, fractures and bedding planes may play an identical hydrodynamic role, as they all may act as migration pathways for water and radionuclides. Therefore, for modelling purposes, we took into account every discontinuity within the rock body detected by the BHTV. Therefore, the results of the fracture network modelling approach outline the worst-case scenario regarding the hydraulic features and fracture connectivity of the studied rock body, which is a potential host rock for the repository of high-level radioactive waste.

III.5.2. Fracture density of the well

Two numerical indices were used to characterise the fracture intensity of the formation: the number of fractures within a metre (P10 index) and the fractal dimension. Based on both indicators, the well can be subdivided into two major sections with a boundary at approximately 400 m. The fracture density (P10 log) characteristics differ significantly between the lower and upper sections of the well; a well-defined, sharp boundary horizon can be drawn between them. Several factors can affect the fracture density of a rock body, among which the rock type, grain size, prevailing stress field and tectonic events are the most essential. In the BAF–2 well, the average grain size of the sediment continuously increases downwards without any abrupt jump at 400 m, and no significant change in lithology can be detected at this depth. Any discontinuous change along this boundary in either the thickness or the lithology of the beds could influence the fracture pattern. Furthermore, both the average grain size and the diagenetic history of the various rock types might result in different rheological properties, causing diverse rock bodies

to respond differently to the same stress field (Brace and Riley, 1972; Paterson, 1978). Even a slight change in the petrophysical features of the rock could influence the fracture density (National Research Council, 1996). Therefore, it cannot be excluded that the change in the fracture pattern at 400 m is caused by the increasing average grain size and thus the difference in the rheological parameters of the formation.

On the other hand, based on stratigraphic irregularities, such as overturned beds and changes in graded sequences, some authors have suggested the presence of a structural boundary in the well (Konrád et al., 2015). This assumption is also supported by the acoustic wave velocity log, which shows an abrupt change in the rock body at 400 m (Bernáth et al., 2014).

In the lower part of the borehole, sandstone layers are more common towards the bedrock below 757 m, where the first sandstone layer with a significant width appears. Here, the density of fractures (P10 index) decreases simultaneously with the presence of sandstone layers (Fig. III.5A), further strengthening the correlation between the fracture geometry and the grain size of the host rock.

Alternatively, instead of changing of the rock type, the three highly fractured zones in the lower half of the well may indicate three distinct shear zones determined by the prevailing stress field. In this model, poorly deformed horizons separate the shear zones at 580 and 710 m.

III.5.3. Hydrological evaluation of the fracture network

The aperture coefficient, which is the aperture of a fracture of unit size, significantly influences the hydrological behaviour of fractured rock bodies. Its value continuously decreases downwards with intervals of anomalous behaviour. The coincident scattering of the hydrological aperture may be the consequence of diverse water-rock interaction processes such as dissolution and cementation. The reduction in the aperture coefficient along the borehole coincides with more closed, presumably more cemented, fractures. In contrast, larger aperture coefficient values indicate open fractures, which could form as a result of weak cementation, dissolution or in situ stresses (Lowell et al., 1993; Laubach et al., 2004; Barton, 2014; Bisdom et al. 2016; Deng et al., 2018).

The two major sections (upper part: 0–400 m; lower part: 400–915 m) of the well determined by the fracture density are also traceable along with the aperture coefficient and effective porosity logs. The aperture coefficients of the fractures vary significantly in the upper section, where well-cemented and poorly cemented sections probably alternate (Tokan-Lawal et al., 2017). The effective porosity varies depending on the change in the aperture coefficient;

where the fractures are more open, the effective porosity increases. In the lower section, the aperture of the fractures decreases significantly. Two of the fracture zones in the lower part at 500 and 850 m have slightly increased aperture coefficients and effective porosity values. The fractures in these zones are probably less cemented. Deeper segments of the borehole generally have smaller aperture coefficients and effective porosity values. The highly fractured zone at 650 m determined by the P10 parameter (Fig. III.5A) cannot be detected on either the aperture coefficient log or the effective porosity log. Based on this observation, this fracture zone probably contains well-cemented fractures that are less hydraulically active. Furthermore, this zone exemplifies that a dense fracture network does not automatically coincide with a hydraulically active system.

The hydraulic behaviour of the well can also be characterised by FZI, which concludes the relationship between porosity and permeability. Two different trends can be recognised along the well based on the poro-perm diagram. A significant part of the rock body aligns to a single trend, suggesting that the predominantly homogenous lithology of the BAF–2 well also has homogeneous hydrodynamic features.

There are three 60–100 m wide sections, where the data determine a different trend on the poro-perm plot and the coinciding FZI values also differ. All of these sections form independent hydraulic flow units along the well. Such deviations may be caused by changes in lithological or structural features.

III.5.3.1. Weathered HFU

The first hydraulic unit of the BAF–2 well with elevated FZI values appears between 60 and 110 m (Fig. III.8C/a). In this section, the porosity decreases more considerably than the permeability, causing an increase in FZI. A possible explanation for this behaviour is that a significant amount of limonite is present in the upper 100 m of the well that formed due to weathering of the haematite-bearing host rock by meteoric waters in the upper part of the rock body (Konrád et al., 2015). As the limonite density is approximately 2.7–4.3 g/cm^3 and that of haematite is 5.3 g/cm^3, hydration of the original rock-forming mineral phase is accompanied by a significant volume increase in the host rock. The volume increases from 30.28 to 41.64 cm^3 for each mole of haematite, which should cause a considerable reduction in the matrix porosity. The permeability, which is mainly connected to structural elements, such as fractures and bedding planes, is less reduced due to the same hydration process. Hence, limonite formation greatly influenced the hydraulic behaviour of the rock body, allowing the development of a flow unit with increased FZI values in the uppermost zone of the well.

III.5.3.2. Sheared HFU

The second hydraulic flow unit, which differs from the primary FZI trend, occurs between 350 and 420 m (Fig. III.8C/c). Along this section, the porosity is very low (Fig. III.5D), but the permeability does not decrease to the same extent, resulting in elevated FZI values (Fig. III.8C/c). At approximately 400 m, this depth interval appears as a boundary in several features along the well. Here, a significant drop in the fracture density is apparent (Fig. III.5A), which alone should cause simultaneous decreases in porosity and permeability, but this would not change the FZI trend.

Nevertheless, the above calculations confirm that the aperture coefficient is substantially reduced in this depth interval. The anomalously low aperture coefficient values suggest that the fractures are more intensely closed than is typical in the well. Furthermore, a sharp decrease in the acoustic wave velocity is also observed below 400 m. This feature reflects the appearance of a rock body with significantly different rock mechanical properties, even if the lithology and the fracture geometry parameters (other than the density) do not change at this boundary. Furthermore, the presence of all four vein generations (Hrabovszki et al., 2017, 2020, 2022; Tóth et al., 2020) along the well suggests that the entire rock column shares an identical structural evolutionary history.

Konrád et al. (2015) explained that the difference between the upper (0–400 m) and lower (400–915 m) segments of the rock body developed during uplift of the formation and the coincident loosening of the upper section. Nevertheless, exhumation would result in a continuous transition in the fracture density and would not justify the observed pattern. The well-defined boundary may instead indicate lithological or structural changes. Based on sedimentological observations (changes in the style of graded bedding, overturned strata sections, etc.), a large-scale shear zone was previously assumed to be present around the same interval (Konrád et al., 2015), without the possibility of precisely locating it. Such a large-scale fault zone is difficult to detect using exclusively small-scale observations. Fault evolution in hard claystones starts with cataclasis, where clay gouges could fill the space between the initial fractures. As faulting progresses, a fully reworked clay gouge could form, which is often not accompanied by mineralogical changes. These evolutionary stages coexist in a fault zone (Holland et al., 2006). The separation of the lithotypes of a fault zone in the highly fractured BCF is difficult, but the changes in porosity and transport properties could strongly indicate a fault zone (Holland et al., 2006).

The FZI log also draws this broad interval as an independent hydraulic flow unit. Above this HFU (350–420 m), the FZI values continuously deviate from the primary trend. Below this

zone, FZI values continuously decrease forming a more than 100 m wide disturbed zone (Fig. III.8C). Taking all observations into account, the entire flow unit with elevated FZI values can indicate the core and the damage zones of a large-scale fault zone. The low fracture density and low porosity in the core zone may be derived from the self-sealing properties of the claystone (Holland et al., 2006; Zhang, 2013; Rutqvist et al., 2020). The very low aperture coefficient values in the core zone also confirm this phenomenon. We propose a large-scale structural boundary at 400 m crosscut by the BAF–2 well. Considering all the above findings, a shear zone more than 100 m wide can be supposed at this interval in the rock body.

III.5.3.3. Coarse-grained HFU

The third section in the borehole with elevated FZI values appears between 690 and 770 m (Fig. III.8C/e). At the boundary of the zone, FZI values change abruptly; unlike to the anomalous zones mentioned above, there is no continuous transition between the major trend and this HFU.

In this zone, the fracture density is not too high, but both the aperture coefficient and the porosity values are slightly elevated. Since sandstone layers become more frequent at this interval, the changes in the hydraulic properties of this section may be due to lithological reasons.

On the other hand, in this HFU the sonic log disturbance is similar to the behaviour observed at approximately 400 m (Fig. III.2B). The acoustic wave velocity decreases significantly, especially between 680 and 690 m. The similarity of this pattern to the structural boundary at 400 m implies that another structural boundary is located at this depth. In this case, the core of the fault zone may be indicated by the lowest velocity of the acoustic waves between 680–690 m, and the highly fractured section may represent the damage zone (Holland et al., 2006).

At both margins of this HFU FZI are lowest within the whole rock column (FZI > 200). Between 640–670 m (Fig. III.8C), fracture density increases; one of the three fracture zones of the lower part of the well appears in this depth interval. This section could form a flow unit if we draw the lower limit of the main trend at 200 FZI values, but the poro-perm trend of these data points is very similar to the main trend. Therefore, it is just a matter of interpretation whether it is an independent unit or not. The lithology does not change significantly here, and the mineral compositions of the four vein generations are unchanged (Hrabovszki et al., 2017, 2020, 2022; Tóth et al., 2020). Therefore, this section could not have formed due to its unique lithology or a different history of vein formation. Nevertheless, this section contains well-cemented fractures, as indicated by the aperture coefficients and effective porosity logs

mentioned above (Fig. III.5C, III.5D). The high fracture density in this section could enhance fluid flow, leading to a high degree of cementation (Lee et al., 1996). This process should result in decreasing permeability and low FZI values. As a result, this depth interval has the worst hydraulic properties of the entire well, despite being one of the highly fractured zones of the well.

This hydraulic unit could have formed due to the complex effects of several processes. Among them, the increasing number of coarse-grained beds and the impact of a possible structural boundary are the most emphasised.

III.5.4. Near-well fracture network geometry

The geometry of the fracture system corroborates the designated hydraulic units within the well. In some cases, the whole modelled fracture system defines one connected system. Therefore, the fracture geometry properties allow a more than 1000 m wide, hydraulically communicating fracture system (Fig. III.7A).

In numerous fracture network models, connected fracture subgroups form and are usually separated at the well-defined depths mentioned above. These designated boundaries appear at approximately 100, 400 and 700 m. At these particular depths, the fracture system should be close to its percolation threshold; therefore, the fracture network connectivity cannot be predicted (Berkowitz, 1995; M. Tóth and Vass, 2011). Even small changes in the modelling parameters can significantly influence the connectivity between the subsystems. Even using the same parameter set may result in different fracture patterns in terms of connectivity (M. Tóth and Vass, 2011).

Taking the modelled fracture geometries together with the information from the hydraulic flow units, the rock body of the BAF–2 well can be divided into four blocks (Fig. III.7E) with boundaries at approximately 100, 400 and 700 m. Around these boundaries, the rock body has specific hydraulic and rheological properties; otherwise, it behaves homogeneously from both physical aspects. Furthermore, all the blocks are affected by the main vein-forming events that developed the four vein generations of the well.

III.6. Conclusions

In this study, we examined the hydrological consequences of the fracture system of a claystone formation. A fundamental attribute of a fracture network is its spatial density, based on which the studied rock column can be divided into two major parts. The upper part of the BAF–2 well, between 0 and 400 m, is highly fractured, while the lower section, below 400 m, contains significantly fewer fractures on average. The lithology of the well is mostly

homogenous; nevertheless, coarser-grained beds become more frequent with depth. The positions of the intensely fractured zones are primarily determined by tectonic processes, but the changing grain size could also influence the fracture density.

The hydraulic properties of the fracture system were investigated using measured permeabilities and computed effective porosities. For this calculation, aperture coefficients were estimated using DFN models for each depth interval where transmissivity measurements were available. The data evaluation suggests that two different poro-perm trends define the hydraulic behaviour of the rock body crosscut by the studied well. While most intervals conform to one trend, three sections differ from it and define distinct hydraulic flow units based on the FZI values.

The communicating fracture clusters and the hydraulic flow units designate the same horizons in the well. Considering the hydraulic characteristics and the fracture geometry, the rock body of the BAF–2 well could be divided into four blocks separated by boundaries at ~100, ~400 and ~700 m. The formation of the boundary at ~100 m relates to lithological and diagenetic processes. Another boundary at ~400 m probably represents the core zone of a wide shear zone. In comparison, the horizon at ~700 m could result from the combined effects of lithology and tectonic activity.

This study outlines the fracture network geometry and the hydraulic features of the BAF–2 well, which may provide a solid basis for further hydrodynamic modelling of the well and its surroundings.

CHAPTER IV.

USING GEOPHYSICAL LOG DATA TO PREDICT THE FRACTURE DENSITY IN A CLAYSTONE HOST ROCK FOR STORING HIGH-LEVEL NUCLEAR WASTE

Emese Tóth

Department of Mineralogy, Geochemistry and Petrology, University of Szeged, Hungary

tothemese@geo.u-szeged.hu

Ervin Hrabovszki

Department of Mineralogy, Geochemistry and Petrology, University of Szeged, Hungary

hrabovszkiervin@geo.u-szeged.hu

Tivadar M. Tóth

Department of Mineralogy, Geochemistry and Petrology, University of Szeged, Hungary

mtoth@geo.u-szeged.hu

Acta Geodaetica et Geophysica

Accepted Manuscript

In Press

Using geophysical log data to predict the fracture density in a claystone host rock for storing high-level nuclear waste

Emese Tóth, Hrabovszki Ervin, Tivadar M. Tóth

Abstract

Previously drilled boreholes of a host rock for a potential nuclear waste repository in Hungary revealed a highly fractured claystone rock body. A crucial step for characterizing the hydrodynamic behaviour of such a fractured reservoir is fracture identification and accurate calculation of the fracture density. Although acoustic borehole televiewers provide a reliable base for determining the fracture density, older boreholes usually lack such data. However, conventional borehole geophysical measurements are often accessible in such cases. The aim of this study was to identify any correlations between well log data and the fracture density. Multiple linear regression analysis was performed on data from two boreholes penetrating the Boda Claystone Formation in southwest Hungary. The upper section of the BAF–4 borehole was used for training, where the fracture density was estimated with a fit of $R^2 = 0.767$. The computed regression function predicted the fracture density with high accuracy in both boreholes for all intervals with typical lithological features. However, in some sections where anomalous well log data indicated changes in the lithology, the prediction accuracy decreased. For example, the function underestimated the fracture density in sandy intervals.

IV.1. Introduction

A host rock of a waste repository that contains fractures may be considered a fractured reservoir. The viability of a fractured reservoir as a waste repository depends on how fluid and contaminants can be retained in the formation. Claystone formations are often targeted as potential repository sites, along with salt, tuff, and granitic rock formations (Ahn and Apted 2010). Claystone generally has very low matrix porosity and permeability, which allows fluid to move exclusively along fracture planes (Anders et al. 2014). Therefore, the fracture network geometry, fracture aperture, and fracture density are among the key parameters that affect the fluid flow in fractured reservoirs. The detection of fractures and precise estimation of the fracture density are important for characterizing the hydrodynamic behaviour of a fractured reservoir. Such information can reflect fracture development and connectivity, which are useful for optimizing waste disposal (Nelson 2001; Ge et al. 2020).

Fractures in boreholes can be detected both directly and indirectly. Direct methods include core analysis, impression packers, and borehole cameras. Indirect methods include packer borehole tests and well log data (Ja'fari et al. 2012). The most accurate method is through direct observation and core analysis, but this approach is costly and time-consuming, and cores are frequently unavailable. In addition, highly fractured zones are often lost during core recovery, and mechanical fractures are frequently induced, which significantly alters the fracture density of multiple sections (Laubach et al. 1988). Human error and non-constant resolution limits may also affect the observed fracture density in direct observation of cores. Downhole cameras are small devices that can capture images and video inside a borehole. These tools collect high-resolution data and offer a quick and efficient approach to detecting discontinuities. Unfortunately, image logs are not available for hundreds of boreholes drilled before such technology was introduced in the 1980s (Tokhmchi et al. 2010; Ja'fari et al. 2012). One of the most popular methods for localizing fractures along boreholes is the acoustic borehole televiewer (BHTV), which is rapid, cost-effective, and accurate (MartinezTorres 2002). A BHTV provides a continuous and oriented image of the borehole wall which reflects the orientation, dip angle and thickness of fractures as a function of depth. BHTV logs are beneficial for evaluating boreholes without oriented cores (Massiot et al. 2017). Images are produced based on the travel time of the ultrasonic signal reflected from the borehole wall in this technique (Zemanek et al. 1970, Pöppelreiter et al. 2010). Potential fluid routes may develop along any discontinuity in a formation. Thus, every single discontinuity is worth defining as a fracture when evaluating a fracture network.

Discrete fracture network (DFN) modelling is a valuable technique for determining the fracture network geometry in a fractured reservoir if the geometric characteristics of individual fractures are known (Witherspoon et al. 1980; Neuzil and Tracy 1981). By modelling the fracture networks of numerous boreholes, it becomes possible to analyse the hydrogeological behaviour over a wider area and the impact of various processes on the fracture network characteristics. One of the most critical parameters for correlating boreholes is the fracture density. Although BHTV datasets provide a firm basis for computing fracture density logs, this information is frequently unavailable for older boreholes. In such cases, however, standard geophysical well logs are typically available. Incorporating such old boreholes in spatial correlation studies can help improve understanding of fractured rock bodies, the locations and sizes of communicating fracture clusters, and the positions of significant structural boundaries.

The fracture density is a significant characteristic that is the primary basis for correlating data from boreholes in the Boda Claystone Formation (BCF). P10 is the most widely used parameter for quantifying the fracture density, and it is defined as the number of fractures per

meter, which can be derived from BHTV data for any borehole segment. Downhole geophysical logging can be used to examine the petrophysical characteristics of a rock formation. Logging equipment responds to various features in the borehole environment (Shalaby and 98 Islam 2017). Even for older boreholes, conventional well logs frequently include geophysical data such as natural gamma rays, spontaneous potential, sonic transit time, bulk density, neutron porosity, calliper data, and resistivity. In contrast, unconventional well logs such as the Formation MicroScanner (FMS) and Formation MicroImager (FMI) are too specialized, expensive, or recently invented to be utilized in every borehole (Gamal et al. 2022).

Several earlier studies have attempted to estimate the fracture density by using conventional well logs. Most of these studies were related to hydrocarbon production, so they typically targeted formations such as fractured carbonate and sandstone reservoirs. Tokhmchi et al. (2010) used well log data (calliper data, density, neutron porosity, sonic transit time, resistivity, natural gamma rays) to calculate the fracture density in naturally fractured reservoirs. Ja'fari et al. (2012) used an adaptive neuro-fuzzy inference method on well log data (sonic transit time, deep resistivity, neutron porosity, bulk density) to calculate the fracture density. Zazoun (2013) used artificial neural networks (ANNs) on standard well log data (gamma rays, sonic transit time, calliper data, neutron porosity, bulk density) as well as core data to predict the fracture density. Aghli et al. (2016) used well log data (bulk density, neutron porosity, gamma rays, sonic transit time, photoelectric absorption, calliper data) to determine fracture zones in a fractured carbonate host rock. Taherdangkoo and Abdideh (2016) used the wavelet transformation approach on conventional well log data (gamma rays, bulk density, sonic transit time, photoelectric absorption) to estimate the locations of fractured zones and calculate the number of fractures in each zone of a reservoir. Dong et al. (2020) used a semi-supervised learning system on conventional well log data (gamma rays, calliper data, spontaneous potential, neutron porosity, acoustic impedance, density, resistivity) to predict fracture zones in tight sandstone. Owing to a lack of directly obtained advanced logging data, Gamal et al. (2022) integrated conventional well logs, thin sections, and other available data to detect fractures in a carbonate rock body. However, no previous study has attempted to use well log data to estimate the fracture density in a claystone formation.

The aim of this study was to quantify how different geophysical features describe the fracture density so that the fracture density of boreholes can be determined without BHTV data. The relationship between geophysical characteristics recorded in well logs and the fracture density of a claystone formation was explored by multiple linear regression analysis, and the developed approach was tested on two boreholes of the Boda Claystone Formation, which is a potential site for a high-level nuclear waste depository in Hungary.

IV.2. Methods

Multiple linear regression (MLR) analysis is a statistical technique to model the linear relationship between a dependent variable and a set of independent variables. The dependent variable is referred to as the predictand or response, while the independent variables are referred to as predictors. MLR model establishes a simultaneous statistical relationship between the single continuous outcome *y* and the predictor variables x_k (k = 1, 2, ... , p − 1):

$$y_i = \beta_0 + \beta_1 x_{i1} + \beta_2 x_{i2} + \ldots + \beta_{p-1} x_{i,p-1} + \varepsilon_i \qquad \text{(IV.1)}$$

where β_0 represents the intercept, also called the constant (the mean of *Y* when all $X_k = 0$), and each β_k represents a slope with respect to X_k, ε_i is the *ith* error. The β_k are called partial regression coefficients (Eberly, 2007; Olive, 2017; Tranmer et al. 2020).

The multiple regression analysis procedure consists of the following steps (Tranmer et al. 2020). In order to build a multiple linear regression model, additional assumptions must be verified. It is important to confirm that a linear relationship is likely to exist for each predictor. If the relationship is not linear, a transformation of the variables is required. The normality assumption assumes that the residuals have a normal distribution with a mean of zero.

The predictors should be independent of each other. High correlations between two or more independent variables are a sign of multicollinearity, which creates redundant information that distorts the results of a regression model. The model can be simplified by removing the highly correlated variables. The variance inflation factor (VIF) can show how multicollinearity has increased the variance of the regression estimates. Multicollinearity can be a problem if the VIF is higher than 10 (Alin, 2010):

$$VIF_i = \frac{1}{1 - R_i^2} \qquad \text{(IV.2)}$$

Where VIF_i is the variance inflation factor of the *i*th predictor and R^2_i is the multiple coefficient of determination in a regression of the *i*th predictor on all other predictors (Alin, 2010).

The Durbin-Watson (DW) statistic tests for autocorrelation in the residuals of the regression analysis and determines whether there is a significant correlation based on the order in which they appear in the data file:

$$d = \frac{\sum_{i=1}^{n} (e_i - e_{i-1})^2}{\sum_{i=1}^{n} e_i^2} \qquad \text{(IV.3)}$$

where n is the number of observations, $\varepsilon_i = y_i - \bar{y}_i$ (y_i is observed values, $\bar{y}_i$ is the predicted values). DW value is always between 0 and 4, if there is no autocorrelation the DW value should be between 1.5 and 2.5 (Vinod, 1973).

Second comes the estimation of the linear regression model and the diagnostic evaluation. The model should then be reduced by removing non-significant predictors after making inferences about the regression coefficient. Finally, recheck that the model provides an adequate fit to the data.

This study used multiple regression analysis with the backward elimination method. Backward stepwise regression is a stepwise regression method that starts with a full model and gradually removes variables to obtain a reduced model that best fits the data. The process of backward elimination ends once all remaining variables meet the requirements to remain in the model (Olive, 2017). The dependent variable was the fracture density measured as P10. The set of independent variables was the geophysical well log data.

Different goodness-of-fit measures can be used for linear regression models. The R^2 value ranges from 0 to 1 and provides a relative measure of the portion of the variation in the dependent variable that is explained by the model (Bowerman et al., 2005). The standard error of estimate (S_e) measures how far away data points typically are from the regression line. Mean absolute error (MAE) indicates the average value of residuals.

IV.3. Geological setting

Several 1000-m-deep boreholes with nearly 100% core recovery were previously drilled in the BCF to investigate its potential as a final storage location for high-level radioactive waste in Hungary (Konrád and Hámos 2006). These boreholes offer a rare opportunity to study and model the fracture network of a claystone formation as precisely as possible. The BCF may be appropriate for storing nuclear waste in Hungary because of its thickness, low permeability and porosity. The BCF is 900 m thick and is a member of the 4000–5000 m thick Palaeozoic–Triassic sedimentary sequence of the Western Mecsek Mountains in southwest Hungary (Fig. IV.1). This Late Permian formation primarily comprises well-compacted reddish-brown claystone and siltstone with layers of fine sandstone and dolomite. The rock-forming minerals are quartz, albite, illite-muscovite, chlorite, calcite, dolomite, and hematite (Árkai et al. 2000). The BCF was deposited in a playa mudflat in an alkaline lake environment during the Late Permian (Árkai et al. 2000; Varga et al. 2005, 2006; Varga 2009; Konrád et al. 2010).

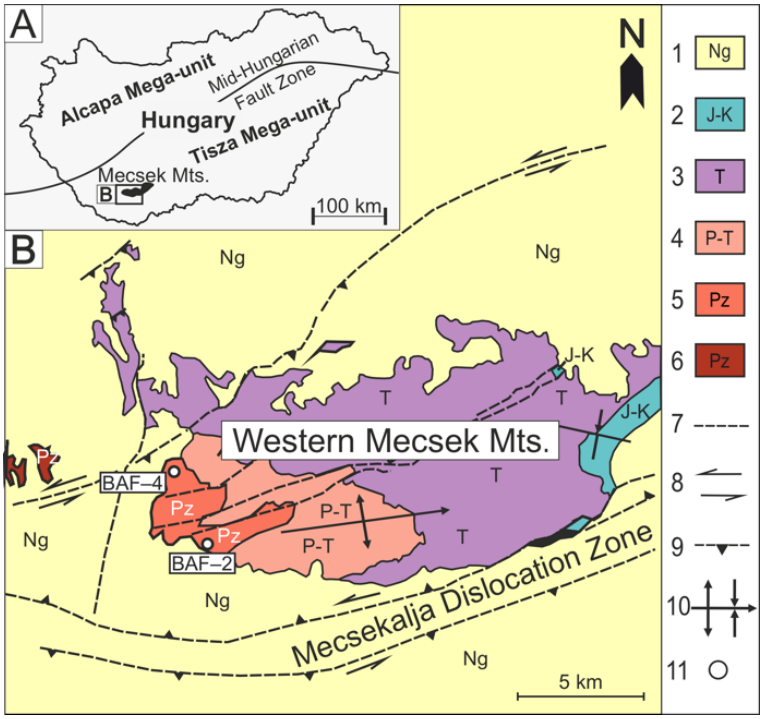

Fig. IV.1 (A) Location of the Mecsek Mountains in Hungary. (B) geological map of the Mecsek Mountains showing the distribution of the Boda Claystone Formation (BCF) modified after Konrád and Sebe (2010). Legend: (1) Neogene sediments, (2) Jurassic and Cretaceous sediments and Cretaceous volcanic rocks, (3) Triassic sediments (sandstones, carbonates, and evaporites), (4) Upper Permian–Triassic Kővágószőlős Sandstone Formation, (5) Upper Permian BCF, (6) Palaeozoic, (7) fault, (8) strike-slip fault, (9) thrust fault, (10) syncline and anticline, (11) borehole sites

Several successive tectonic stages characterize the structural evolution of the region. Significant NE–SW shortening occurred in the Late Cretaceous (Benkovics et al. 1997) followed by Neogene events related to the formation of the Pannonian Basin. Early Miocene deformation caused by tensional forces was followed by Late Miocene (Sarmatian) compression and thermal subsidence of the basin (Bergerat and Csontos 1988; Csontos and Bergerat 1992; Fodor et al. 1999; Csontos et al. 2002; Maros et al. 2004). The ongoing tectonic inversion of the basin is the most recent significant event (Konrád and Sebe 2010). Previous drillings have revealed a rock body with a significant number of mineral veins and fractures. Examining these structural elements is crucial for evaluating the retention qualities of the claystone. BAF–2 is a borehole that has been extensively investigated, and numerous studies have focused on its veins and fractures (Hrabovszki et al. 2017, 2020, 2022; Tóth et al. 2020, 2022a, 2022b). Four distinct vein generations have been identified: straight veins, veins with wall rock inclusions, breccia-like veins, and sigmoidal shaped en-échelon veins. These are

primarily filled by calcite while small amounts of anhydrite, barite, celestine, etc. are also present as vein-filling phases (Hrabovszki et al. 2020, 2022).

DFN modelling and hydrogeological evaluation of the simulated fracture network of BAF–2 revealed three zones whose hydrogeological properties deviate from the average of the claystone body (Tóth et al. 2022a). BAF–2 is more than 900 m deep (Fig. IV.2), and the first anomalous zone is located in the upper 100 m, where the porosity decreases more considerably than the permeability. This may be because the BCF was exposed at the surface for a considerable amount of time (Konrád et al. 2015), and the subsequent weathering changed the hydrogeological characteristics in the uppermost part. Several features of the upper 400-m and bottom 400-m sections of BAF–2 differ considerably. The upper half of BAF–2 has a significantly higher P10 than the lower half, and the geophysical logs also differ (Tóth et al. 2022a). The average P10 is 8.7 m^{-1} in the upper 400 m and 4.6 m^{-1} in the lower 400 m (Fig. IV.3). Considering the tectonic history of the area, the contact between the two regimes can be interpreted as a large-scale structural boundary that is probably a reverse fault zone. The border of the two sections also behaves as an independent hydraulic unit. The third zone, which differs from the average hydrogeological characteristics, is at a depth of about 700 m, and it displays unique behaviour attributed to fine sandstone layers that are common at depths below 758 m or another large-scale tectonic structure could also influence the hydrogeological behaviour of this section (Tóth et al. 2022a).

IV.3.1. Fracture system of the BAF–4 well

BAF–4 is a 900-m-deep borehole that was also considered in the present study. Below the BCF, BAF–4 unexpectedly ran into the Gyűrűfű Formation and drilled into it for about 50 m (Fig. IV.2). The same method presented by Tóth el al. (2022a) was used to characterize the fracture network of BAF–4. The P10 values of the two boreholes, which are approximately 3.5 km apart (Fig. IV.1), differ significantly. The two key 400-m-thick sections defined in BAF–2 (Tóth et al. 2022a; Fig. IV.3A) cannot be identified in BAF–4 (Fig. IV.3B). In BAF–4, P10 increased continuously with increasing depth from 0 to 900 m without any sudden changes. According to BHTV data, the average fracture density is 3.6 fracture per meter.

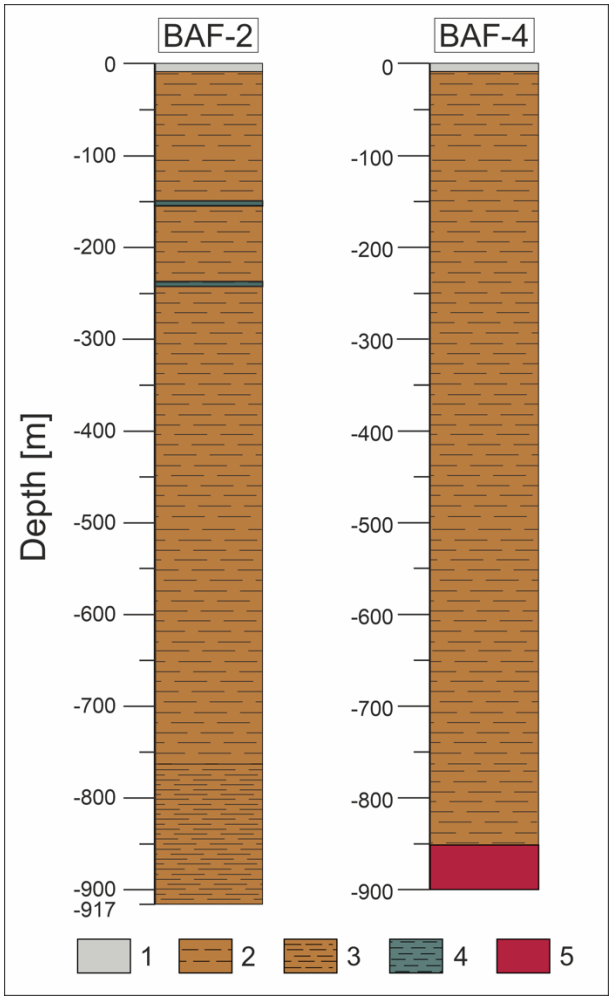

Fig. IV.2 Lithologies of BAF–2 and BAF–4. Legend: (1) quaternary sediments; (2) claystone with siltstone beds; (3) claystone with siltstone and sandstone beds; (4) reductive claystone; (5) rhyolite.

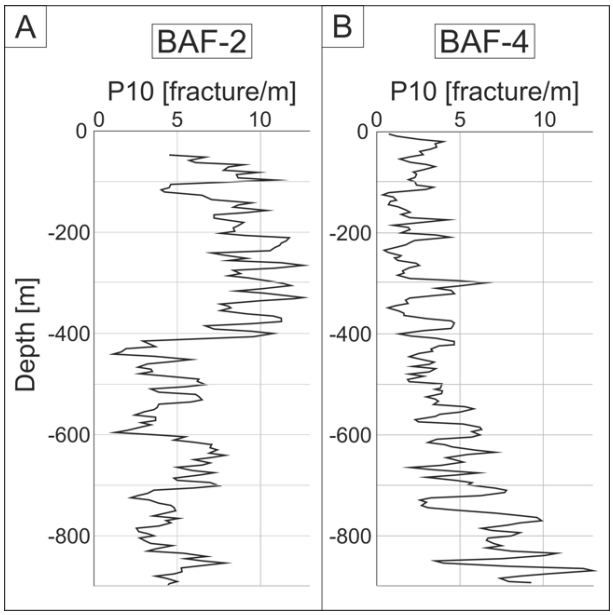

Fig. IV.3 Fracture density in (A) BAF–2 and (B) BAF–4.

IV.4 Results and discussion

IV.4.1 Multiple regression analysis between the fracture density and the geophysical log data

This study examined the relationship between geophysical log data and the fracture density of the rock body by using the software IBM SPSS Statistics, version 28.0. Geophysical well log data from the top section of BAF–4 (220–530 m) were used to train the multiple linear regression model. This section has a lithology typical of the BCF and all of the required geophysical log data. The lower part of BAF–4 (530–840 m) was used to validate the model. Then, the regression function computed in BAF–4 was used to estimate P10 of BAF–2, which was then compared to the measured data. The P10 values for both boreholes were calculated by using BHTV data. The independent variables comprised a standard well log set of the neutron porosity, short-spaced density, natural gamma, and resistivity (e10, e40, and ll3) (Figs. IV.4, IV.5). Conventional log data and the BHTV measurements were carried out by Geo–Log Ltd. There were short sections for which geophysical log data were not available due to technical reasons. These sections were not included in the study. The vertical resolution of the logs was 10 cm. Each log was averaged into 10-m sections with a 5-m overlap (i.e., moving window). These were then compared with the observed P10 values, which were also calculated for 10-m-wide sections from the BHTV data.

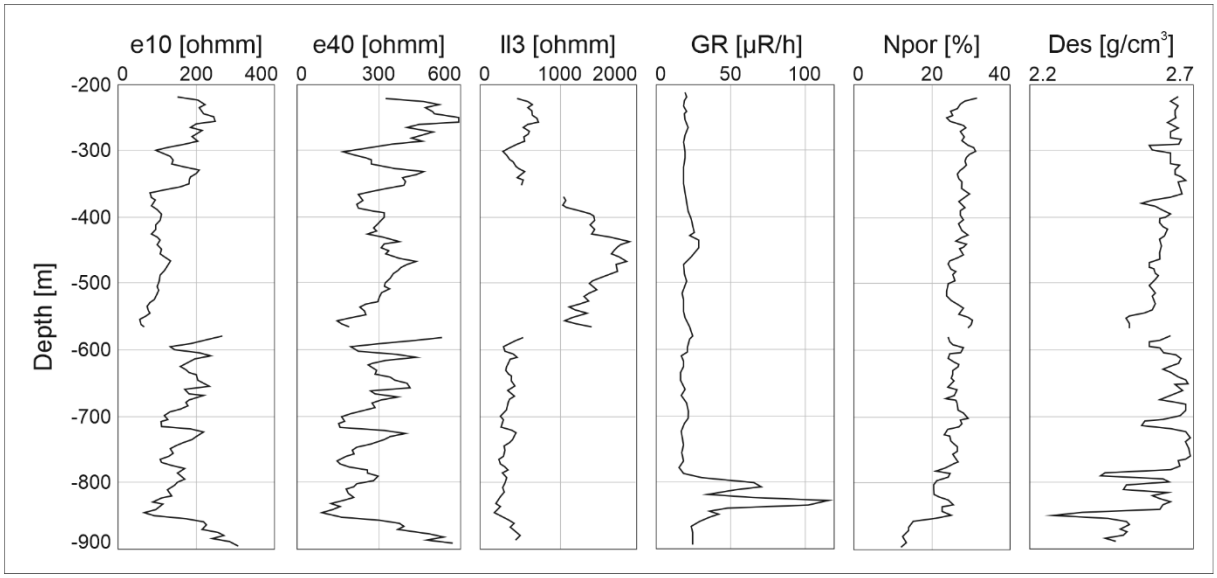

Fig. IV.4 Geophysical logs of BAF–4. Each log is averaged into 10 m wide sections with a 5 m overlap. e10, e40 and ll3: resistivity logs, GR: natural gamma ray, Npor: neutron porosity, Des: density log measured with short-spaced detector. Discontinuities of the logs are caused by a lack of data.

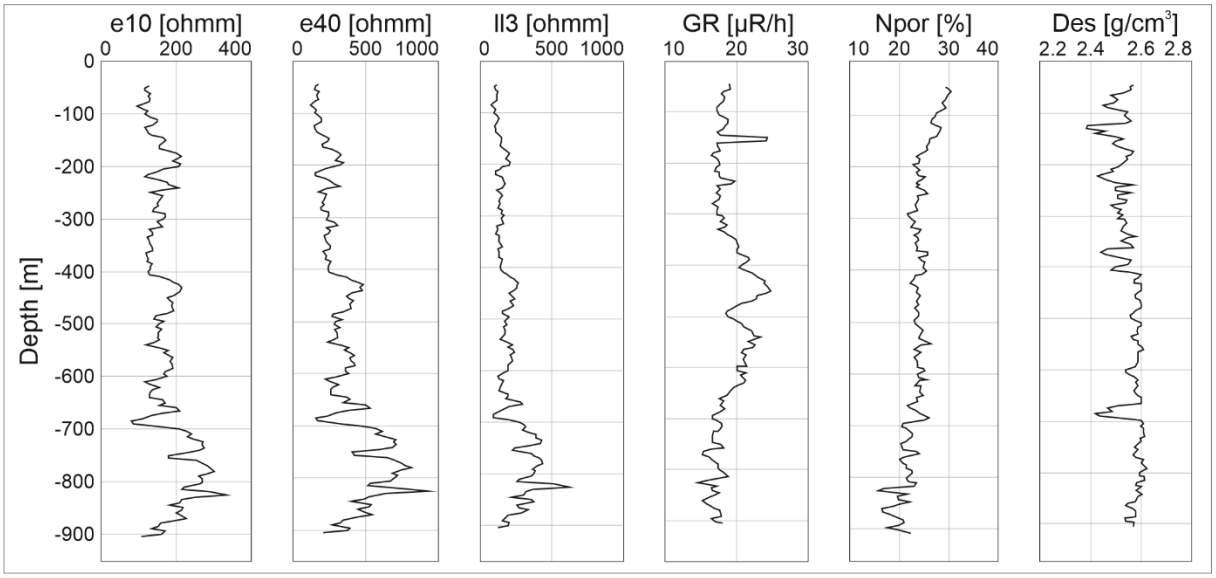

Fig. IV.5 Geophysical logs of the BAF–2. Each log is averaged into 10 m wide sections with a 5 m overlap. e10, e40 and ll3: resistivity logs, GR: natural gamma ray, Npor: neutron porosity, Des: density log measured with short-spaced detector. Discontinuities of the logs are caused by a lack of data.

IV.4.2 Results of the multiple linear regression analysis

A multiple linear regression analysis was run to predict P10 from well log data. The normal distribution of the variables was checked, a log transformation of the natural gamma ray and the density values was required. There was linearity as assessed by partial regression plots. With the backward stepwise regression method all predictors were entered (e10, e40, ll3, lg(GR), lg(Des), Npor, Table IV.1.). The elimination criterion was that, variables whose partial F p-value greater or equal to 0.100 was eliminated from the model (Table IV.1).

Table IV.1Workflow of the multiple linear regression model with backward elimination method, where a variable was removed from the model if partial F p-value was greater or equal to 0.100. During the backward regression analysis ll3, lg(GR) and Npor was removed from the model.

Variables Entered/Removed

Model	Variables Entered	Variables Removed	Method
1	lg(GR), lg(Des), Npor, e40, ll3, e10	-	Enter
2	-	ll3	Backward (criterion: Probability of F-to-remove >= .100).
3	-	lg(GR)	Backward (criterion: Probability of F-to-remove >= .100).
4	-	Npor	Backward (criterion: Probability of F-to-remove >= .100).

Table IV.2 Summary of the models of the backward multiple regression analysis with the R^2, standard error of each model and the Durbin-Watson statistics

Model Summary [e]

Model	R^2	Std. Error of the Estimate	Durbin-Watson
1	.784	.66463	
2	.784	.65724	
3	.779	.65690	
4	.767	.66829	1.426

a. Predictors: (Constant). lg(GR), lg(Des), Npor, e40, LL3, e10

b. Predictors: (Constant). lg(GR), lg(Des), Npor, e40, e10

c. Predictors: (Constant). lg(Des), Npor, e40, e10

d. Predictors: (Constant). lg(Des), e40, e10

e. Dependent Variable: P10

There was independence of residuals, as assessed by a Durbin-Watson statistic of 1.426 (Table IV.2). All three variables of the model are statistically significant to the prediction, $p < .001$ based on t-statistic (Table IV.3.) Multicollinearity was assessed by tolerance values greater than 0.1 (VIF smaller than 10; Franke, 2010). The backward elimination process found two types of resistance logs to be significant, between which there may be a correlation (Table VI.3.). The residuals have normal distribution, with a standard deviation close to 1, MEA = 0.092 (Fig. IV.6).

Table IV.3Coefficients of the multiple regression analysis of model 4 with the collinearity and t-statistics.

Coefficients [a]

Model		Unstandardized Coefficients		t	Sig.	Collinearity Statistics	
		β	Std. Error			Tolerance	VIF
4	(Constant)	76.174	13.285	5.734	<.001		
	lg(Des)	-173.499	33.095	-5.242	<.001	.321	3.114
	e10	.024	.006	3.997	<.001	.098	10.178
	e40	-.018	.002	-7.287	<.001	.170	5.888

a. Dependent Variable: P10

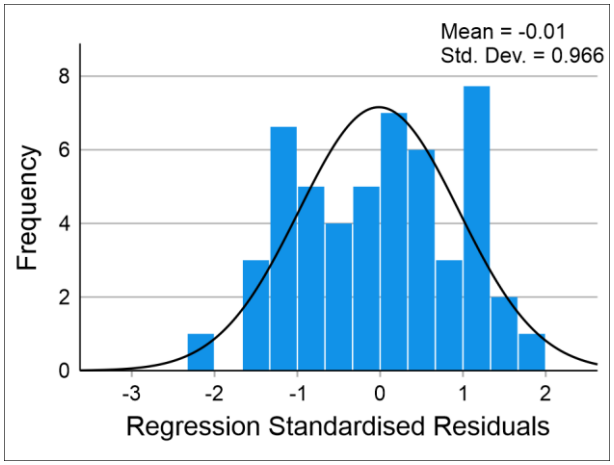

Fig. IV.6 Distribution of the residuals with a mean of -0.01 and a standard deviation of 0.966.

The multiple regression model statistically significantly predicted P10, F(3, 47) = 51.511, $p < .001$, with $R^2 = 0.767$ and $S_e = 0.668$ based on e10, e40 and density data in the upper part of the BAF–4 well (Table 4.). The best fitting regression function was as follows:

$$P10 = 76.174 + 0.024 * e10 - 0.018 * e40 - 173.499 * lg(Des) \qquad \text{(IV.4)}$$

where P10 denotes the fracture density (m^{-1}), e10 and e40 indicate the resistivity [Ωm], Des is the density [g/cm^3].

Table IV.4 ANOVA (analysis of variance) table of the multiple linear regression.

ANOVA [a]

Model		Sum of Squares	df	Mean Square	F	Sig.
4	Regression	69.016	3	23.005	51.511	<.001[b]
	Residual	20.990	47	.447		
	Total	90.006	50			

a. Dependent Variable: P10

b. Predictors: (Constant), lg(DES), e40, e10

In the upper section of BAF–4 (220–530 m), a good fit was obtained by the regression analysis with R^2 =0.767, (Figs. IV.7A, IV.8A). The residuals are the difference between the observed value and value predicted by the model. A slight correlation was obtained between the residuals and P10, and the residuals increased slightly with P10 (Fig. IV.7B).

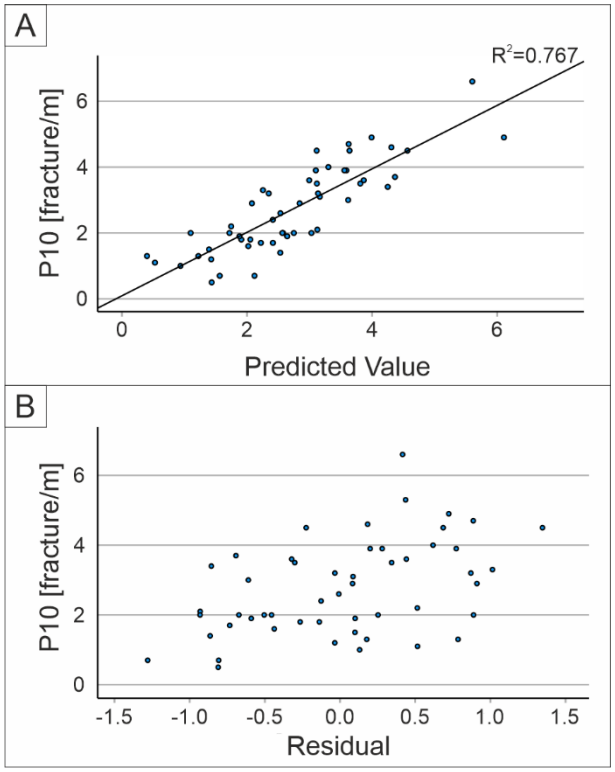

Fig. IV.8 Linear regression analysis: observed P10 values plotted against (A) predicted P10 in BAF–4 at 220–530 m and (B) residuals (i.e., difference between the data points and regression line)

In the lower section of BAF–4 (530–850 m), fracture density can be predicted using the same function with good accuracy, except the section between 750 and 780 m, where the predicted and measured P10 values differ noticeably (Fig. IV.8B). In this section the predicted P10 values underestimated the measured P10. Correlation coefficient between 530 and 750 m is $R^2 = 0.630$, $S_e = 1.623$, MEA = 1.024.

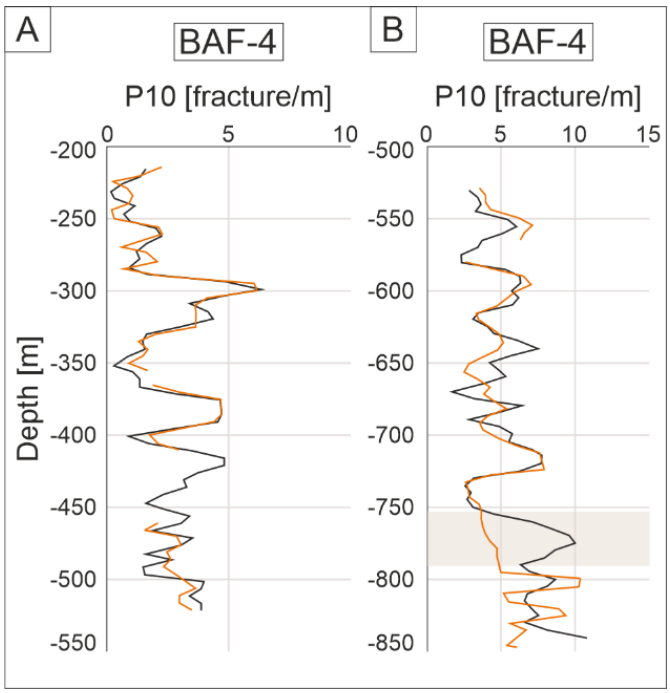

Fig. IV.9 Predicted and measured P10 values with the depth of BAF–4: (A) in the training section at 230–530 m and (B) in the predicted section at 530–850 m. Black line: measured P10, orange line: predicted P10, grey area: section with lower prediction accuracy

The regression model function computed by using the upper segment of BAF–4 was applied to predict P10 along BAF–2 (Fig. IV.9). The correlation between the measured and predicted P10 values was strong with $R^2 = 0.701$, $S_e = 2.239$, MEA = 2.533. The predicted P10 values closely matched the dichotomy of the borehole. However, P10 was slightly underestimated in the upper 400 m, which was highly fractured. Below 400 m, in the lower half of the well, the prediction was accurate including the section at 400–600 m, which was the least fragmented section of the well (Fig. IV.9). At 700–860 m, P10 was underestimated. In some extreme cases (e.g., at 720, 780, and 820 m), the model function predicted a negative P10 value because it underestimated the very low measured P10 value. Obviously, a negative fracture density is not possible.

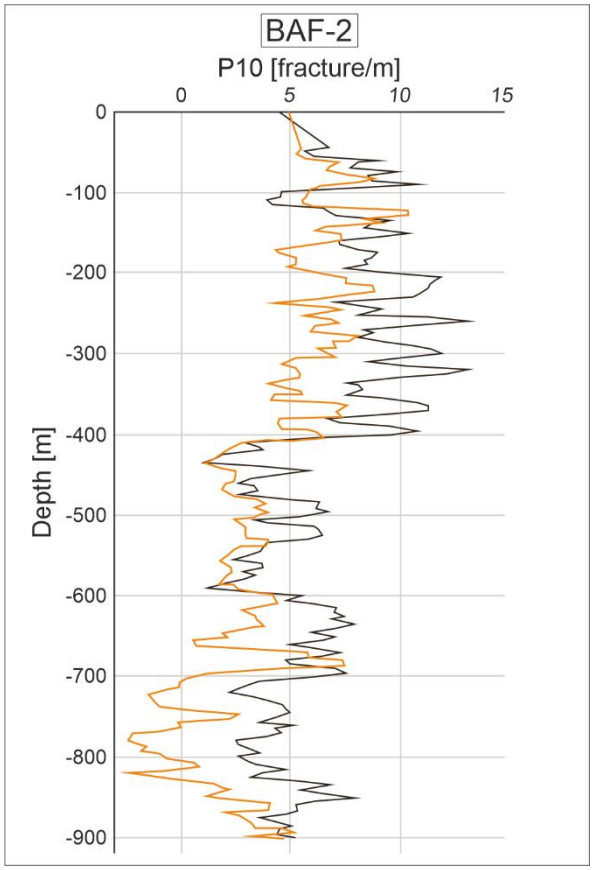

Fig. IV.10 Predicted (orange line) and measured (black line) P10 values with the depth in BAF–2

IV.4.3 Limitations and implications

The resistivity and density were the primary influencing factors of P10. The resistivity is related to formation fluid saturation and depends on the rock type, porosity, type, composition, and volume of fluid (Archie 1942). Resistivity measurements are usually used to identify permeable sections and estimate the porosity. Because resistivity logs are available to

locate permeable intervals in an essentially impermeable host rock, they are suitable for determining fractured zones. The neutron porosity and density also showed correlations in the partial regression plot with P10. Because a larger number of open fractures may increase porosity and decrease bulk density, these logs may also be used to identify fractured zones. Natural gamma-ray logs are used to detect gamma radiation, which is linked to the amount of clay in the host rock. This lithological factor may affect the rheology of the claystone through the grain size and clay content, which can influence the formation and propagation of fractures (Eisenstadt and Sims 2005). Based on the multiple regression analysis of the BAF, neutron porosity and gamma radiation did not influence significantly the fracture density in the formation.

The determined correlation coefficients were significantly impacted by the lithology of the section under study. Because the rock body of the BCF showed little variation in its lithology (Halász 2009; Halász and Halmai 2015), P10 can be predicted using the above multiple linear regression function for much of the formation. However, the estimated and measured P10 values diverged more than usual at several sections in the analysed boreholes: at 750–780 m in BAF–4 and at 700–860 m in BAF–2.

In BAF–4, the model function underestimated P10 at 750–780 m, at this section, the BHTV detected more discontinuities than predicted. Core images (Fig. 10) show that this interval contains substantially thinner layers than typical for the BCF. The BHTV registers all planar objects in the borehole; therefore, the raw data used to calculate P10 included both the bedding planes and fractures. The P10 prediction based on the geophysical log data was less accurate for this section because these beds do not affect the geophysical characteristics of the rock body. The difference between the observed and estimated values shows that, in the laminated zones of the claystone, the actual P10 value may be significantly lower than the calculated value from considering all discontinuities.

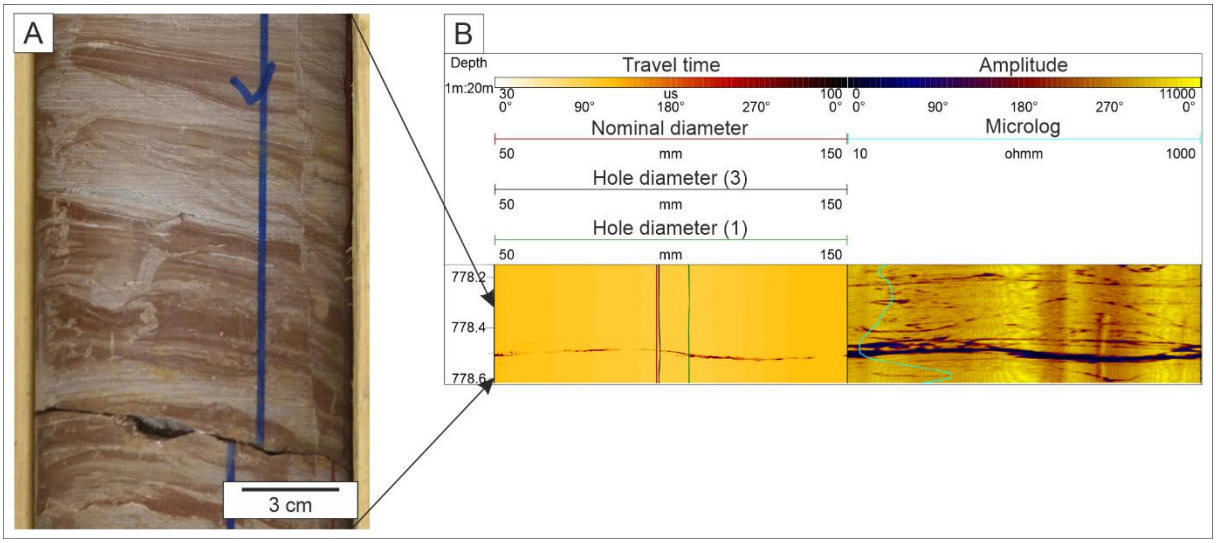

Fig. IV.11 (A) Core sample of BAF–4 between 778.37 and 778.52 m. Thin-layered claystone was detected by the BHTV. Blue arrow: downward direction. (B) BHTV image from the same depth, thin layers of the claystone can be detected on the BHTV image on the right.

Because the function of the linear regression model was trained by using the upper portion (220–530 m) of BAF–4, the prediction was less accurate in lower parts of the BCF, which had a larger average grain size. When the regression model function was applied to BAF–2, it showed a similar behaviour. Here, the slight decrease in accuracy toward the bedding may be attributed to a gradual change in the lithology (i.e., coarsening grain size). P10 was most significantly underestimated below 700 m, where the fine sandstone layers were common. For accurate prediction of the sandy parts, another regression analysis should be performed on this section. However, there is no way to validate the calculation on another section with fine sandstone layers among the available boreholes of the BCF. In addition, the sandy part of the BCF is a less important concern regarding the choice of the repository site because the repository should be built in a part with the best sealing properties.

The above results suggest that the prediction accuracy of the regression analysis was primarily affected by the lithology of the rock body. For intervals of typical lithology and consequently representative well log data, P10 can be predicted with a high degree of accuracy. However, special attention must be paid to intervals with atypical well log data suggesting unique changes in the lithology, such as a larger than average grain size or laminar layers.

IV.5. Conclusion

In this study, the relationship between P10 and different geophysical log data were examined for the BCF, which is a potential host for a high-level nuclear waste repository. Two boreholes more than 900 m deep provided a unique opportunity to explore the fracture network

characteristics of the BCF. Regression analysis showed a strong linear relationship between P10 and selected geophysical log data. The main influencing factors for P10 were the resistivity (e10, e40) and density. The coefficients of the regression model function were trained on the upper half of BAF–4. The function was then used to predict P10 with high accuracy for other sections typical of the BCF.

In some sections where the lithological properties were atypical, the prediction was less accurate. The lower part of the BCF contains fine sandstone layers, and this change in grain size may have influenced the geophysical properties. In these sandy sections, the function underestimated P10.

The established linear regression model function for the BCF may be used to determine the fracture density in older boreholes that intersect the formation where BHTV log data are not available. By involving more boreholes, the presented approach may provide more information about the spatial extension of communicating fracture clusters and large-scale structural elements such as fault zones.

CHAPTER V.

Conclusion

In this work, I have studied the structural elements of the Boda Claystone Formation (BCF) on a wide scale in several wells that penetrated the formation in large thickness. This formation has been in the focus of Hungarian geological research for the last 30 years, since the BCF is the designated host rock for high-level nuclear waste in Hungary (Konrád & Hámos, 2006). The structural geological study of the formation could be of paramount importance for the disposal of wastes, it is important to evaluate the tectonic evolution of the host rock, the hydrogeological significance of the tectonic structures and their role in fluid flow (Delay, 2010). This study includes the microstructural investigation of the sigmoidal-shaped veins up to the investigation of the geometry of the fracture system and the fracture density of the BCF based on two wells.

The BCF contains a large number of sigmoidal veins, which are particular structural elements of the formation, in well BAF−2 there are more than 200 sigmoidal vein arrays. The development of these structures is caused by shear strain in shear zones. Therefore, the shape of the sigmoidal veins is a good deformation marker, these structures can be used to estimate the amount of strain and volume change in the shear zone (Ramsay & Huber, 1983). The analysis of the geometry of the veins concluded, that the shear zone had moderate shear strain. Despite the vein forming processes and mineral precipitation, which accompany their evolution, the shear zones in the BCF suffered volume loss. This phenomenon is proved by micro-CT and mass balance analyses. The density of the rock bridges between the veins is higher than the density of the wall rock, and the 2D porosity also decreases between the veins compared to the wall rock. Consequently, the volume loss and porosity reduction of the shear zone took place in the rock bridges due to tectonic compaction. Based on the mass balance analysis, the shear zone is enriched in Ca, Ba, Sr, S and Mn, and is not depleted in any element. The enrichment of these elements is related to the mineral precipitation in the veins. The mineral composition of these veins include calcite, anhydrite, barite and celestine. Sigmoidal veins usually form in sandstones and limestone, where pressure solution always accompanies this type of vein formation. Contrary, the role of pressure solution is restricted in a claystones. In the case of the BCF, the veins develop without the sign of pressure solution. Based on my analysis I proposed a new formation mechanism for the sigmoidal veins in the BCF. The sharp triangular edges of the veins suggest that they are pennant veins (Coelho et al., 2006), and conjugate Riedel fractures control their kinematics during the formation of the vein arrays. The group of sigmoidal veins is one of the youngest vein generation of the four vein generations (Hrabovszki

et al. 2017) of the BCF; their formation is not older than the folding and tilting of the rock body, Cretaceous in age.

The geometry of the fracture network was modelled using a DFN modelling approach in the BAF−2 well. Five possible fracture network geometries can be distinguished in the well, with equal probabilities, due to the stochastic nature of the simulation method. In the worst-case scenario, in terms of retentive properties, the fractures form a single communicating system along with the entire borehole, from 0 m down to 900 m. In several cases, the fracture system is divided into two subgroups at different depths (300, 400 or 700 m). In other runs, the fracture system of the well can be subdivided into four blocks that do not communicate with each other; the boundaries are at 100, 400 and 700 m. The hydrogeological evaluation of the fracture system of the BAF−2 well was carried out using the flow zone indicator (FZI). This parameter denotes hydraulic flow units based on the covariation of porosity and permeability. Since the matrix porosity and permeability of the host rock are insignificant, the calculated porosity and permeability values describe the behaviour of the fracture system. The FZI determines seven hydraulic flow units within the BAF−2 well. Most of them fit into a trend representing the average, typical behaviour of the fracture system in the BCF; while three zones, which are few tens of meters wide, form another trend with elevated FZI values compared to the typical one. These independent hydraulic units are located between 60−110, 350−420 and 690−770 m. The first one, at the top section of the formation, is formed by weathering, as a result of near surface processes. At 400 m a large-scale fault zone is indicated, which is probably an inverse fault based on the tectonic evolution of the region. The average grain size of the formation is increasing with the depth and sandstone beds become more frequent in the lower part of the rock body. This lithological change could affect the hydrogeological properties of the rock body and form the hydraulic flow unit at 700 m. These hydraulic flow units denote the same boundaries shown by the DFN modelling in terms of fracture network connectivity. Based on these results, the rock body of the BAF−2 well could be divided into four blocks, with boundaries at 100, 400 and 700 m.

The relationship between the geophysical log data and fracture density was analysed using multiple linear regression analysis. Strong linear relationship is observed between the geophysical properties and the fracture density based on the analysis of core data of BAF−2 and BAF−4 wells. The main factors affecting fracture density are resistivity and density. This investigation suggests that the attributes recorded in a borehole regarding the fracture network can be extended between wells.

Designation of the repository requires detailed information on the geometry of the fracture network, location of the fractured zones and large-scale structural elements. Therefore,

the fracture network of all available boreholes of the formation should be investigated. Fracture density is the simplest attribute to compare the fracture networks of different boreholes. The established regression equation can be used to estimate the fracture density in older wells for which no BHTV data are available. The location and extent of communicating fracture clusters and large-scale fracture zones could be identified and analysed by combining the estimated fracture densities of older wells with the available fracture network models from BAF−2, BAF−3 (Tóth et al. 2022c), BAF−3A and BAF−4 (Tóth et al. 2022b). In addition to the fracture network models of the BCF, the calculated effective porosity and permeability could serve as a basis for hydraulic and transport modelling of the formation in the future.

ACKNOWLEDGEMENT

First and foremost, I am deeply grateful to my two supervisors Tivadar M. Tóth and Félix Schubert for their support and encouragement throughout my years at the university. I warmly thank M. Tóth Tivadar for his generous supervision, and invaluable guidance which shaped the direction of my research. I wish to express my thank to Félix Schubert for his motivational lectures on structural geology, which were the first to draw my interest to the field and introduced me to the study of the Boda Claystone Formation.

I would like to thank my colleague Ervin Hrabovszki for his assistance, advice, and thought-provoking discussions regarding our research topic.

I appreciate Zoltán Máthé and Péter Mucsi for supplying the data I needed for my study and for their quick replies to my inquiries.

I would like to express my appreciation to Mecsekérc PLC and to Public Limited Company for Radioactive Waste Management for enabling me to perform this study and for supplying the data.

The research was financially supported by the National Research, Development and Innovation Office (grant no. K-138919) and the University of Szeged Open Access Fund (grant no. 4608, no. 5454, no. 6126). Publications part of this study were edited for English language and spelling by Enago, an editing brand of Crimson Interactive Inc, sponsored by the University of Szeged. Financial support for purchasing the CT instrument was provided by the Hungarian National Research, Development and Innovation Office through project GINOP-2.3.3-15-2016-00010.

I would like to thank all the reviewers of the papers published as part of this study for their valuable feedback and suggestions, which greatly improved the quality of my work.

I would like to express my gratitude to the very pleasant and supportive day-to-day environment during my PhD studies, including all the members of the PhD room at the Department of Mineralogy, Geochemistry and Petrology.

I am also grateful to my family for their love, support, and encouragement throughout this journey. Last but not least, I would want to express my gratitude to Szilárd, my fiancé, for his unwavering love, support, and patience throughout my PhD studies.

REFERENCES

Aghli, G., Soleimani, B., Moussavi-Harami, R., Mohammadian R., 2016. Fractured zones detection using conventional petrophysical logs by differentiation method and its correlation with image logs. Journal of Petroleum Science and Engineering 142:152–162. https://doi.org/10.1016/j.petrol.2016.02.002

Ahn, J, Apted M. J., (eds) 2010. Geological repository systems for safe disposal of spent nuclear fuels and radioactive waste. Woodhead Publ, Oxford Cambridge

Al-Dhafeeri, A. M., Nasr-El-Din, H. A., 2007. Characteristics of high-permeability zones using core analysis, and production logging data. Journal of Petroleum Science Engineering 55, 18–36. https://doi.org/10.1016/j.petrol.2006.04.019

Alin, A., 2010. Multicollinearity. WIREs Computational Statistics, 2, 370-374. https://doi.org/10.1002/wics.84

Amaefule, J. O., Altunbay, M., Tiab, D., Kersey, D. G., and Kedan, D. K., 1993. Enhanced reservoir description: Using core and log data to identify hydraulic (flow) unites and predict permeability in uncored intervals/wells. SPE 26436, SPE Annual Technical Conference and Exhibition, Houston, Texas. https://doi.org/10.2118/26436-MS

Anders, M. H., Laubach, S. E., Scholz, C. H. 2014. Microfractures: A review. Journal of Structural Geology 69:377–394. https://doi.org/10.1016/j.jsg.2014.05.011

Anders, M. H., Laubach, S. E., Scholz, C. H. 2014. Microfractures: A review. Journal of Structural Geology 69:377–394. https://doi.org/10.1016/j.jsg.2014.05.011

Andrássy, M., Dankó, Gy., Darvas, K., Farkas, M. P., Korpai, F., Talpas, L., 2018. Hydrofracking and hydraulic packer testing in the framework of Boda Claystone Formation (BCF) geological investigation program in the Kővágószőlős southern anticline tectonic block. Bodai Agyagkő Formáció kutatás szakmai előadói nap kiadványa (Lecture day of the Boda Claystone Formation research), Pécs (in Hungarian).

Apted, M., Ahn, J. 2010. Multiple-barrier geological repository design and operation strategies for safe disposal of radioactive. Geological Repository Systems for Safe Disposal of Spent Nuclear Fuels and Radioactive Waste, Woodhead Publishing Series in Energy 3–28 https://doi.org/10.1533/9781845699789.1.3

Archie, G. M. 1942. The Electrical Resistivity Log as an Aid in Determining Some Reservoir Characteristics. Transactions of the AIME 146:54–62

Archie, G. M. 1942. The Electrical Resistivity Log as an Aid in Determining Some Reservoir Characteristics. Transactions of the AIME 146:54–62

Árkai, P., Demény, A., Fórizs, I., Nagy, G., Balogh, K., Máthé, Z., 2000. Composition, diagenetic and post-diagenetic alterations of a possible radioactive waste repository site: The Boda Albitic claystone formation, southern Hungary. Acta Geologica Hungarica 43, 351–378.

Barker, S.L.L., Cox, S.F., Eggins, S.M., Gagan, M.K., 2006. Microchemical evidence for episodic growth of antitaxial veins during fracture-controlled fluid flow. Earth and Planetary Science Letters 250, 331–344. https://doi.org/10.1016/j.epsl.2006.07.051

Barton, C. C., Larsen, E., 1985. Fractal geometry of two-dimensional fracture networks at Yucca Mountain, Southwestern Nevada. In: Stephanson, O. (Ed.), Proceedings of International Symposium on Fundamentals of Rock Joints 77–84.

Barton, N., 2014. Non-linear behaviour for naturally fractured carbonates and frac-stimulated gas-shales: First Break 32/2031, 51–66. https://doi.org/10.3997/1365-2397.2014011

Bauer M., M. Tóth, T., 2017. Characterization and DFN modelling of the fracture network in a Mesozoic karst reservoir: Gomba oilfield, Paleogene Basin, Central Hungary. Journal of Petroleum Geology 40/3, 319–334. https://doi.org/10.1111/jpg.12678

Beach, A., 1975. Geometry of En-Echelon Vein Arrays. Tectonophysics 28, 245–263. https://doi.org/10.1016/0040-1951(75)90040-2

Bear, J., 1972. Dynamics of fluids in porous media. American Elsevier Pub. Co., New York.

Benkovics, L., Mansy, J-L., Csontos, L., Bergerat, F., 1997. Folding in the Abaliget road cut (Mecsek Mountains). Acta Geologica Hungarica 40/4, 425–440.

Bergerat, F., Csontos, L., 1988. Brittle tectonics and paleo-stress field in the Mecsek and Villány Mts (Hungary): correlation with the opening mechanism of the Pannonian Basin. Acta Geologica Hungarica 31, 81–100.

Berkowitz, B., 1995. Analysis of fracture network connectivity using percolation theory. Mathematical Geology 27/4, 467–483. https://doi.org/10.1007/BF02084422

Berkowitz, B., 2002. Characterizing flow and transport in fractured geological media: a review. Advanced Water Resources, 25, 861–884. https://doi.org/10.1016/S0309-1708(02)00042-8

Bernáth, Gy., 2015. Lyukgeofizikai értékelés. In: Sámson, M. (Ed.), 2015. BAF–2 fúrás dokumentáló és értékelő jelentése. (Documentation and evaluation of the BAF–2 well). Research Report, Public Limited Company for Radioactive Waste Management (RHK Kft.), Pécs, (in Hungarian).

Bernáth, Gy., Gärtner, D., Zilahi-Sebess, L., Prohászka, A., Hegedűs, S., 2014. A BAF–2 jelű magfúrás mélyfúrás-geofizikai dokumentálása és értékelése (Geophysical documentation

and evaluation of the BAF–2 well). Research Report, Geo-Log Környezetvédelmi és Geofizikai Kft., Budapest (in Hungarian).

Bisdom, K., Bertotti, G., Nick, H., 2016. A geometrically based method for predicting stress-induced fracture aperture and flow in discrete fracture networks. AAPG Bulletin 100, 1075–1097. https://doi.org/10.1306/02111615127

Bons, P.D., Elburg, M.A., Gomez-Rivas, E., 2012. A review of the formation of tectonic veins and their microstructures. Journal of Structural Geology 43, 33–62. https://doi.org/10.1016/j.jsg.2012.07.005

Bowerman, B. L., O'Connell, R. T. Koehler, A. B., 2005. Forecasting, time series and regression. 4 th ed. United States of America: Brooks/Cole Thomson Learning Inc.

Brace, W. F., Riley, D. K., 1972. Static uniaxial deformation of 15 rocks to 30 kb. International Journal of Rock Mechanics and Mining Sciences 9, 271–288. https://doi.org/10.1016/0148-9062(72)90028-9

Cheng, C., Hale, S., Milsch, H., and Blum, P., 2020. Measuring hydraulic fracture apertures: a comparison of methods, Solid Earth 11, 2411–2423. https://doi.org/10.5194/se-11-2411-2020

Childs, C., Walsh, J. J., Watterson, J., 1997. Complexity in fault zone structure and implication for fault seal prediction. In: Moller-Pedersen, P., Koestler, A.G. (Eds.), Hydrocarbon Seals. Elsevier. https://doi.org/10.1016/S0928-8937(97)80007-0

Christoforidis, T., Katrakilidis, C., Karakotsios, A., Dimitriadis, D. 2021: The dynamic links between nuclear energy and sustainable economic growth. Do institutions matter? Progress in Nuclear Energy, 139, 103866, https://doi.org/10.1016/j.pnucene.2021.103866

Cobbold, P.R., Rodrigues, N., 2007. Seepage forces, important factors in the formation of horizontal hydraulic fractures and bedding-parallel fibrous veins ('beef' and cone-in-cone). Geofluids 7, 313–322. https://doi.org/10.1111/j.1468-8123.2007.00183.x

Coelho, S., Passchier, C., Marques, F., 2006. Riedel-shear control on the development of pennant veins: Field example and analogue modelling. Journal of Structural Geology 28, 1658–1669. https://doi.org/10.1016/j.jsg.2006.05.009

Csicsák, J., 1999. Hidrológiai, hidrokémiai vizsgálati program (Hydrological, hydrochemical study). Research Report, Mecsekérc Zrt., Pécs (in Hungarian).

Csontos, L., Benkovics, L., Bergerat, F., Mansy, J-L., Wórum, G., 2002. Tertiary deformation history from seismic section study and fault analysis in a former European Tethyan margin (the Mecsek–Villány area, SW Hungary). Tectonophysics 357, 81–102. https://doi.org/10.1016/S0040-1951(02)00363-3

Csontos, L., Bergerat, F., 1992. Reevaluation of the Neogene brittle tectonics of the Mecsek–Villány are (SW Hungary). Annales Universitatis Scientiarum Budapestinensis de Rolando Eötvös Nominatae. Sectio geologica 29, 3–12.

Delay, J. 2010. Clay geological repository systems: characterisation and site surveying technologies and techniques. Geological Repository Systems for Safe Disposal of Spent Nuclear Fuels and Radioactive Waste. Woodhead Publishing Series in Energy 153–187 https://doi.org/10.1533/9781845699789.2.153

Deng, H., Steefel, C., Molins, S., DePaolo, D., 2018. Fracture Evolution in Multimineral Systems: The Role of Mineral Composition, Flow Rate, and Fracture Aperture Heterogeneity. Earth and Space Chemistry 2/2, 112–124. https://doi.org/10.1021/acsearthspacechem.7b00130

Dezfoolian, M. A., 2013. Flow Zone Indicator Estimation Based on Petrophysical Studies Using an Artificial Neural Network in a Southern Iran Reservoir, Petroleum Science and Technology 31/12, 1294–1305. https://doi.org/10.1080/10916466.2010.542421

Dong, S., Zeng, L., Lyu, W., Xia, D., Liu, G., Wu, Y., Du, X., 2020. Fracture identification and evaluation using conventional logs in tight sandstones: A case study in the Ordos Basin, China. Energy Geoscience 1, 115–123. https://doi.org/10.1016/j.engeos.2020.06.003

Eberly, L. E., 2007. Multiple linear regression. Methods in molecular biology 404:165–187. https://doi.org/10.1007/978-1-59745-530-5_9

Einsteind, H. H., Baecher, G. B. 1983. Probabilistic and statistical methods in engineering geology. Rock Mechanics and Rock Engineering, 16/1 39–72. https://doi.org/10.1007/BF01030217

Eisenstadt, G., Sims, D., 2005. Evaluating sand and clay models: do rheological differences matter? Journal of Structural Geology 27, 1399–1412. https://doi.org/10.1016/j.jsg.2005.04.010

Fodor, L., Csontos, L., Bada, G., Györfi, I., Benkovics, L., 1999. Tertiary tectonic evolution of the Pannonian Basin system and neighbouring orogens: a new synthesis of palaeostress data. In: Durand, B., Jolivet, L., Horváth, F., Séranne, M. (Eds.), The Mediterranean Basins: Tertiary Extension within the Alpine Orogen. Geological Society, London, Special Publications 156, 295–334. https://doi.org/10.1144/GSL.SP.1999.156.01.15

Franke, G. R., 2010. Multicollinearity. In Wiley International Encyclopedia of Marketing (eds Sheth, J., Malhotra, N.). https://doi.org/10.1002/9781444316568.wiem02066

Freund, R. J., Wilson, W. J., Sa, P., 2006. Regression analysis: statistical modeling of a response variable, 2nd ed. Elsevier Academic Press, Burlington, MA

Gamal, M., El-Araby, A. A., El-Barkooky, A. N., Hassan, A., 2022. “Detection and characterization of fractures in the Eocene Thebes formation using conventional well logs in October field, Gulf of Suez, Egypt.” Egyptian Journal of Petroleum 31, 1–9. https://doi.org/10.1016/j.ejpe.2022.06.001

Ge, Z., Pan, S., Li, J., Zhang, D., Luo, H., 2020. Estimation of weak anisotropy parameters and fracture density of asymmetric fractures in monoclinic medium. Journal of Geophysics and Engineering 17, 1049–1064. https://doi.org/10.1093/jge/gxaa063

Gentier, S., Hopkins, D., Riss, J., 2000. Role of fracture geometry in the evolution of flow path under stress. Dynamic of Fluids in Fractured Rock, Geophysical Monograph 122, 169–184. https://doi.org/10.1029/GM122p0169

Giumaraes, V., Bobos, I., 2021. Sorbents Materials for Controlling Environmental Pollution Current State and Trends. 513–541 Chapter 20 – Role of clay barrier systems in the disposal of radioactive waste

Gong, Q.J., Yan, T.T., Li, J.Z., Zhang, M., Liu, N.Q., 2016. Experimental simulation of element mass transfer and primary halo zone on water-rock interaction. Applied Geochemistry 69, 1–11. https://doi.org/10.1016/j.apgeochem.2016.04.001

Götze, J., 2012. Application of Cathodoluminescence Microscopy and Spectroscopy in Geosciences. Microscopy and microanalysis 18/6, 1270–1284. https://doi.org/10.1017/S1431927612001122

Grant, J.A., 1986. The Isocon Diagram - a Simple Solution to Gresens Equation for Metasomatic Alteration. Economic Geology 81, 1976–1982. https://doi.org/10.2113/gsecongeo.81.8.1976

Grant, S. A., 2005. Hydraulic properties, temperature effects. In: Hillel, D., (Ed.) Encyclopedia of Soils in the Environment Elsevier, 207–211.

Gresens, P. L., 1967. Composition-volume relationships of metasomatism. Chemical Geology 2, 47–65 https://doi.org/10.1016/0009-2541(67)90004-6

Gudmundsson, A., Berg, S. S., Lyslo, K. B., Skurtveit, E., 2001. Fracture networks and fluid transport in active fault zones. Journal of Structural Geology 23 2/3, 343–353. https://doi.org/10.1016/S0191-8141(00)00100-0

Guntoro, P.I., Ghorbani, Y., Koch, P.-H., Rosenkranz, J. 2019. X-ray microcomputed tomography (μct) for mineral characterization: A review of data analysis methods. Minerals 9, 20–26. https://doi.org/10.3390/min9030183

Haas, J., Péró, C., 2004. Mesozoic evolution of the Tisza Mega-unit. International Journal of Earth Sciences 93, 297–313. https://doi.org/10.1007/s00531-004-0384-9

Halász, A., 2009. Cycles and rhythms within the Boda Claystone Formation in WELL Ib-4. Central European Geology 52, 325–342. https://doi.org/10.1556/CEuGeol.52.2009.3-4.7

Halász, A., Halmai, Á., 2015. The colour analysis method applied to homogeneous rocks. Geologos 21, 233–239. https://doi.org/10.1515/logos-2015-0019

Hancock, P., 1972. The analysis of en-échelon veins. Geological Magazine, 109/3, 269–276. https:// 10.1017/S0016756800039315

Holland, M., Urai, J. L., van derZee, W., Stanjek, H., Konstanty, J., 2006. Fault gouge evolution in highly overconsolidated claystones. Journal of Structural Geology 28/2, 323–332. https://doi.org/10.1016/j.jsg.2005.10.005

Hoteit, N., Shao, J. F., Su, K., Tijani, M., 2002. Hydromechanical and Thermohydromechanical Behaviour of Deep Argillaceous Rock: Theory and Experiments, CRC Press, Boca Raton, USA ISBN 9789058095336

Hrabovszki, E., Tóth, E., M. Tóth, T., Garaguly, I., Futó, I., Máthé, Z., Schubert, F., 2022. Geochemical and microtextural properties of veins in a potential high-level radioactive waste disposal site. Journal of Structural Geology 154, 104490. https://doi.org/10.1016/j.jsg.2021.104490

Hrabovszki, E., Tóth, E., M. Tóth, T., Máthé, Z., Schubert, F., 2020. Potential formation mechanisms of early diagenetic displacive veins in the Permian Boda Claystone Formation. Journal of Structural Geology 138, 104098. https://doi.org/10.1016/j.jsg.2020.104098

Hrabovszki, E., Tóth, E., Raucsik, B., Varga, A., Schubert, F., 2017. Microstructure and cementation analyses on core samples from the BAF–2 well (Boda Claystone Formation, Mecsek Mts). Bulletin of the Hungarian Geological Society 147/3, 245–264. (in Hungarian with English abstract). https://doi.org/10.23928/foldt.kozl.2017.147.3.245

IEA (International Energy Agency), 2012. CO2 emissions by product and flow, IEA CO2 Emissions from Fuel Combustion Statistics (database).

Ja'fari, A., Kadkhodaie-Ilkhchi, A., Sharghi, Y., Ghanavati, K. 2012. Fracture density estimation from petrophysical log data using the adaptive neuro-fuzzy inference system. Journal of Geophysics and Engineering 9, 105–114. https://doi.org/10.1088/1742-2132/9/1/013

Kanit, T., Forest, S., Galliet, I., Mounoury, V., Jeulin, D., 2003. Determination of the size of the representative volume element for random composites: statistical and numerical approach. International Journal of Solids and Structures 40, 3647–3679. https://doi.org/10.1016/S0020-7683(03)00143-4

Kawamura, T., 1990. Nondestructive, 3-Dimensional Density-Measurements of Ice Core Samples by X-Ray Computed-Tomography. Journal of Geophysical Research Solid Earth 95, 12407–12412. https://doi.org/10.1029/JB095iB08p12407

Keller, A., 1998. High resolution, non-destructive measurement and characterization of fracture apertures. International Journal of Rock Mechanics and Mining Science 35/8, 1037–1050. https://doi.org/10.1016/S0148-9062(98)00164-8

Konrád, Gy., Hámos, G., 2006. Geological aspects of determining high activity radioactive waste depository sites in Hungary and the results of the recent research. Acta Geographica ac Geologica et Meteorologica Debrecina 01, 33–38.

Konrád, Gy., Sebe, K., 2010. New details of young tectonic phenomena in the Western Mecsek Mts and their surroundings. Bulletin of the Hungarian Geological Society 140, 135–162. (in Hungarian with English abstract).

Konrád, Gy., Sebe, K., Halász, A., 2015. Földtani-tektonikai értékelés In: Sámson, M. (Ed.), 2015. BAF–2 fúrás dokumentáló és értékelő jelentése. (Documentation and Evaluation of the BAF–2 well). Research Report, Public Limited Company for Radioactive Waste Management (RHK Kft.), Pécs, (in Hungarian).

Konrád, Gy., Sebe, K., Halász, A., Babinszki, E., 2010. Sedimentology of a Permian playa lake: the Boda Claystone Formation, Hungary. Geologos 16, 27–41. https://doi.org/10.2478/v10118-637 010-0002-1

Krauskopf, K. B., 1988. Radioactive waste disposal and geology, Springer, Dordrecht. https://doi.org/10.1007/978-94-009-1201-4

Kumar, S., Bodvarsson, G. S., Boernge, J., 1991. Fractal characteristics of fracture roughness and aperture data. High-Level Nuclear Waste Management, Proceedings of the Second International Conference, Las Vegas, Nevada, 279–284.

La Pointe, P. R., 1988. A method to characterize fracture density and connectivity through fractal geometry. International Journal of Rock Mechanics and Mining Science & Geomechics Abstracts 25, 421–429. https://doi.org/10.1016/0148-9062(88)90982-5

Laubach SE, Baumgardner RW, Monson ER, et al (1988) Fracture Detection in Low-Permeability Reservoir Sandstone: A Comparison of BHTV and FMS Logs to Core. In: All Days. SPE, Houston, Texas, p SPE-18119-MS

Laubach, S. E., Olson, J. E., Gale, J. F., 2004. Are open fractures necessarily aligned with maximum horizontal stress?: Earth and Planetary Science Letters 222/1, 191–195. https://doi.org/10.1016/j.epsl.2004.02.019

Lázár, K., Máthé, Z., 2012. Claystone as a potential host rock for nuclear waste storage. Clay minerals in nature and their characterization, modification and application. Intech 56–80. http://dx.doi.org/10.5772/48123

Lee, W. E, Ojovan, M. I. 2013. Fundamentals of radioactive waste (RAW): science, sources, classification and management strategies. In: Lee, W. E., Ojovan, M. I., Jantzen, C. M. (Eds), Radioactive waste management and contaminated site clean-up, Woodhead Publishing.

Lee, Y.J., Morse, J.W., Wlitschko, D. V., 1996. An experimentally verified model for calcite precipitation in veins. Chemical Geology 130, 203–215. https://doi.org/10.1016/0009-2541(96)00008-3

Lei, Q., Latham, J., Tsang, C. 2017. The use of discrete fracture networks for modelling coupled geomechanical and hydrological behaviour of fractured rocks Computers and Geotechnics 85, 151–176 https://doi.org/10.1016/j.compgeo.2016.12.024

Lisle, R.J., 2013. Shear zone deformation determined from sigmoidal tension gashes. Journal of Structural Geology 50, 35–43. https://doi.org/10.1016/j.jsg.2012.08.002

Liu, E., 2005. Effects of fracture aperture and roughness on hydraulic and mechanical properties of rocks: implication of seismic characterization of fractured reservoirs. Journal of Geophysics and Engineering 2/1, 38–47. https://doi.org/10.1088/1742-2132/2/1/006

López Moro, F.J., 2012. EASYGRESGRANT—A Microsoft Excel spreadsheet to quantify volume changes and to perform mass-balance modelling in metasomatic systems. Computers & Geosciences 39, 191–196. https://doi.org/ 10.1016/j.cageo.2011.07.014

Lowell, R. P., Van Cappellen, P., Germanovich, L. N., 1993. Silica precipitation in fractures and the evolution of permeability in hydrothermal upflow zones. Science 260, 192–194. https://doi.org/10.1126/science.260.5105.192

M. Tóth, T., 2010. Determination of geometric parameters of fracture networks using 1D data. Journal of Structural Geology 32, 878–885. https://doi.org/10.1016/j.jsg.2009.04.006

M. Tóth, T., 2018. Fracture network characterisation using 1D and 2D data of the Mórágy Granite body, Southern Hungary. Journal of Structural Geology 113, 176–187. https://doi.org/10.1016/j.jsg.2018.05.029

M. Tóth, T., Hollós, Cs., Szűcs, É., Schubert, F., 2004. Conceptual fracture network model of the crystalline basement of the Szeghalom Dome (Pannonian Basin, SE Hungary). Acta Geologica Hungarica 47/1, 19–34. https://doi.org/10.1556/AGeol.47.2004.1.2

M. Tóth, T., Vass, I., 2011. Relationship between the geometric parameters of rock fractures, the size of percolation clusters and REV. Mathematical Geosciences 43, 75–97. https://doi.org/10.1007/s11004-010-9315-4

Maclean, W.H., Kranidiotis, P., 1987. Immobile Elements as Monitors of Mass-Transfer in Hydrothermal Alteration - Phelps Dodge Massive Sulfide Deposit, Matagami, Quebec. Economic Geology 82, 951–962. https://doi.org/10.2113/gsecongeo.82.4.951

Maros, Gy., Koroknai, B., Palotás, K., Fodor, L., Dudko, A., Forián-Szabó, M., Zilahi-Sebess, L., Bán-Győri, E., 2004. Tectonic analysis and structural evolution of the north-eastern Mórágy Block. Annual Report of the Geological Institute of Hungary 2003, 371–386.

Maros, Gy., Palotás, K., Fodor, L., Sallay, E., Rálischné Felgenhauer, E., Koroknai, B., Matayiko, M., 2000. A Bodai Aleurolit Formációban mélyült D–5 és D–6 fúrások ImaGeo magszkennerrel történt értékelésének eredményei. Kézirat, Magyar Állami Földtani Intézet, Budapest. (in Hungarian)

Martinez-Torres, L. P., 2002. Characterization of naturally fractured reservoirs from conventional well logs. Msc Thesis, University of Oklahoma

Massiot, C., Townend, J., Nicol, A., McNamara, D. D., 2017. Statistical methods of fracture characterization using acoustic borehole televiewer log interpretation: BHTV Fracture Data Analysis. Journal of Geophysical Research: Solid Earth 122:6836–6852. https://doi.org/10.1002/2017JB014115

Massiot, C., Townend, J., Nicol, A., McNamara, D. D., 2017. Statistical methods of fracture characterization using acoustic borehole televiewer log interpretation Journal of Geophysical Research: Solid Earth 122/8 6836–6852. https://doi.org/10.1002/2017JB014115

Máthé, Z., 2015. Results of mineralogical, petrological and geochemical investigation of Boda Claystone Formation. Doctoral dissertation Eötvös Lóránd University, Budapest, Hungary 130 p. (in Hungarian with English summary).

Means, W.D., Li, T., 2001. A laboratory simulation of fibrous veins: some first observations. Journal of Structural Geology 23, 857–863. https://doi.org/10.1016/S0191-8141(00)00158-9

Min, K. B., Jing, L., Stephansson, O., 2004. Determining the equivalent permeability tensor for fractured rock masses using a stochastic REV approach: Method and application to the field data from Sellafield, UK. Hydrogeology Journal 12/5, 497–510. https://doi.org/10.1007/s10040-004-0331-7

Mukherjee, P.K., Gupta, P.K., 2008. Arbitrary scaling in ISOCON method of geochemical mass balance: An evaluation of the graphical approach. Geochemical Journal 42, 247–253. https://doi.org/10.2343/GEOCHEMJ.42.247

National Research Council, 1996. Rock Fractures and Fluid Flow: Contemporary Understanding and Applications. Chapter: 2 Physical Characteristics of Fractures and

Fracture Patterns. Washington, DC: The National Academies Press. https://doi.org/10.17226/2309

NEA 2010. Self-sealing of Fractures in Argillaceous Formations in the Context of Geological Disposal of Radioactive Waste, OECD Publishing, Paris ISBN 978-92-64-99095-1

Nelson, R. A., 2001. Geologic analysis of naturally fractured reservoirs, 2nd ed. Gulf Professional Publication, Boston

Németh, T., Máthé, Z., Pekker, P., Dódony, I., Kovács-Kis, V., Sipos, P, Cora, I., Kovács, I., 2016. Clay mineralogy of the Boda Claystone Formation (Mecsek Mts., SW Hungary) Open Geosciences, 8/1, 259–274. http://dx.doi.org/10.1515/geo-2016-0024

Neuzil, C. E., Tracy, J. V., 1981. Flow through fractures. Water Resources Research 17/1, 191–199. https://doi.org/10.1029/WR017i001p00191

Nicholson, R., 1991. Vein morphology, host rock deformation and the origin of the fabrics of echelon mineral veins. Jorunal of Structural Geology 13, 635–641. https://doi.org/10.1016/0191-8141(91)90026-F

Nicholson, R., 2000. Inter-array and intra-array kinematics of en echelon sigmoidal veins in cross-bedded sandstone, Merimbula, southeastern Australia: Discussion. Journal of Structural Geology 22, 145–145. https://doi.org/10.1016/S0191-8141(99)00004-8

Nicholson, R., Ejiofor, I.B., 1987. The three-dimensional morphology of arrays of echelon and sigmoidal, mineral-filled fractures - Data from North Cornwall. Journal of the Geological Society 144, 79–83. https://doi.org/10.1144/gsjgs.144.1.0079

Nicholson, R., Pollard, D.D., 1985. Dilation and linkage of echelon cracks. Journal of Structural Geology 7, 583–590. https://doi.org/10.1016/0191-8141(85)90030-6

Norris, S., 2017. Radioactive waste confinement: clays in natural and engineered barriers – introduction. Ed(s): Norris S., Bruno J., Van Geet E.A.C., Verhoef E. Radioactive Waste Confinement: Clays in Natural and Engineered Barriers. Geological Society, London, Special Publications, 443, 1–8, https://doi.org/10.1144/SP443.26

Olive, D. J., 2017. Linear regression. Springer Cham, Switzerland. https://doi.org/10.1007/978-3-319-55252-1

Olson, J.E., Pollard, D.D., 1991. The initiation and growth of en-echelon veins. Journal of Structural Geology 13, 595–608. https://doi.org/10.1016/0191-8141(91)90046-L

Olsson, R., Barton, N., 2001. An improved model for hydromechanical coupling during shearing of rock joints: International Journal of Rock Mechanics and Mining Sciences 38/3, 317–329. https://doi.org/10.1016/S1365-1609(00)00079-4

Opheim, J. A., Gudmundsson, A., 1989. Formation and geometry of fractures, and related volcanism, of the Krafla fissure swarm, northeast Iceland. Bulletin of the Geological

Society of America 101, 1608–1622. https://doi.org/10.1130/0016-7606(1989)101<1608:FAGOFA>2.3.CO;2

Paillet, F. L., Kay, R. T., Yeskis, D., Pedler, W., 1993. Integrating well logs into a multi-scale investigation of a fractured sedimentary aquifer. The Log Analyst 34/1, 13–23.

Paterson, M. S., 1978. Experimental Rock Deformation: The Brittle Field. Berlin: Springer. https://doi.org/10.1007/b137431

Pavičić, I., Galić, I., Kucelj, M., Dragičević I., 2021. Fracture System and Rock-Mass Characterization by Borehole Camera Surveying: Application in Dimension Stone Investigations in Geologically Complex Structures. Applied Sciences 11, 764. https://doi.org/10.3390/ app11020764

Picard, M. D., 1971. Classification of Fine-grained Sedimentary Rocks. SEPM Journal of Sedimentary Research, 41/1, 179–195. doi:10.1306/74d7221b-2b21-11d7-8648000102c1865d

Pollard, D. D., Segall, P., 1987. Theoretical displacements and stresses near fractures in rock: with application to faults, joints, veins, dikes and solution surfaces. In: Atkinson, B. (Ed.), Fracture Mechanics of Rock. Academic Press, London. https://doi.org/10.1016/C2009-0-21691-6

Pöppelreiter, M., García-Carballido, C., Kraaijveld, M., 2010. Borehole Image Log Technology: Application Across the Exploration and Production Life Cycle. In: Dipmeter and Borehole Image Log Technology. American Association of Petroleum Geologists, 1–13

Ramsay, J.G., 1980. Shear Zone Geometry - a Review. Journal of Structural Geology 2, 83–99. https://doi.org/10.1016/0191-8141(80)90038-3

Ramsay, J.G., Graham, R.H., 1970. Strain variations in shear belts. Canadian Journal of Earth Sciences 7, 786–813. https://doi.org/10.1139/e70-078

Ramsay, J.G., Huber, M.I., 1983. The techniques of modern structural geology. Academic Press, London; New York.

Ramsay, J.G., Huber, M.I., 1987. The techniques of modern structural geology: 2: Folds and Fractures. Academic Press, London; New York.

Rickard, M.J., Rixon, L.K., 1983. Stress Configurations in Conjugate Quartz-Vein Arrays. Journal of Structural Geology 5, 573–578. https://doi.org/10.1016/0191-8141(83)90069-X

Rothery, E., 1988. En-Echelon Vein Array Development in Extension and Shear. Journal of Structural Geology 10, 63–71. https://doi.org/10.1016/0191-8141(88)90128-9

Rutqvist, J., Graupner, B., Guglielmi, Y., Kim, T., Maßmann, J., Nguyen, T. S., Jung-Wook Park, J. W., Shiu, W., Urpi, L., Yoon, J. S., Ziefle, G., Birkholzer, J., 2020. An international

model comparison study of controlled fault activation experiments in argillaceous claystone at the Mont Terri Laboratory. International Journal of Rock Mechanics & Mining Sciences 136, 104505. https://doi.org/10.1016/j.ijrmms.2020.104505

Rutter, E.H., 1983. Pressure Solution in Nature, Theory and Experiment. Journal of Geological Society London 140, 725–740. https://doi.org/10.1144/gsjgs.140.5.0725

Schneider, C.A., Rasband, W.S., Eliceiri, K.W., 2012. NIH Image to ImageJ: 25 years of image analysis. Nat. Methods 9, 671–675.

Sebe, K., 2017. Structural evolution of the Mecsek–Villány area (SW Hungary) during post-rift phase and basin inversion, in: Horvat, M., Wacha, L. (Eds.), 7th International Workshop "Neogene of Central and South-Eastern Europe". Velika, Croatia.

Seyum, S., Pollard, D.D., 2016. The mechanics of intersecting echelon veins and pressure solution seams in limestone. Journal of Structural Geology 89, 250–263. https://doi.org/10.1016/j.jsg.2016.06.009

Shalaby, M. R., Islam, M. A., 2017. Fracture detection using conventional well logging in carbonate Matulla Formation, Geisum oil field, southern Gulf of Suez, Egypt. Journal of Petroleum Exploration and Production Technology 7, 977–989. https://doi.org/10.1007/s13202-017-0343-1

Smith, J.V., 1995. True and Apparent Geometric Variability of En-Echelon Vein Arrays. Journal of Structural Geology 17, 1621–1626. https://doi.org/10.1016/0191-8141(95)00058-L

Sonnberger, M., Ruddat, M., Arnold, A., Scheer, D., Poortinga, W., Bo, G., Bertoldo, R., Mays, C., Pidgeon, N., Poumadère, M., Steentjesc, K., Tvinnereimi, E., 2021. Climate concerned but anti-nuclear: Exploring (dis)approval of nuclear energy in four European countries. Energy Research & Social Science, 75, 102008. https://doi.org/10.1016/j.erss.2021.102008

Swanson, M.T., 1992. Late Acadian-Alleghian transpressional deformation: evidence from asymmetric boudinage in the Casco Bay area, coastal Maine. Journal of Structural Geology 14, 323–341. https://doi.org/10.1016/0191-8141(92)90090-J

Taherdangkoo, R., Abdideh, M., 2016. Application of wavelet transform to detect fractured zones using conventional well logs data (case study: southwest of Iran). International Journal of Petroleum Engineering 2, 125. https://doi.org/10.1504/IJPE.2016.078818

Thiele, S.T., Micklethwaite, S., Bourke, P., Verrall, M., Kovesi, P., 2015. Insights into the mechanics of en-échelon sigmoidal vein formation using ultra-high resolution photogrammetry and computed tomography. Journal of Structural Geology 77, 27–44. https://doi.org/10.1016/j.jsg.2015.05.006

Tokan-Lawal, A., Prodanović, M., Landry, C., J., Eichubl, P., 2017. Influence of numerical cementation on multiphase displacement in rough fractures. Transport in Porous Media 116/1, 275–293. https://doi.org/10.1007/s11242-016-0773-0

Tokhmchi, B., Memarian, H., Rezaee, M. R., 2010. Estimation of the fracture density in fractured zones using petrophysical logs. Journal of Petroleum Science and Engineering 72, 206–213. https://doi.org/10.1016/j.petrol.2010.03.018

Tóth, E., Hrabovszki, E., M. Tóth, T., 2023. Using geophysical log data to predict the fracture density in a claystone host rock for storing high-level nuclear waste. Acta Geodaetica et Geophysica (In Press)

Tóth, E., Hrabovszki, E., M. Tóth, T., Schubert, F., 2020. Shear strain and volume change associated with sigmoidal vein arrays in the Boda Claystone, Journal of Structural Geology 138, 104105. https://doi.org/10.1016/j.jsg.2020.104105

Tóth, E., Hrabovszki, E., Schubert, F., M. Tóth, T., 2022a. Discrete fracture network (DFN) modelling of a high-level radioactive waste repository host rock and the effects on its hydrogeological behaviour. Journal of Structural Geology 156, 104556. https://doi.org/10.1016/j.jsg.2022.104556

Tóth, E., Hrabovszki, E., Schubert, F., M. Tóth, T., 2022b. Geometrical and hydrogeological properties of the fracture network of the Boda Claystone Formation based on the BAF–2, BAF–3, BAF–3A and BAF–4 wells. In: Hámos, G., Sámson, M. (Eds.) A Bodai Agyagkő Formáció (BAF) kutatásának legújabb eredményei. Magyarhoni Földtani Társulat, Pécs, 108–109.

Tóth, E., Hrabovszki, E., Schubert, F., M. Tóth, T., 2022c. Lithology-Controlled Hydrodynamic Behaviour of a Fractured Sandstone–Claystone Body in a Radioactive Waste Repository Site, SW Hungary. Applied Sciences 12, 2528. https://doi.org/10.3390/app12052528

Tóth, E., Hrabovszki, E., Steinbach, G., Schubert, F., 2018. Quantitative estimation of shear strain and volume change using sigmoidal tension gashes. Bulletin of the Hungarian Geological Society 148/4, 367–380. (in Hungarian with English abstract). https://doi.org/10.23928/foldt.kozl.2018.148.4.367

Tournassat, C., Vinsot, A., Gaucher, E. C., Altmann, S., 2015. Chemical Conditions in Clay-Rocks. Ed(s): Tournassat, C., Steefel, C. I., Bourg, I. C., Bergaya, F. Developments in Clay Science, 6, 71–100

Toussaint, R., Aharonov, E., Koehn, D., Gratier, J.P., Ebner, M., Baud, P., Rolland, A., Renard, F., 2018. Stylolites: A review. Journal of Structural Geology 114, 163–195. https://doi.org/10.1016/j.jsg.2018.05.003

Tranmer, M., Murphy, J., Elliot, M., Pampaka, M., 2020. Multiple Linear Regression (2nd Edition); Cathie Marsh Institute Working Paper 2020-01. https://hummedia.manchester.ac.uk/institutes/cmist/archive-publications/working-papers/2020/2020-1- multiple-linear-regression.pdf

Turcotte, D. L., 1992. Fractals and Chaos in Geology and Geophysics. Cambridge University Press. https://doi.org/10.1002/gj.3350280216

Varga, A., 2009. Petrology and Geochemistry of the Paleozoic–Lower Triassic Siliciclastic Rocks from Southern Transdanubia, Hungary. PhD thesis, Eötvös Loránd University, Budapest, Hungary 150 p. (in Hungarian with English summary).

Varga, A., Raucsik, B., Szakmány, Gy., Máthé, Z., 2006. Mineralogical, petrological and geochemical characteristics of the siliciclastic rock types of Boda Siltstone Formation. Bulletin of the Hungarian Geological Society 136/2, 201–231, (in Hungarian with English abstract).

Varga, A., Szakmány, Gy., Raucsik, B., Máthé, Z., 2005. Chemical composition, provenance and early diagenetic processes of playa lake deposits from the Boda Siltstone Formation (Upper Permian), SW Hungary. Acta Geologica Hungarica 48, 49–68. https://doi.org/10.1556/AGeol.48.2005.1.2

Vermilye, J. M., Scholz, C. H., 1995. Relation between vein length and aperture. Journal of Structural Geology 17/3, 423–434. https://doi.org/10.1016/0191-8141(94)00058-8

Vinod, H. D., 1973. Generalization of the durbin-watson statistic for higher order autoregressive processes, Communications in Statistics, 2/2, 115-144. https://doig.org/10.1080/03610927308827060

Wang, L. L., Bornert, M., Yang, D.S., Héripré, E., Chanchole, S., Halphen, B., Pouya, A., Caldemaison, D. 2015. Microstructural insight into the nonlinear swelling of argillaceous rocks. Engineering Geology, 193, 435–444 https://doi.org/10.1016/j.enggeo.2015.05.019

Wein Gy., 1967. Délkelet-Dunántúl hegységszerkezeti egységeinek összefüggései az óalpi ciklusban. Bulletin of the Hungarian Geological Society 97/3, 286–293. (in Hungarian)

Willemse, E.J.M., Pollard, D.D., 1998. On the orientation and patterns of wing cracks and solution surfaces at the tips of a sliding flaw or fault. Journal of Geophysical Research 103, 2417–2438. https://doi.org/10.1029/97JB01587

Wiltschko, D.V., Morse, J.W., 2001. Crystallization pressure versus "crack seal" as the mechanism for banded veins. Geology 29, 79–82. https://doi.org/10.1130/0091-7613(2001)029<0079:CPVCSA>2.0.CO;2

Witherspoon, P. A., Wang, J. S. Y., Iwai, K., Gale, J. E., 1980. Validity of cubic law for fluid flow in deformable rock fracture. Water Resources Research 16/6, 1016–1024. https://doi.org/10.1029/WR016i006p01016

Wu, Y. 2016. Multiphase Flow in Fractured Porous Media. (Ed.) Wu, Y. Multiphase Fluid Flow in Porous and Fractured Reservoirs. Gulf Professional Publishing, 207–250. doi:10.1016/b978-0-12-803848-2.00009-x

Yielding, G., Walsh, J. J., Watterson, J., 1992. The prediction of small scale faulting in reservoirs. First Break, 10, 449–460. https://doi.org/10.3997/1365-2397.1992023

Zazoun, R. S., 2013. Fracture density estimation from core and conventional well logs data using artificial neural networks: The Cambro-Ordovician reservoir of Mesdar oil field, Algeria. Journal of African Earth Sciences 83, 55–73. https://doi.org/10.1016/j.jafrearsci.2013.03.003

Zemanek, J., E. E. Glenn, L. J. Norton, R. L. Caldwell 1970. Formation evaluation by inspection with the borehole televiewer, Geophysics, 35/2 254–269. https://doi.org/10.1190/1.1440089

Zhang, C. L., 2013. Sealing of fractures in claystone. Journal of Rock Mechanics and Geotechnical Engineering 5/3, 214–220. https://doi.org/10.1016/j.jrmge.2013.04.001

Zimmerman, R. W., Bodvarsson, S., 1996. Hydraulic conductivity of rock fractures. Transport in Porous Media 23/1, 1–30. https://doi.org/10.1007/BF00145263

Zimmerman, R., Main, I., 2004. Hydromechanical Behavior of Fractured Rocks, Ed(s): Guéguen, Y., Boutéca, M. International Geophysics, Academic Press, 89, 363–421 https://doi.org/10.1016/S0074-6142(03)80023-2

SUMMARY

This dissertation extensively examines the brittle structural elements of the Boda Claystone Formation (BCF), which could serve as a host rock formation for high-level radioactive waste in Hungary (Konrád & Hámos, 2006). Despite the formation's low porosity and permeability, which give its retentive features, it is crucial to assess the tectonic setting of the rock body to comprehend the timing and magnitude of faults and folds. Since the possible fluid flow path ways are connected to fractures in an impermeable rock. This analysis enables an evaluation of the tectonic development of the host rock and the hydrogeological significance of the tectonic features (DELAY, 2010).

The idea behind the research is that each successive phase of the study examines the problem at an increasing scale, from microstructural observations to the model of the fracture network geometry in a borehole. Even the microscale investigations of individual fracture network segments contribute to the understanding of the behaviour of the whole fracture network. The main goals of this study were to identify the geometry and hydrodynamic properties of the fracture network of the Boda Claystone Formation the investigation of the spatial extensibility of the properties of the fracture network.

The BAF–2 well was regarded as a base well in this study because it explores the maximum thickness of the formation (917 m) with almost 100% core recovery and offers unique opportunity to evaluate its brittle structural elements. In addition, the analysis of the BAF–4 well was also done to investigate the extensibility of the properties of the fracture system.

In-depth analysis of the formation's brittle structures at different scales was performed in this study using a variety of methods. Petrology of the sigmoidal veins was analysed with standard polarization microscope. Volume and density change of the shear zones were analysed based on the geometry of the sigmoidal veins (Lisle, 2013), with micro-CT and with mass-balance analysis (Gresens, 1967; Grant, 1986). Discrete fracture network (DFN) modelling, which is based on the fractal-like characteristics of the fracture system in rocks, was used to model the geometry of the fracture network (Barton and Larsen, 1985). Hydrological properties of the fracture network were described with the flow zone indicator (FZI; Amaefule et al., 1993). This indicator, which denotes hydraulic flow units (HFU) within the system, is based on the porosity and permeability. Finally, multiple linear regression analysis was used to determine the relationship between the geophysical well log data and the fracture density in the Boda Claystone Formation based on two wells.

The study of the brittle structural elements of the Boda Claystone Formation has yielded important new results concerning the formation method of *en échelon* veins in claystone, the geometry and hydrological properties of the fracture network, and the controlling factors of fracture formation in the studied formation:

1. ***En échelon* veins of the BCF can be interpreted as pennant veins whose kinematics are controlled by Riedel conjugate fractures**. Sigmoidal shaped *en échelon* veins are peculiar structures of the BCF. The veins developed without the sign of pressure solution in shear zones in contrast to the general model. Their formation begins from initial flaws of the shear zone; triangular terminations arise at the tip of these localised shear planes. This triangular shape at the end of the veins is formed with rotation and slip of the shear fractures. Between these initial shear planes, rhombus-shaped vein segments could develop during the evolution of the shear zone with the rotation of these a sigmoidal-shaped vein could form. Mineral precipitation can also occur in the middle part of these shear planes if the orientation becomes favourable for vein opening induced by rotation by the shear zone. At the end of the process, a sigmoidal-shaped vein could form by connecting vein segments and continuous mineral precipitation.

2. **The shear zones of the BCF underwent volume loss despite vein formation and the precipitation of minerals.** Based on the isocon-method and the micro-CT measurements, 5–8% volume loss occurred in the shear zones. Despite the volume loss, the mass of the shear zone increased based on the isocon method. Assuming immobile Ti, the shear zone enriched in Ca, Mn, Ba, Sr and S relative to the host rock. The mineral composition of the veins explains the enrichment of these elements. Precipitation of minerals may have been responsible for the mass gain and could also cause volume gain. However, the shear zone carries volume loss. Consequently, the rate of volume loss must have been higher than the overall volume gain generated by mineral precipitation. The volume loss occurred in the rock bridges between the veins, where the 2D porosity is significantly less than in the wall rock outside the shear zone. Micro-CT measurements showed that the density of the rock bridges was also higher than the wall rock. I propose that the volume loss is the result of the partial porosity reduction of the shear zones that is caused by tectonic compaction.

3. **A large-scale fault can be interpreted in the BAF–2 well at 400 m based on fracture density, geophysical well log data and sedimentological observations.** The rock body of the BCF in the BAF–2 well can be divided into two major sections based on the properties of the fracture network. The characteristics of the fracture density differ

significantly in the upper half (0–400 m) and the lower half (400–915 m) of the well. The upper section is intensively and uniformly fractured, while the lower half contains significantly fewer fractures. In the lower half three distinct fractured zones could be traced where the fracture density increases. The lithology of the well is relatively homogeneous, although coarser-grained layers appear more frequently with depth. While changing grain size may impact the fracture density, tectonic processes predominantly determine where the highly fractured zones are located. At 400 m, the geophysical parameters of the formation change significantly, and there are stratigraphic irregularities, such as overturned beds and changes in graded sequences, indicating a large-scale structural element.

4. **Seven hydraulic flow unit and two poro-perm trends can describe the hydraulic behaviour of the rock body in the BAF–2 well**. The most part of the rock body conforms to one trend; the homogenous lithology of the well comes with uniform hydrodynamic characteristics. Only three narrow sections (at 100, 400, and 700 m) differ from this primary poro-perm trend. These sections define individual hydraulic units based on their flow zone indicator (FZI) value. The first zone occurs between 60 and 110 m. In this section, porosity decreases considerably more than permeability. The hydraulic properties of this section were altered by weathering as a result of the long-term near-surface exposure of the formation. The second zone is located between 350 and 420 m; the fault zone forms an independent hydraulic unit with elevated FZI. The third zone, where the FZI values are higher than the average, is between 690 and 770 m. In this zone, the lithology changes, and fine-sandstone layers are more common, which could influence the hydraulic behaviour of the rock body. On the other hand, the sonic log disruption in this HFU resembles the behaviour seen at about 400 m; therefore, the effects of a large-scale structure at this depth cannot be ruled out either.

5. **Five possible fracture network geometries could be distinguished based on the modelling in the BAF–2 well.** In some cases, the fracture network forms one communicating group along the well. In many cases, two connected subsystems appear that do not communicate with each another. In other modelling runs, the subgroup boundaries can be found at 300, 400 or 700 meters. Most models suggest that the fracture system of the well is separated at 100, 400, and 700 m into four fracture subgroups. The same horizons are designated by the interconnecting fracture clusters and the hydraulic flow units in the well.

6. **Fracture density can be predicted in the BCF based on the density and resistivity logs.** Based on multiple linear regression density and resistivity are the primary

determinants of the fracture density in BAF–4 and BAF–2 wells. In the upper part of the BAF–4 well, which was the training section of the regression analysis, a strong relationship was identified with a good fit, $R^2 = 0.767$. The correlation equation was validated in the lower part of the BAF–4 well ($R^2 = 0.630$). I predicted the fracture density of the BAF–2 well using the same method ($R^2 = 0.701$). The fracture density could be predicted with high accuracy in sections with the typical lithology of the BCF. The prediction is less precise in other situations where the lithological characteristics of the claystone are untypical. Fine sandstone layers are present in the lower part of the formation and this grain size variation affects the geophysical characteristics of the rock body. The regression function underestimates the fracture density of the rock body in these sandy areas. Fracture density of the BCF can be predicted with relatively high accuracy with the established regression equation in wells without BHTV from conventional geophysical well log data.

ÖSSZEFOGLALÁS

Jelen értekezés részletesen vizsgálja a Bodai Agyagkő Formáció (BAF) töréses szerkezeti elemeit, amely a magyarországi nagy aktivitású radioaktív hulladékok befogadó képződményeként szolgálhat (Konrád & Hámos, 2006). Annak ellenére, hogy a képződmény alacsony porozitása és permeabilitása kedvező tulajdonságokat biztosít a hulladéktároló kialakításához, kulcsfontosságú a kőzettest szerkezeti elemeinek felmérése, többek között a törések és a gyűrődések vizsgálata (Delay, 2010).

Kutatásom során az egymást követő munkafázisok során egyre nagyobb léptékben vizsgáltam a problémát, a mikroszerkezeti megfigyelésektől kezdve a töréshálózat több fúráson alapuló vizsgálatáig. Az egyes érgenerációk mikroszerkezeti vizsgálatával jobban megérthető a teljes töréshálózat viselkedése. A tanulmány fő célja a Bodai Agyagkő Formáció töréshálózat geometriájának és hidrodinamikai tulajdonságainak, valamint a repedésrendszer hidrodinamikai viselkedését befolyásoló főbb szerkezeti elemek helyzetének meghatározása.

A vizsgálat fókuszpontjában a BAF–2 kutatófúrás áll, amely a legnagyobb vastagságban harántolja a képződményt (917 m) valamint teljes hosszában magfúrással mélyült. Ennél fogva ez a fúrás kínálja a legjobb lehetőséget a képződmény töréses szerkezeti elemeinek vizsgálatára. A BAF–2 fúrás mellett a BAF–4 fúrás elemzése is megtörtént, amellyel a repedésrendszer tulajdonságainak kiterjeszthetőségét vizsgáltam.

Dolgozatomban igen széles vizsgálati mérettartományban, különféle módszerekkel részletesen elemeztem a képződmény töréses szerkezeti elemeit. A szigmoidális kulisszás erek petrográfiai leírása 30 μm vastagságú vékonycsiszolatokon történt, Olympus BX41 polarizációs mikroszkóp segítségével, a fotók Olympus DP73 típusú digitális kamerával készültek.

A nyírási zónák térfogat-, sűrűség-, és alakváltozását három különböző megközelítés alapján vizsgáltam. Az első módszer a szigmoidális erek geometriáján alapul. Lisle (2013) szerint az erek szigmoidális alakja kétféleképpen alakulhat ki; ezek a passzív forgási modell és a „redőzött kőzethíd” modell. A két modell alapján különböző módon kiszámítható a nyírási alakváltozás és térfogatváltozás, amennyiben ismerjük az erek és a nyírási zóna geometriai tulajdonságait, mint pl. a nyírási zóna vastagsága, a nyírási zóna határa és az ér csúcsa által bezárt szög, stb.

A második módszer a nyírási zónák teljes kémiai összetételén alapuló elemmobilizációs számításokat foglalja magába. A metaszomatikus folyamatok során végbemenő összetétel- és térfogatváltozás kapcsolatát leíró egyenletet Gresens (1967) írta le. Az egyenlet segítségével meghatározható a térfogat- és sűrűség-, valamint az egyes elemek mennyiségének változása a

kiindulási és az átalakult kőzet között Az izokon-módszer (Grant, 1986) Gresens (1967) egyenletének grafikus megoldása. Az izokon módszerben egy komponens koncentrációja az eredeti és az átalakult kőzetekben lineáris összefüggést mutat, az immobilis elemeknek az origón áthaladó izokon mentén kell elhelyezkedniük. Az izokonvonal felett elhelyezkedő elemek aránya nő, míg az izokonvonal alá eső elemek aránya csökken az átalakult kőzetben.

A harmadik megközelítés során a nyírási zóna és a mellékkőzet sűrűségváltozását Bruker Skyscan 2211 mikro-komputertomográfia (mikro-CT) segítségével vizsgáltam. A mérés elvégzéséhez a BAF reprezentatív elemi térfogatát (REV) képanalízissel határoztam meg ImageJ szoftver (verziószám 1.51) segítségével.

A töréshálózat geometriáját diszkrét törésekből felépülő (DFN) töréshálózat modellezési megközelítéssel modelleztem, amely a kőzetekben található törésrendszerek fraktálszerű tulajdonságain alapul (Barton és Larsen, 1985). A törésrendszer geometriájának és az egyes repedések apertúrájának megértése a DFN modellek alapja (Barcelona et al. 2020). Ez a modellezési megközelítés lehetővé teszi a törésrendszer konnektivitásának, porozitásának és permeabilitásának becslését. A tanulmányban az Infress töréshálózat-modellező program segítségével modelleztem a töréshálózat geometriáját. A töréshossz, a töréssűrűség, a törés orientációja és az apertúra a DFN-modellek létrehozásához szükséges változók. A töréssűrűséget a P10 paraméterrel és fraktáldimenzióval jellemeztem, a P10 paraméter megmutatja, hány törés fordul elő méterenként. A törések hosszúságának meghatározásához szükséges két különböző felbontóképességű módszer által meghatározott törés szám (M. Tóth, 2010). A töréshossz-eloszlás paraméterei törések számának különbségéből és az alkalmazott módszerek felbontási határai alapján számíthatók ki. A kevésbé érzékeny megközelítéssel észlelt törések száma elkerülhetetlenül kevesebb, mint az érzékenyebb módszerrel észlelt törések száma (M. Tóth, 2010). Munkámban a töréshossz-eloszlás paramétereit akusztikus lyukfal televízió (BHTV) adatok és magládafotók felhasználásával számítottam ki. A törések orientációját a dőlésirány és a dőlésszög írja le, amelyeket a BHTV adatok alapján határoztam meg. Az apertúra koefficiens kiszámításához a többpakkeres kút teszten és a DFN modellen alapuló apertúra kalibrációt használtam. Az apertúra kalibráció során a fúrásban mért és a modellezett permeabilitás adatokat hasonlítottam össze, majd a modellben úgy változtattam a törések nyitottságát, hogy a mért és modellezett permeabilitás egyenlővé váljon. Így a repedésrendszer effektív apertúrája meghatározható, ami lehetővé teszi az effektív porozitás kiszámítását.

A töréshálózat hidrológiai tulajdonságait az áramlási zóna indikátorral jellemeztem (FZI – *flow zone indicator*; Amaefule et al., 1993). Ez a mutató a porozitás és a permeabilitás alapján

hidraulikus áramlási egységeket jelöl ki, amelyeken belül az áramlást irányító tényezők egységesnek tekinthetők.

Végül többszörös lineáris regressziós analízis alkalmazásával vizsgáltam a lyukgeofizikai szelvények és a töréssűrűség kapcsolatát a BAF-ot harántoló két fúrásban. A többszörös lineáris regresszió egy statisztikai módszer, amellyel meghatározható, hogy egy függő változó milyen szorosan kapcsolódik független változók egy csoportjához. Munkámban a töréssűrűség a becsült függő változó. A független változók azok, amelyek hatással vannak a töréssűrűségre, jelen tanulmányban a lyukgeofizikai adatok. Munkám során a lyukgeofizikai adatok és a képződmény töréssűrűsége közötti kapcsolat értékelésére az IBM SPSS statisztikai programot használtam. A felállított regressziós egyenlet segítségével a töréssűrűség megbecsülhető a hagyományos lyukgeofizikai szelvények alapján.

A Bodai Agyagkő Formáció töréses szerkezeti elemeinek vizsgálata fontos új eredményeket hozott az agyagkőben keletkező szigmoidális alakú kulisszás erek képződési mechanizmusaival, BAF a töréshálózat geometriájával és hidrológiai tulajdonságaival, valamint a vizsgált képződmény repedésképződését szabályozó tényezőkkel kapcsolatban:

1. **A BAF-ban megjelenő *en échelon* erek „pennant" erekként értelmezhetők, amelyek kialakulását Riedel konjugált törések okozták.** Az erek nyírási zónákban, számottevő nyomási oldódás nélkül alakultak ki az általános modellel ellentétben. A kulisszás erek a nyírási zónákban, kezdeti gyengeségi síkok mentén alakultak ki, ezeknek a lokalizált nyírási síkoknak a csúcsán háromszög alakú végződések keletkeztek. A háromszög alak az erek végén a nyírásos törések forgásával és csúszásával jött létre. Ezen kezdeti nyírási síkok között a nyírási zóna kialakulása során rombusz alakú érszakaszok alakulhattak ki, amelyek rotációjával szigmoid alakú ér képződhet. Amennyiben a törés orientációja kedvezővé válik, felnyílás és érképződés is történhet. A folyamat végén érszegmensek összekapcsolásával és folyamatos ásványkiválással szigmoidális alakú ér alakulhat ki.

2. **A BAF nyírási zónái az érképződés és az ásványok kiválása ellenére térfogatcsökkenésen mentek keresztül.** Az izokon-módszer és a mikro-CT mérések alapján a nyírási zónákban 5-8%-os térfogatveszteség jött létre. A térfogatcsökkenés ellenére a nyírási zóna tömege az izokon módszer alapján nőtt. A Ti-t immobilis elemnek feltételezve a nyírási zóna Ca, Mn, Ba, Sr és S tartalma növekedett a befogadó kőzethez képest. Az erek ásványos kalcitból, anhidritből, barit-célesztinből állnak, amelyek kémiai összetétele magyarázza feldúsulásuló elemeket. Az ásványok kiválása tömegnövekedést és térfogatnövekedést okoz a nyírási zónában, azonban a nyírási zóna térfogata összességében

csökkent. Következésképpen a térfogatcsökkenés mértékének nagyobbnak kellett lennie, mint az ásványok kicsapódása által generált teljes térfogatnövekedésnek. A térfogatveszteség az erek közötti kőzethidakban mehetett végbe, ahol a 2D porozitás lényegesen kisebb, mint a nyírási zónán kívüli mellékkőzetben. A mikro-CT mérések kimutatták, hogy a kőzethidak sűrűsége is megnövekedett a mellékkőzethez képest. Ezek alapján a nyírási zónák térfogatcsökkenése tektonikus kompakció és porozitáscsökkenés révén alakulhatott ki.

3. Nagyléptékű szerkezeti határ található a BAF–2 fúrásban 400 m mélységben. A BAF–2 fúrás kőzetoszlopa két, egymástól jelentősen eltérő szakaszra osztható fel a töréshálózat tulajdonságai alapján**.** A töréssűrűség jelentősen eltér egymástól a fúrás felső (0-400 m) és alsó (400-915) szakaszában. A felső rész erőteljesen és egységesen töredezett, míg a fúrás alsó szakasza jelentősen kevesebb törést tartalmaz. A fúrás alsó felében három, jól elkülöníthető törési zóna helyezkedik el, amelyekben a töréssűrűség megemelkedik. A kőzetoszlop litológiája homogén, azonban a mélységgel az átlagos szemcseméret növekszik, finomszemcsés homokkő betelepülések egyre gyakoribbá válnak a fekü felé. A változó szemcseméret befolyásolhatja a töréssűrűséget, azonban a törési zónák elhelyezkedését elsősorban a tektonikai folyamatok határozzák meg. 400 m mélységben a kőzettest geofizikai tulajdonságai megváltoznak, átfordult rétegek és megváltozott gradációval rendelkező rétegek jellemzőek, valamint a jelentősen megváltozik a töréssűrűség amelyek alapján ebben a mélységben egy nagyléptékű vető helyezkedik el a képződményben.

4. A BAF–2 fúrás által feltárt kőzettest hét hidraulikai áramlási egységre osztható, amelyek két különböző poro-perm trenddel írhatók le. A kőzettest legnagyobb részének viselkedése jellemezhető egy poro-perm trenddel; a homogén litológia homogén hidrogeológiai tulajdonsággokkal jár. Az átlagos poro-perm trenddel csupán három keskeny szakasz (100, 400 és 700 m) hidrológiai viselkedése nem írható le. Ezek a zónák egyedi hidraulikai áramlási egységet alkotnak az áramlási zóna indikátor alapján. Az első zóna 60 és 110 m között helyezkedik el, itt a porozitás nagyobb mértékben csökken, mint a permeabilitás. Ebben a zónában, a hosszantartó felszín közeli elhelyezkedés következményeként, mállás határozta meg és módosította a kőzet hidrogeológiai tulajdonságait. A második zóna 350 és 420 m között húzódik; a nagyléptékű nyírási zóna független áramlási egységet alkot, amelyet a megemelkedett FZI értékek jeleznek. A harmadik megemelkedett FZI értékekkel rendelkező zóna 690 és 770 m között helyezkedik el. Ebben a mélységben egyre gyakoribbá válnak a képződményben

finomszemű homokkő betelepülések, amelyek befolyásolhatják a hidrogeológiai tulajdonságokat. A lyukgeofizikai szelvények alapján egy nagyléptékű szerkezeti elem jelenléte sem zárható ki ebben a mélységben, mivel a szelvények mintázata hasonlóságot mutat a 400 m-es mélységhez, ahol a nagyléptékű szerkezeti határ helyezkedik el a BAF–2 fúrásban. Mind ezek alapján a litológiai változékonyság mellett, tektonikai folyamatok is befolyásolhatták az áramlási egység kialakulását 690 és 770 m között.

5. Töréshálózati modellezés alapján öt lehetséges töréshálózati geometria különböztethető meg a BAF–2 fúrásban. A modellezett töréshálózatok azonos valószínűséggel fordulhatnak elő. Némely modellben a töréshálózat egy kommunikáló rendszert alkot a fúrás teljes hosszában. Számos esetben azonban két egymással nem kommunikáló alrendszer alakul ki. Egyes futások alapján a határok 300, 400 vagy 700 m-en találhatók meg. Néhány esetben a töréshálózat négy kommunikáló alcsoportra esett szét, ezek határai 100, 400 és 700 m helyezkednek el. Az egymással kommunikáló töréscsoportok határai és az áramlási egységek ugyanazon horizontokat jelölik ki a kőzettestben.

6. A BAF-ban a töréssűrűség megbecsülhető a sűrűség és ellenállás szelvények alapján. A többszörös regressziós analízis alapján a töréssűrűséget lyukgeofizikai mérések közül a sűrűség és ellenállás értékek befolyásolják a BAF–2 és BAF–4 fúrásokban. A BAF–4 fúrás felső szakaszában, amely a regressziós analízis tanító szakasza volt, erős kapcsolat áll fenn a töréssűrűség és a lyukgeofizikai értékek között, kiváló illeszkedéssel $R^2 = 0{,}767$. A korrelációs együttható validálása a BAF–4 fúrás alsó szakaszán ($R^2 = 0{,}630$) valamint a BAF–2 fúrásban is ($R^2 = 0{,}701$) jó illeszkedést mutat. A regressziós egyenlettel nagy pontossággal megbecsülhető a töréssűrűség a BAF-ra jellemző tipikus litológiával rendelkező kőzetszakaszokban. Az becslés pontossága csökken, ahol az agyagkő litológiai jellemzői eltérnek a tipikustól. A formáció alsó részén finom homokkőrétegek vannak jelen, ez a szemcseméret-változás befolyásolja a kőzettest geofizikai jellemzőit, amely miatt a regressziós függvény alábecsüli a kőzettest repedéssűrűségét a homokos szakaszokban. A jövőben a regressziós egyenlettel, BHTV mérések nélküli, csak hagyományos lyukgeofizikai szelvényekkel rendelkező fúrásokban is megbecsülhető a töréssűrűség.

DECLARATION OF THE SUPERVISOR

I hereby confirm that the content of the dissertation is based on the independent work of the doctoral candidate and that she has contributed decisively to the results through her independent creative activity. I consider the entire dissertation to be eligible for support from a professional and academic point of view and recommend its acceptance.

Szeged, 20.02.2023.

Tivadar M. Tóth DSc
supervisor

DECLARATION OF THE SUPERVISOR

I hereby confirm that the content of the dissertation is based on the independent work of the doctoral candidate and that she has contributed decisively to the results through her independent creative activity. I consider the entire dissertation to be eligible for support from a professional and academic point of view and recommend its acceptance.

Szeged, 20.02.2023.

Félix Schubert PhD
supervisor